THE EFFECT OF VARYING SECONDARY MACH NUMBER AND INJECTION ANGLE ON SECONDARY GASEOUS INJECTION INTO A SUPERSONIC FLOW

by

Larry Neil Koch

United States
Naval Postgraduate School

THESIS

THE EFFECT OF VARYING SECONDARY MACH NUMBER AND INJECTION ANGLE ON SECONDARY GASEOUS INJECTION INTO A SUPERSONIC FLOW

by

Larry Neil Koch

June 1969

The Effect of Varying Secondary Mach Number and Injection Angle on Secondary Gaseous Injection into a Supersonic Flow

by

Larry Neil Koch
Lieutenant, United States Navy
B.S., United States Naval Academy, 1961

Submitted in partial fulfillment of the
requirements for the degree of

AERONAUTICAL ENGINEER

from the

NAVAL POSTGRADUATE SCHOOL
June 1969

ABSTRACT

This study was undertaken to investigate the effects of varying both the secondary Mach number and angle of inclination relative to the primary stream on the flow field generated by the interaction of a secondary jet with a supersonic mainstream. The experimental portions of this investigation were conducted at a primary Mach number of 2.80 in the Naval Postgraduate School Supersonic Wind Tunnel. Data are presented and compared with various theories. This presentation includes correlation of the penetration height of the secondary flow, bow-shock shape by non-dimensionalization with respect to various parameters and correlation of interaction side force amplification factor.

TABLE OF CONTENTS

LIST OF FIGURES

LIST OF SYMBOLS

Symbol	Definition
A	experimental side force amplification factor
A_t	nozzle throat area
A^*	sonic area projected on a plane normal to the wall or flat plate
a	speed of sound
a_t	speed of sound at the nozzle throat (generally equal to a*)
a_∞	speed of sound at infinity in the primary stream
a^*	speed of sound at sonic conditions
b	$-J_o\lambda_1$
c	nozzle discharge coefficient
C_p^*	Newtonian pressure coefficient behind a normal shock
C_D	drag coefficient
d_t	nozzle throat diameter
E	energy per unit length of a line charge
E'	analogous energy term for secondary injection
F_i	interaction side force
F_j	secondary nozzle thrust
F_{jo}	secondary nozzle thrust in a vacuum
F_w	force on wall or flat plate
F_x	force component in streamwise direction
h	penetration height of secondary injectant
J_o	first order blast wave constant

k_1	constant from evaluation of the blast wave theory pressure distribution function integral
k_2	constant from evaluation of the blast wave theory pressure distribution function integral
M_∞	primary Mach number
M_s	secondary injection Mach number
m_p	molecular weight of primary gases
$\dot{m}$	mass flow rate
$\dot{m}_s$	secondary mass flow rate
P_D	static pressure immediately behind Mach disc
P_{pt}	primary stream total pressure
P_{st}	secondary stream total pressure
P_1	pressure on the surface of a flat plate without injection
P_∞	free stream pressure at infinity
q_1	dynamic pressure on a flat plate without injection
R_o	blast wave characteristic radius
R	bow shock radius at x
$\bar{R}$	R/R_o
R'	R/h
s	length of plate
T_{pt}	primary total temperature
T_{st}	secondary total temperature
V_e	velocity at the exit plane of a nozzle
V_j	secondary velocity
V_{jx}	component of the secondary velocity parallel to the primary stream
V_p	velocity of the primary flow
V_s	blast wave shock speed

x	distance along the flat plate measured from injector centerline (positive in the downstream direction)
$\bar{x}$	x/R_o
x'	x/h
z	non-dimensional pressure coefficient
α	primary nozzle divergence half angle
δ	boundary layer separation angle
ε	injection inclination angle measured between the flat plate surface and the free stream such that for epsilon less than 90° an upstream component of secondary flow exists
θ	the conical shock angle associated with a cone of half-angle δ
λ_k	higher order blast wave coefficients ($k = 1,2, \ldots$)
ρ	density
ρ^*	density at sonic conditions
ρ_t	density at the nozzle throat (generally equal to ρ^*)
ϕ	$b\bar{R}$

ACKNOWLEDGMENT

The author would like to express his indebtedness to Professor Daniel J. Collins for his interest and guidance in all phases of this study and to Mr. Norman Leckenby, Mechanical and Aerospace Engineering Technician, for his enthusiastic and competent technical assistance in the experimental portions of the investigation.

I. INTRODUCTION

For a period of time spanning at least the last decade, considerable interest has been displayed in the interaction of secondary gaseous flows injected into a primary supersonic stream. Several theoretical models exist which reflect the physical trends expected for varying sets of injection parameters (such as injection pressure, temperature, mass flow rate, Mach number and angle of inclination to the primary flow, et cetera). The body of experimental investigation has, for the most part, concerned itself with sonic injection normal to the primary stream.

The objective of this work is to study the phenomena associated with changes of both injection Mach number and inclination angle in order to compare results with the analytical models presently available. The degree to which correlation of experimental and theoretical results are obtained and the empirical relationships observed will be discussed.

This study was performed at the Naval Postgraduate School Supersonic Blow-Down Wind Tunnel operating at a primary Mach number of 2.80. A flat plate model incorporating an interchangeable nozzle set and instrumented for the collection of plate surface pressure distribution was constructed and used in this investigation. Commercially available dry nitrogen, helium and argon were

injected into the main air flow at various stagnation pressures and mass flow rates through nozzles of varying Mach number and angle of inclination to the primary stream.

II. EXPERIMENTAL APPARATUS

A. THE FLAT PLATE MODEL

The pylon mounted flat plate model shown in Figure 1 (made of steel and flash plated with chromium) was mounted in the test section of the Naval Postgraduate School Supersonic Wind Tunnel. The tubing which leads to the forty-seven pressure taps arranged on the upper surface of the flat plate passes through the model pylon and the tunnel floor. The pressure tap locations are depicted in Figure 2. Access for mating the nozzles with the injectant gas supply lines is also made available through the model pylon and tunnel floor. A representative set of drawings of three interchangeable injection nozzles is provided in Figure 3 showing, from left to right, a normal sonic nozzle, a normal supersonic nozzle and an inclined supersonic nozzle. All nozzles have a throat diameter of 0.1000 ± 0.001 and convergence and divergence half-angles of 10°. Nozzles were constructed for injection at Mach numbers of 1.00, 1.73 and 2.13. For each Mach number nozzles were constructed at nominal inclination angles ε of 90°, 80°, 70°, 60° and 50°. Epsilon is taken to be the angle between the nozzle axis and the direction of the primary stream (or the surface of the flat plate) in a sense such that for injection not normal to the primary flow an upstream component of the secondary flow exists. The nozzles are inserted from above the model. Alignment

and a positive in-place lock for securing the nozzles in position is provided by a small key bolt passing through the pylon from below

B. THE WIND TUNNEL

This investigation was conducted in the Naval Post-graduate School Blow-Down Wind Tunnel. The facility has a test section 4 inches by 4 inches in cross-section by 6 inches in length and provides an approximate run time of 5 minutes at a Mach number of 2.80 and a stagnation pressure of 50 psia. The lower (tunnel floor) aluminum block was replaced by an accurate phenolic replica of the original lower block in order to facilitate mounting the model with its required tunnel floor holes while preserving the geometry of the original block intact.

C. THE EXPERIMENTAL SET-UP

Figure 4 is a schematic representation of the equipment arrangement. The calibrating apparatus is not shown.

Injectant gas, manifolded from banks of four commercial high pressure cylinders, was supplied through a throttle valve into a sharp-edged orifice flowmeter. The flowmeter upstream pressure was measured in psia by a Heise gauge (Serial No. H 2946). Differential pressure across the orifice was sensed by a Statham differential pressure transducer (Serial No. 11404) calibrated in inches of mercury and capable of measuring a ± 10 psi differential at a working pressure of 500 psig maximum. The stagnation

temperature of the flow was measured at the flowmeter by means of a chromel-alumel thermocouple. The injectant gas then proceeded to an expansion chamber mounted adjacent to the lower wall of the wind tunnel in which the flow was effectively stagnated. At this station the total pressure of the secondary flow was measured by a Heise pressure gauge. The total temperature of the injectant measured at the expansion chamber agreed closely with that measured downstream of the flowmeter (within 5° F). The stagnation temperature at the flowmeter was taken to be the injection total temperature. The total temperature and total pressure of the primary flow was measured in the wind tunnel plenum chamber.

For side force determination, the static pressures were measured at the pressure taps on the flat plate model by a Scanivalve (Model 48J4 - 1065 Scanivalve with a 0-10 psia transducer) calibrated in inches of mercury vacuum. The measurements were recorded on a Honeywell 2106 twelve channel Visicorder as was the pressure differential across the flowmeter orifice mentioned above.

Schlieren photographs on Polaroid 4 x 5 type 55 P/N positive-negative film were taken of each run using an off-set Schlieren system with collimating mirrors.

Photographs of the experimental equipment are provided in Figures 5 through 9.

III. THEORETICAL ANALYSIS

From the many phenomena associated with secondary injection, it was chosen in this paper to deal with the characteristic radius which may be computed from the blast wave analogy model, the penetration height of the injected gas, the shape of the interaction or bow shock and the resultant normal side force developed on a flat plate.

A. PENETRATION HEIGHT

1. The Blunt Body Model of Zukoski and Spaid

The similarity of the shock shapes produced by secondary injection into supersonic main flows and the shock patterns produced by blunt axisymmetric bodies in supersonic flow prompted Zukoski and Spaid [Ref. 1] to develop a blunt body analogy to the secondary injection phenomena. Assuming the proper choice of a blunt body, the characteristic dimension of the nose (a length analogous to the penetration height of the secondary injectant) may be computed by equating the drag of the required blunt body to the change in momentum flux of the secondary injectant. These investigators assumed:

a. Sonic injection into a uniform supersonic flow with no boundary layer

b. No mixing between primary and secondary flows

c. The blunt body to be a quarter sphere with a semi-cylindrical afterbody

d. The injectant gases remain within the confines described in item C

By assuming Newtonian flow about a body in the form of a quarter-sphere with a half-cylinder afterbody, Zukoski and Spaid obtained the force balance

$$F_{x(\text{Injection})} = F_{x(\text{Blunt Body})} \tag{1}$$

or

$$\dot{m}_s V_{jx}^2 = (\pi/8)\, M_\infty^2\, \gamma_p C_p^* h^2\, P_\infty \tag{2}$$

V_{jx} is the streamwise velocity of the injectant and is determined by assuming isentropic expansion of the injectant from the secondary stagnation pressure to free-stream pressure. C_p^* is the Newtonian pressure coefficient behind a normal shock and is evaluated at the nose of the analogous blunt body.

Solving Equation (1) for the radius of the blunt body (the effective penetration height h) and applying a nozzle coefficient of discharge correction to permit the use of physical nozzle dimensions in these calculations, the following expression was obtained:

$$h/d\sqrt{c} = \frac{1}{M_\infty} \left(\frac{2P_{st}\gamma_s}{C_p^* P_{pt}\gamma_p}\right)^{1/2} \left\{\left(\frac{2}{\gamma_s-1}\right)\left(\frac{2}{\gamma_s+1}\right)^{(\gamma_s+1)/(\gamma_s-1)} \cdot \left[1-\left(\frac{P_{pt}}{P_{st}}\right)^{(\gamma_s-1)/(\gamma_s+1)}\right]\right\}^{1/4} \tag{3}$$

2. The Blunt Body Model of Cassel, Davis and Engh

In a manner somewhat similar to the method of Zukoski and Spaid, work by Cassel, Davis and Engh [Ref. 2] employed an equivalent blunt body analogy in the development of an expression of effective penetration height of a secondary injectant. The obstacle envisioned in their model is a cylinder which is tangent to a flat plate, capped on the upstream end by a half-sphere and oriented in the streamwise direction of the primary flow. Assuming that the momentum of the secondary gases is parallel to the plate at the sonic line in the plume of the secondary jet, these investigators also equate the change in the streamwise momentum of the injectant with the drag of the equivalent body. The following equation results:

$$C_D A^* q_1 - (P^* - P_1) A^* = \dot{m}_s [a^* + V_e \sin\varepsilon (90° - \varepsilon)] \qquad (4)$$

where A* is the projection of the sonic area on a plane normal to the wall, P* is the pressure at sonic conditions, A_t is secondary throat area, a* the speed of sound at sonic conditons and V_e is the secondary nozzle exit velocity. Continuity implies

$$\dot{m} = \rho^* A^* a^* = \rho_t A_t a_t = \gamma_s \left(\frac{2}{\gamma_s + 1}\right)^{\gamma_s/(\gamma_s - 1)} \frac{P_{st} A_t}{a_t}$$

for a perfect secondary gas at constant total temperature. Therefore, assuming that the frontal area of the injectant stream is effectively circular,

$$\frac{P_t^*}{P_{st}} = \frac{\rho^*}{\rho_t} = \frac{A_t}{A^*} = \left(\frac{d_t}{h}\right)^2 \tag{5}$$

Substituting into Equation (5) the two previous equations yields

$$\frac{A^*}{A_t} = \left(\frac{h}{d_t}\right)^2 = \left(\frac{2}{\gamma_s+1}\right)^{\gamma_s/(\gamma_s-1)} \left(\frac{P_{st}}{C_D q_1 + P_1}\right) \{\gamma_s [1+\frac{V_e}{a_t}\sin(90°-\varepsilon)]+1\}$$

In Ref. 3, the vacuum thrust coefficient of a nozzle is defined as

$$C_{f_o} = (\gamma_s+1)\left(\frac{2}{\gamma_s+1}\right)^{\gamma_s/(\gamma_s-1)} \tag{6}$$

combining the above equations, Cassel, Davis and Engh obtain

$$A^* = \frac{F_{jo}}{q_1}\left(\frac{1}{C_D+(2/\gamma_s M_\infty^2)}\right)\left\{\frac{\gamma_s}{\gamma_s+1}[1+\frac{V_e}{a_t}\sin(90°-\varepsilon)] + \left(\frac{1}{\gamma_s+1}\right)\right\}$$

where the last two terms are approximately one for normal sonic injection. This reduces the expression for sonic injection to

$$A^* = F_{jo}/q_1$$

or

$$\frac{h}{d_t} = \left(\frac{A^*}{A_t}\right)^{\frac{1}{2}} = \left(\frac{F_{jo}}{q_1 A_t}\right)^{\frac{1}{2}} \tag{7}$$

Crist, Sherman and Glass [Ref. 4] obtained a good fit between analytical and experimental results with the expression

$$h_D/d_t = 0.71\ (P_{st}/P_D)$$

or, from Equation (5)

$$h_D/h^* = 0.71\ (P^*/P_D)$$

which led to the expression for $\varepsilon = 90°$.

$$h_D/d_t = \frac{3}{4}\left(\frac{F_{jo}}{q_1 A_t}\right)^{\frac{1}{2}} = \frac{3}{4}\left(C_{fo}\right)^{\frac{1}{2}}\left(\frac{P_{st}}{q_1}\right)^{\frac{1}{2}} \qquad (8)$$

3. Penetration Height as a Function of Secondary Mach Number

Schetz and Billig [Ref. 5] propose a theoretical relationship between the values of h for varying M_s which is based on the ratio of dynamic pressure at initial injection conditions to that at mainstream conditions. For $\gamma_s = 1.4$ the following relationship between penetration height at $M_s = 1.0$ and that for M_s greater than 1.0 was obtained

$$\frac{h}{h_1} = \frac{1.2 M_s^{\frac{1}{2}}}{1+0.2 M_s^2}$$

where h_1 is the penetration height at sonic injection.

B. SHOCK SHAPE AND SIDE FORCE PREDICTION

1. Blast Wave Analogy

Hayes [Ref. 6] and Lees and Kubota [Ref. 7] proposed a similarity between hypersonic flow about an unyawed, axisymmetric body and the detonation of a line charge. In general, this similarity is based upon correlating the time

dependent pressure, density and velocity fields which are generated by the explosion of a line charge with the similar field, generated as a function of axial distance over the velocity of the undisturbed flow, about a body in a steady hypersonic flow. In their blast wave analogy approaches to the solution of the secondary injection problem, Broadwell [Ref. 8] and Dahm [Ref. 9] have employed this similitude concept and Sakuri's [Refs. 10 and 11] solutions to the flow fields behind blast waves resulting from the explosion of line charges of uniform energy per unit length. Two basic assumptions are common to the development of both Broadwell and Dahm. The first is that the injectant gas profile is equivalent to a blunt nosed body and the second that the pressure field between the shock and a blunt nosed body is correctly predicted by the blast wave theory. The first assumption has been justified by the observed similarity of the pressure fields about blunt bodies to those generated by flat plate injection. The second is less tenable in that it does not hold strictly true where hypersonic flow assumptions do not apply, i.e., near the nose of the blunt body or equivalent and at mainstream Mach numbers not in the hypersonic range. Both Dahm and Broadwell assume also that at some point not far down stream the injectant gas has been accelerated to the mainstream velocity.

The energy per unit length of line charge in the blast wave theory may be considered analogous to the energy

added to the flow by the injectant. Broadwell's development considers this energy term to be composed of the secondary momentum change resulting from acceleration of the injectant to the mainstream velocity plus the energy generated by the volume addition associated with injection. Dahm derived this analogous energy term directly from thermodynamic considerations with the assumption of negligible mixing of primary and secondary streams.

In the blast wave theory, a full 360° cylindrical shock wave is considered while in the case of secondary injection, where the flat plate is a plane of symmetry, only a half-cylinder shock wave is formed. Therefore, the analogous energy term becomes

$$E = 2E'$$

where E is the energy per unit length required for blast wave formation.

Sakuri relates a characteristic radius, R_o, to the blast wave energy and primary static pressure by:

$$R_o = (E/2\pi P_\infty)^{\frac{1}{2}} \tag{10}$$

The energy term as derived by both Broadwell and Dahm is of the general form

$$E = 2\dot{m}_s V_p \omega_2 \tag{11}$$

Broadwell, by use of previously mentioned assumptions, ascribed to ω_2 the expression,

$$\omega_2 = 1 + \left(\frac{1+\frac{\gamma_p-1}{2}M_\infty^2}{(\gamma_p-1)M_\infty^2}\right)\left(\frac{m_p T_{st}}{m_s T_{pt}}\right) \qquad (12)$$

whereas, from thermodynamic considerations, Dahm developed the form

$$\omega_2 = \frac{1}{2} + \frac{1}{\gamma_p(\gamma_p-1)M_\infty^2} + \frac{\gamma_s}{\gamma_s-1}\left(\frac{1+\frac{\gamma_p-1}{2}M_\infty^2}{\gamma_p M_\infty^2}\right)\left(\frac{m_p T_{st}}{m_s T_{pt}}\right)$$

$$+ \left(\frac{\gamma_s m_p T_{st}}{\gamma_p m_s T_{pt}}\right)^{\frac{1}{2}} \frac{M_s}{M_p}\left(1+\frac{\gamma_p-1}{2}M_\infty^2 \Big/ 1+\frac{\gamma_s-1}{2}M_s^2\right)^{\frac{1}{2}} \cos\varepsilon \qquad (13)$$

where ε is the angle between the primary flow direction and the injection axis.

For normal injection, with which Broadwell was exclusively concerned, the expressions in Equations (12) a and (13) have been noted to be quite similar in form although their origins differ considerably in concept. Henceforth, ω_2 will be used here exclusively as expressed by Dahm in Equation (13). Therefore,

$$\omega_2 = E/2\dot{m}_s V_p$$

and Equation (10) becomes

$$R_o = (\omega_2 \dot{m}_s V_p/\pi P_\infty)^{\frac{1}{2}} \qquad (14)$$

Taking

$$\bar{R} = R/R_o$$

$$\bar{x} = x/R_o$$

$$t = x/V_p$$

where R is the radius of the interaction shock or bow shock at x. The shock radius predicted by blast wave theory is given by Sakuri as

$$\left(\frac{a_\infty}{V_j}\right)\left(\frac{1}{\bar{R}}\right)^2 = J_o \left[1 + \lambda_1 \left(\frac{a_\infty}{V_j}\right)^2 + \frac{1}{2}\lambda_2 \left(\frac{a_\infty}{V_j}\right)^4 + \ldots\right] \quad (15)$$

where J_o is the first order blast wave constant, λ_k are higher order blast wave constants, V_s is the shock velocity, and a_∞ is sonic velocity in the undisturbed mainstream. Solution of Equation (15) yields

$$R = [2aR_o/J_o^{\frac{1}{2}}]^{\frac{1}{2}}$$

or, for the first order theory,

$$\bar{R} = [2/J_o^{\frac{1}{2}}]^{\frac{1}{2}} \left(\bar{x}/M_\infty\right)^{\frac{1}{2}}$$

and, for the second order theory,

$$\bar{R} = \left(\frac{2}{J_o^{\frac{1}{2}}}\right)^{\frac{1}{2}} \left(\frac{\bar{x}}{M_\infty}\right)^{\frac{1}{2}} \left[1 + \frac{b}{2J_o^{\frac{1}{2}}} \left(\frac{\bar{x}}{M_\infty}\right)\right]^{\frac{1}{2}} \quad (16)$$

The theoretical bow shock shape for any given set of injection parameters can thus be determined.

In Broadwell's development, the interaction force is described by

$$F_w = 2 \int_0^L \int_0^R (P-P_\infty)\, dr dx$$

where

$$P = P\ [P_\infty, J_o, M_\infty, \bar{x}, g(\eta)]$$

which yields

$$F_w = F\ [E, J_o, L, g(\eta)]$$

where $g(\eta)$ is a non-dimensional pressure ratio.

In a similar fashion, Dahm developed the expression for second order theory interaction side force

$$\frac{F_i}{P_\infty A_t} = \left(\frac{12\omega_2^{3/2} M_\infty k_1}{\pi^2 J_o^{3/2}}\right)^{1/2} \left(\frac{s}{d_t}\right)^{1/2} \left(\frac{\dot{m}_s V_p}{P_\infty A_t}\right)^{3/4}$$

This expression applies only at small values of the blast wave analogy parameter $s/R_o M_\infty$ (less than 0.0654 according to Cassel, Davis and Engh). For larger values of this parameter, i.e., for lower mass flow rates, the following relationship was developed in Ref. 9 for circular port injection

$$F_i = (2/\pi)\omega_2 \dot{m}_s V_p M_\infty z \qquad (17)$$

where

$$z = \frac{k_1}{2J_o^{1/2}} \left[\left(\frac{1}{b^{1/2}} + \frac{J_o k_2}{k_1 b^{3/2}}\right)\left(\frac{\phi}{b^{1/2}}\right)\sqrt{1+\frac{\phi^2}{b}} + \left(\frac{1}{b^{1/2}} - \frac{J_o k_2}{k_1 b^{3/2}}\right) \ln\left(\frac{\phi}{b^{1/2}} + \sqrt{1+\frac{\phi^2}{b}}\right)\right]$$

in which $b = -J_o\lambda_1$, and $\phi = b\bar{R}$ when $\bar{R}$ is evaluated at s. Reference 9 evaluates $k_1 = 0.4973$ and $k_2 = -1.103$ for $\gamma_p = 1.4$.

2. Upstream Model

Consideration of the secondary injectant as being analogous to a blunt nosed obstacle in the primary stream lead to the two-dimensional upstream model of Vinson, Amick and Liepman [Ref. 12]. Here the weak shock formed by boundary layer separation in the high pressure region ahead of the secondary stream or the analogous blunt body yields the equivalent penetration height of the secondary injectant. The penetration height thus determined, the boundary layer detachment angle, the mainstream pressure and the pressure behind the shock in turn yield the magnitude of the interaction side force developed.

Wu, Chapkis and Mager [Ref. 13] extended the previous model to three dimensions by assuming that the separation region ahead of the secondary nozzle is conical. Their model of the interaction phenomena leads to the expression:

$$F_i/F_j = \frac{\cos\alpha \tan\theta}{\pi} \{\cot\delta + \tan(\alpha+\varepsilon')\}^2 \sqrt{2}\ \gamma_s \sqrt{2/(\gamma_s+1)}$$

$$\cdot\{(\frac{P}{P_1} - 1)/[2\gamma_s + (\gamma_s-1)(\frac{P}{P_1} - 1)]\}^{\frac{1}{2}} \qquad (18)$$

where α is the primary nozzle half angle and is zero for the purposes of this paper, $\varepsilon' = 90-\varepsilon$, P is the pressure in the area of the detached region ahead of the bow shock, δ the

boundary layer attachment angle and θ the associated conical shock angle.

3. Downstream Model

Walker, Stone and Shandor [Ref. 14] propose a model in which the immediate mixing with the mainstream gas of a low flow rate injectant in a constant area is suggested. After mixing, the gas is assumed to expand isentropically to the mainstream pressure thus inducing a side force. The following expression for side force is obtained:

$$\frac{F_i}{F_j} = \frac{\cos \alpha \gamma_p^{\frac{1}{2}} M_\infty}{[2(M_\infty^2 - 1)]^{\frac{1}{2}}} \left(1 + \frac{\gamma_p - 1}{2} M_\infty^2\right)^{-\frac{1}{2}} \left(\frac{\gamma_s}{\gamma_s + 1}\right)^{\frac{1}{2}} \left(\frac{m_s T_{pt}}{m_p T_{st}}\right)^{\frac{1}{2}} G \qquad (19)$$

where

$$G = 1 + \frac{\gamma_s - 1}{2} M_\infty^2 - \left\{\frac{m_p}{m_s} - \frac{m_p T_{st}}{m_s T_{pt}} \left(1 + \frac{\gamma_p - 1}{2} M_\infty^2\right)\right\} \frac{\gamma_s}{\gamma_p} \left(\frac{\gamma_p - 1}{\gamma_s - 1}\right)$$

$$+ \frac{m_p}{m_s} + \left\{\left(\frac{m_p T_{st}}{m_s T_{pt}}\right)^{\frac{1}{2}} \left(\frac{2\gamma_s}{\gamma_s + 1}\right)^{\frac{1}{2}} \left(\frac{1 + \frac{\gamma_p - 1}{2} M_\infty^2}{\gamma_p}\right)^{\frac{1}{2}}\right\}$$

$$\cdot \left[1 + (\gamma_p - 1) M_\infty^2\right] \frac{\sin(\alpha + \varepsilon)}{M_\infty}$$

IV. DESCRIPTION OF THE EXPERIMENT

A. PARAMETERS

The secondary nozzles constructed for use in this experiment were of Mach numbers 1.00, 1.73 and 2.13. A description of the calibration of the supersonic nozzles is contained in Appendix A. The throat diameter of all nozzles was a nominal 0.100 ± 0.001 inches. Nominal inclination angles of 90°, 80°, 70°, 60° and 50° were tested at each injection Mach number.

During all runs, the primary flow Mach number remained constant at $M_\infty = 2.80$. The primary total pressure was a constant 50.0 psia. In successive closely spaced runs, the primary total temperature decreased slightly as the tunnel walls were cooled by the flow. This temperature decrease was slight, having an overall variance of ± 15°F from the mean total primary temperature for all runs. For purposes of the interpretation of the results of the theoretical computations involving the primary flow parameters, this temperature variation was considered negligible.

The secondary total pressure was increased by increments of 25.0 psia from 25.0 to 250.0 psia providing a series of ten secondary-to-primary total pressure ratios for each of the 15 nozzles tested. The secondary gas reservoir total temperatures varied only slightly due to minor fluctuations in the ambient temperature over the period of the testing.

Therefore, the total temperature of the secondary flow after it was throttled to the desired total pressure also varied slightly. This effect was also neglected for purposes of interpretation.

B. EXPERIMENTAL PROCEDURE

The test runs were conducted in ascending order of M_s and at a given secondary Mach number in descending order of ε. Ten runs were conducted at each nozzle configuration at the previously described total pressure ratios using nitrogen as the secondary gas. Two nozzle configurations ($M_s = 1.0$, $\varepsilon = 90°$ and $M_s = 1.73$, $\varepsilon = 68°$) were tested similarly with argon and helium as the secondary injectant.

Individual runs averaged less than one minute in duration. During each run the following observations were made:

1. The static pressure at each of the 47 flat plate pressure taps was measured by a Scanivalve and recorded on a Visicorder.
2. The differential pressure through the flowmeter was measured by a differential pressure transducer and recorded on a Visicorder.
3. The upstream flowmeter pressure was measured by pressure gauge.
4. The injection total pressure was measured by pressure gauge.

5. The primary total pressure was measured by pressure gauge.
6. The total temperature of the secondary flow through the flowmeter was sensed by a chromel-alumel thermocouple and displayed on a millivoltmeter.
7. Primary total temperature was sensed by a chromel-alumel thermocouple and displayed on a millivoltmeter.
8. A Schlieren photograph was taken of the test section.

As described earlier, the total temperature of the secondary flow at the flowmeter was taken to be the injection total temperature.

Tare pressures were observed at the plate surface with the tunnel operating but without secondary injection. These were then subtracted from the respective pressures measured during injection to determine the interaction pressure rise. This pressure rise was then integrated over the plate surface for determination of the interaction side force. Tare observations were made prior to each of the series of 10 runs for a given nozzle configuration. In all cases, tare pressures were observed with a nozzle for normal injection installed.

Penetration heights and bow shock coordinates were measured by projecting the negatives of Schlieren photographs onto a measuring grid. The grid was constructed to

twice the actual scale of the model and reference points were provided to insure that the grid was properly oriented with respect to the projection of the negative.

In order to determine the effect of the protrusion of the downstream side of the nozzles at $\varepsilon < 90°$, a duplicate sonic normal nozzle was constructed. A dummy obstruction representing the protrusion of an inclined nozzle was then inserted just downstream of the normal sonic nozzle orifice. This nozzle was tested in order to determine the effect of the obstruction on the pressure distribution over the plate and on penetration height.

A normal sonic nozzle was constructed with a cylindrical constant area throat section 0.01 inches in length and tested for comparison with the sharp-edged-throat nozzles used in this experiment

V. EXPERIMENTAL RESULTS

A. PENETRATION HEIGHT

Zukoski and Spaid have stated that the height of penetration of the secondary gases into the main flow is a dimension characteristic of the scale of the interaction disturbance. This parameter, non-dimensionalized by the nozzle throat diameter and the square root of the nozzle discharge coefficient (i.e., by the effective nozzle throat diameter) has been utilized by previous investigators [Refs. 1, 15 and 16] to correlate injection penetration height with secondary-to-primary total pressure ratios for normal, sonic injection.

In this experiment, the discharge coefficient was found by dividing the actual flow rates through the nozzles by the corresponding mass flow rate calculated for ideal gas assuming isentropic flow. The actual flow was measured by means of a sharp-edged orifice flowmeter placed in the injectant supply line. The flowmeter was constructed and the flow through it evaluated in accordance with Ref. 17. Discharge coefficients thus obtained are shown versus the inverse square root of nozzle throat Reynolds number in Figures 10, 11, and 12. These results are in general agreement with the discharge coefficients of similar nozzles determined by Amick and Hays [Ref. 16] and by Chrans and Collins [Ref. 15].

As described in detail earlier, measurements of the penetration heights were taken from the Schlieren photographs which were made of each run. This dimension was measured along a normal from the surface of the flat plate to the point of highest penetration of the secondary flow.

For injection at a given Mach number, penetration height correlations in non-dimensional plots of $(h/d\sqrt{c})\sin\varepsilon$ versus $(P_{st}/P_{pt})\sin\varepsilon$ for all ε were obtained. The results are shown in Figures 13, 14 and 15. For the special case of normal ($\sin\varepsilon = 1$), sonic injection Figure 13 is equivalent to a plot of $h/d\sqrt{c}$ as a function of P_{st}/P_{pt} which, as stated earlier, has seen previous use. The present application extends the generality of the earlier correlation.

From Figures 13, 14 and 15 it can be seen that

$$\left(\frac{h}{d\sqrt{c}}\right)\sin\varepsilon = \left[\left(\frac{P_{st}}{P_{pt}}\right)\sin\varepsilon\right]^{\beta}$$

where the exponent β varies with Mach number. In Figure 13, β was found to be approximately equal to 0.53. This was in close agreement with the value of $\beta = 0.5$ in the theoretical development of Zukoski and Spaid for normal sonic injection. As can also be seen in Figure 13, the observed data agrees closely with the theoretical penetration height for normal, sonic injection of Cassel, Davis and Engh. The Riemann disc height as a function of pressure ratio for an underexpanded sonic nozzle exhausting into still air as determined in Ref. 18 is also shown in Figure

13. This curve agrees closely with both the observed and the theoretical correlations.

As expressed by Schetz and Billig in Equation (9), the penetration height is expected to increase as a function of Mach number. In Figures 13, 14 and 15 this is borne out in a qualitative sense. Figure 16 is a reproduction of the mean lines defined by the data in the preceding three figures. As shown in this figure, the penetration height does increase with increasing secondary Mach number. However, values of the exponent β are also seen to increase. As indicated by the theoretical plots also shown in Figure 16, this was not predicted by Schetz and Billig. At $M_s = 1.73$ the observed value of β is approximately 0.62 and at $M_s = 2.13$ approximately 0.63.

B. SHOCK SHAPE

Dahm and Broadwell suggest that the characteristic radius R_o is a dimension representative of the scale of the interaction. Dahm has shown theoretically that a non-dimensional plot of $x/R_o = \bar{x}$ versus $R/R_o = \bar{R}$ provides correlation of bow-shock coordinates. Experimental verification of this correlation for normal sonic injection was obtained by Chrans and Collins with variations in mass flow rate and secondary-to-primary total temperature ratio. The present study has shown that these coordinates are not sufficiently general. Simultaneous correlation is not achieved when data is collected at various values of inclination angle ε. As

shown for nitrogen injection in Figures 17 through 30, it was, however, found that bow shock shape correlated in a plot of $\bar{x}$ versus $\bar{R}$ for any specific ε. Correlation with respect to all values of epsilon was obtained by plotting shock shapes in the non-dimensional coordinates $\bar{x} \sin \varepsilon$ versus $\bar{R} \sin \varepsilon$. For normal injection, where $\sin \varepsilon = 1$, the coordinates in effect revert to $\bar{x}$ and $\bar{R}$. Bow shock shapes are correlated in this manner in Figures 31, 32, and 33 for nitrogen, argon and helium injected at a secondary-to-primary total pressure ratio of 3.0. It can be seen from the previous data correlations for various pressure ratios in Figures 17 through 30 that the results here are representative of all pressure ratios.

The data scatter in Figures 31, 32, and 33, although coherent, is separated to a slight degree with respect to secondary Mach number. In general, the data representing injection at $M_s = 2.13$ lie along the upper bound of the scatter band, that for $M_s = 1.73$ in the center and the data for sonic injection along the lower bound. The parameter R_o, by which bow-shock coordinates were non-dimensionalized in these figures, was calculated from Equation (14) in which R_o is a function of ω_2. As can be seen from Equation (13), ω_2 is a function of M_s only for $\varepsilon < 90°$. This dependence on M_s is sufficient to cause shock shapes to correlate very closely for all ε at a given M_s. Correlation at differing values of M_s is, however, not so precisely obtained. In the previous section, h was suggested as a

characteristic dimension representative of the scale of the disturbance. In Refs. 1 and 15 bow shock shape correlation for the case of normal, sonic injection was obtained by plotting $x/h = x'$ versus $R/h = R'$. Correlation of shock shapes for all inclination angles was obtained in Figure 34 by plotting $R' \sin \varepsilon$ versus $x' \sin \varepsilon$. For normal injection ($\sin \varepsilon = 1$) these coordinates are identical with the coordinates previously used for correlation of shock shapes formed by normal sonic injection. It was found that when correlated in this manner, the data for various secondary Mach numbers was randomly distributed throughout the scatter band rather than forming obvious subgroups by M_s within it as was the case when shock coordinates were non-dimensionalized by R_o.

The mean lines representative of the shock shape correlation data in Figures 31, 32, and 33 (for nitrogen, argon and helium) are reproduced for comparison in Figure 35. The dependence of shock shape on molecular weight previously noted by Chrans and Collins is seen. At a given value of $\bar{x} \sin \varepsilon$ the non-dimensional radius, $\bar{R} \sin \varepsilon$ increased with increasing secondary molecular weight. Blast wave theory does not indicate such a dependence. It has been suggested [Ref. 15] that the mixing of the secondary gases with the primary stream (assumed to be negligible in the development of the blast wave analogy) may account for this dependence.

When plotted in terms of x' sin ε versus R' sin ε, the same molecular weight dependence is shown.

C. SIDE FORCE

An experimental examination of the interaction side force developed by secondary injection was also conducted. Side forces on the flat plate were calculated from the interaction pressure rise on the plate surface as detailed earlier. The interaction side force was calculated for all runs.

In this study, side forces are presented in the form of a non-dimensional force amplification factor A. The amplification factor is defined as

$$A = \frac{F_i + F_j \sin \varepsilon}{F_j \sin \varepsilon}$$

which relates the interaction side force to the component of secondary nozzle thrust normal to the plate surface. Reproducibility of the observed values of A were consistently good. Figure 36 (a) shows representative data scatter in a plot of A versus primary-to-secondary total pressure ratio.

In order to prevent disruption of the symmetry of the secondary flow by the physical hardware of the model, all nozzles were constructed with the upstream edge of the nozzle exit planes coincident with the plate surface. As a result, the downstream edge of the nozzles protruded slightly into the primary flow. It was necessary to

determine the effect of this protrusion. A sonic, normal nozzle was constructed with an obstruction representing an inclined nozzle installed immediately downstream of the nozzle orifice. This nozzle was then tested for comparison with the normal sonic nozzle used in the experiment. The values of A at various injection pressure ratios thus obtained agreed within the normal experimental scatter encountered. A normal sonic nozzle having a short (0.01 inches) cylindrical, constant area throat (square edged) was also tested for comparison with the sharp edged nozzles used in this experiment. The amplification factors were found to agree within the bounds of anticipated scatter. The results of these comparisons are shown in Figure 36 (b). Schlieren photographs showed no difference in either bow shock shape or penetration height in these comparisons of nozzle configuration.

In the development of their blunt body models, Zukoski and Spaid, and others [Refs. 2 and 8] suggest that the characteristic length is a function of the change in momentum experienced by the secondary gases.

As has been shown earlier, penetration height increases as epsilon decreases (i.e., as the upstream component of momentum increases) when all other parameters are held constant. It is, therefore, to be expected that as the scale of the disturbance increases the interaction side force will increase accordingly. In Figure 37, at a representative secondary-to-primary total pressure ratio of

3.0, a plot of interaction side force versus epsilon is shown. It may be seen that a decrease in epsilon is accompanied by an increase in observed side force. This figure also shows a decreasing trend in interaction side force as M_s increases. The interaction side force for sonic injection and that for injection at $M_s = 1.73$ at various values of ε are nearly equal. For injection at $M_s = 2.13$, however, a decrease in observed side force occurs. This decrease is not predicted by Dahm. Reference 5 suggests that the gains which theoretically appear to be associated with supersonic injection may be countered by the losses involved in turning a supersonic secondary jet downstream. The turning of a sonic secondary jet is largely shock free and the losses are thus small compared to the turning of a supersonic jet.

In Figures 38, 39, and 40, interaction side force is plotted in terms of the nondimensional force amplification factor A versus secondary-to-primary total pressure ratio. The amplification factor A, at a given value of pressure ratio, is seen to increase with decreasing epsilon. Part of this increase is due to the decreasing value of the normal component of jet thrust ($F_j \sin \varepsilon$) as ε decreases and part is due to the increasing value of F_i as ε decreases which is shown in Figure 37.

It is noted in Ref. 19 that an empirical correction factor of 0.51 when applied to Dahm's second order theory values of side force provides a semi-empirical value of

side force very nearly comparable with previous experimental data. The shaded areas on Figures 38, 39 and 40 represent the region of the value of A computed from this semi-empirical correction to Dahm's theory. It can be seen that considerable data scatter exists in the area of low injection pressure ratios and that observed and semi-empirical values differ considerably. Conversely, at the higher pressure ratios, scatter decreases and agreement with the semi-empirical values of A improves considerably. Also, as M_s increases, a comparison of Figures 38, 39 and 40 shows that overall data scatter decreases and overall agreement with the semi-empirical values of A increases.

In Figures 41, 42 and 43, the data shown in Figures 38, 39 and 40 is presented in a more general manner. The previously observed successes in correlation of parameters suggest, as ε is varied, that all features of the flow scale by sin ε when properly non-dimensionalized. A degree of correlation was achieved in Figures 38, 39, and 40 in a plot of A sin ε versus $\dot{m}_s V_j$ sin ε. Again, at lower values of $\dot{m}_s V_j$ sin ε (i.e., lower injection pressure ratios) data scatter is pronounced and agreement with empirically corrected theory is not good. As $\dot{m}_s V_j$ sin ε increases, however, data scatter decreases and agreement with the corrected theory continually improves. As M_s increases, comparison of Figures 41, 42 and 43 also shows considerable improvement in the degree of correspondance of data with the curve representing the semi-empirical values of A.

The degree to which observed values of side force agree with the side force actually developed is a function of the fineness of the grid spacing of the pressure taps. It was found in this experiment that both data scatter and disagreement with corrected theory were pronounced at the lower values of injection pressure ratio (or the related lower values of $\dot{m}_s V_j \sin \varepsilon$). In this area of operation, the characteristic length h was of the order of or less than the average distance between pressure taps. As h increased to a value of the order of twice the pressure tap spacing or greater (i.e., for values of $(P_{st}/P_{pt}) \sin \varepsilon$ greater than 2.0) data scatter decreased and agreement with semi-empirically predicted values of A increased. Above values of $(P_{st}/P_{pt}) \sin \varepsilon > 2.0$ or the corresponding values of $\dot{m}_s V_j \sin \varepsilon > 25$, the data in Figures 38 through 43 is considered reliable. In this area, the data in Figures 41, 42, and 43 shows a consistant degree of correlation which agrees well with expected values.

As determined by Zukoski and Spaid, the surface area ahead of the injector is subjected to the highest interaction pressures developed during secondary injection. It was observed in this experiment that the pressures developed downstream of the injector were generally of little significance in calculating the value of interaction side force. The model of the interaction proposed by Wu, Chapkis and Mager depends exclusively upon flow phenomena upstream of the nozzle for determination of the

interaction side force. A limited investigation of this theory was undertaken. The results of the comparison of observed data and that calculated according to Equation 18 is shown in Figure 44 in a plot a A versus P_{st}/P_{pt}. The calculated values were determined by measuring the boundary layer detachment angle δ from the Schlieren photographs of the respective runs. These measurements were accomplished on an optical comparitor. The shock angle θ was not shown on the photographs with sufficient clarity to permit measurement. Therefore, the value of θ corresponding to a cone of half-angle δ was taken from Ref. 20. The pressure behind the conical shock was also determined from Ref. 20. The results of the computations thus achieved are shown by the curve in Figure 44. The broken portion of the curve represents areas in which photographic quality did not permit accurate measurement of δ. Observed and calculated values agreed closely.

The side force determined by the downstream theory of Walker, Stone and Shandor was evaluated in accordance with Equation 19 for normal sonic injection. The value of A at low values of pressure ratio was found to be of the order of 6, in considerable disagreement with observed and previously computed values.

In Figures 45 and 46, values of A are plotted against pressure ratio and $\dot{m}_s V_j \sin \varepsilon$, respectively, for nitrogen, argon and helium for two different nozzle configurations.

Within the previously encountered range of data scatter, no dependence of A on the molecular weight of the injectant was observed.

VI. CONCLUSIONS

Penetration height increases both with an increase in M_s and with a decrease in ε, all other parameters being held constant. Correlation of penetration height for a given value of M_s is obtained in a plot of $(h/d\sqrt{c})\sin\varepsilon$ versus $(P_{st}/P_{pt})\sin\varepsilon$. For normal sonic injection these coordinates become the familiar $h/d\sqrt{c}$ versus P_{st}/P_{pt}. In the case of sonic injection , the slope of the correlation curve is approximately 0.5, i.e.,

$$\frac{h}{d\sqrt{c}}\sin\varepsilon \propto \left[\left(\frac{P_{st}}{P_{pt}}\right)\sin\varepsilon\right]^{0.5}$$

or for the case of normal sonic injection

$$h/d\sqrt{c} \propto [P_{st}/P_{pt}]^{0.5} \propto (\dot{m}_s)^{0.5}.$$

This is in close agreement with the theories discussed. As M_s increases, the value of the exponent increases. At $M_s = 1.0$ the value of the exponent is approximately 0.53, at $M_s = 1.73$ approximately 0.62 and at $M_s = 2.13$ approximately 0.63.

Non-dimensional bow shock shape plotted in the coordinate set $(\bar{x}, \bar{R})$ remains essentially constant with varying M_s. The non-dimensional radius at a given value of $\bar{x}$ (where x is measured downstream from the nozzle centerline) increases with decreasing ε. Bow shock shapes correlate in non-dimensional plots of $\bar{x}\sin\varepsilon$ versus $\bar{R}\sin\varepsilon$ or $x'\sin\varepsilon$

versus R' sin ε. The correlation curves are coincident with those for normal sonic injection plotted in the coordinates $\bar{x}$ versus $\bar{R}$ or x' versus R'.

The empirical correction factor of 0.51 applied by Dahm to the values of interaction side force calculated from his second order theory was qualitatively substantiated. Correlation of side force data in a plot of A sin ε versus $\dot{m}_s V_j$ sin ε is indicated for all ε and M_s. In order to obtain valid side force data by means of integrating interaction pressure rise over a flat plate, the spacing of the pressure taps should be on the order of or less than one-half the smallest penetration height expected.

Dahm's theory predicts an increase in the magnitude of side force with decreasing ε, all other parameters remaining constant. This was qualitatively confirmed. Side force at a given value of ε was observed to decrease with increasing M_s. Dahm's theory predicts no change with increasing M_s for normal injection and a slight increase in side force with increasing M_s as ε decreases.

For the same values of injectant momentum, the experimental results indicate, within the degree of data scatter expected, that side force does not vary with changes in the molecular weight of the secondary gas. At the nozzle throat, i.e., at choked flow, the secondary mass flow rate is reduced as the molecular weight of the injectant decreases. It is beneficial, therefore, to inject gases of low molecular weight in order to minimize the total weight of secondary fluid which must be carried by the vehicle.

APPENDIX A

SUPERSONIC NOZZLE CALIBRATION

The supersonic nozzles utilized in this experiment were constructed with 10° divergence half-angles on either side of a sharp edged throat. The diameters of the throats of all nozzles were 0.10 ± .001 inches. Throat diameters were held to this tolerance in the following manner. Two carefully manufactured rods were constructed, one having a diameter of 0.10 - .001 = 0.099 inches and the other having a diameter of 0.10 + .001 = 0.101 inches. The 10° half-angle approach portion of the nozzle was drilled out. The portion of the nozzle downstream of the throat was then drilled (also with the 10° half-angle bore) until the smaller diameter rod but not the larger diameter rod was free to pass through the nozzle throat. Thus, the throat diameter was within the diameter difference of the testing rods, or 0.10 ± .001 inches.

The nozzle having the lowest supersonic Mach number was constructed to a nominal area ratio of 1.6900 corresponding to M_s = 1.998 in Ref. 20. The diameter tolerance allowed at the throat was also incurred at the exit plane of the nozzle. The area ratios of the nozzles constructed, therefore, varied between 1.6823 and 1.6979. This causes a Mach number variation between M_s = 1.996 and M_s = 2.001 for one dimensional, inviscid isentropic flow calculations..

The higher Mach number nozzle was constructed to a nominal area ratio of 2.6569 corresponding as above to $M_s = 2.508$. Tolerances in manufacture caused a possible spread in area ratio between 2.6366 and 2.6777 or, in Mach number, between $M_s = 2.500$ and 2.516.

The nozzles, however, are actually three dimensional. Additionally, the viscosity of the secondary gas will cause boundary layer effects to be present, especially downstream of the nozzle throat where a turbulent boundary layer will exist. The nozzle in effect will sense a smaller area ratio than that for which the nozzles were designed. The overall effect is to decrease Mach number observed from that determined by one dimensional, isentropic, inviscid calculations.

Calibration was accomplished by suspending a thin 2.5° half-angle cone (with its apex pointed upstream) in the flow exiting the nozzles. The apex of the cone was centered in the exit plane of the nozzle. Schlieren photographs were then taken of the flow over a range of nozzle flow stagnation-pressure-to-atmospheric-pressure ratios.

The conical shock angles, θ, were measured from the photographs on an optical comparitor. The angles thus determined were $\theta = 35.5° \pm 0.5°$ for the low Mach number supersonic nozzle and $\theta = 28.0° \pm 0.5°$ for the higher Mach number supersonic nozzle. These correspond, respectively,

to M_s = 1.73 ± 0.05 and M_s = 2.13 ± 0.05 from the conical shock curves of Ref. 20.

Taking the actual uncertainty in M_s caused by variation of the physical dimensions in the nozzles to be of the same magnitude as that determined by one-dimensional flow calculations, the nozzles constructed operated at M_s = 1.73 ± .002 and 2.13 ± .008. In comparison with the degree of calibration uncertainty present, the dimensional variation allowed in nozzle construction is, therefore, insignificant.

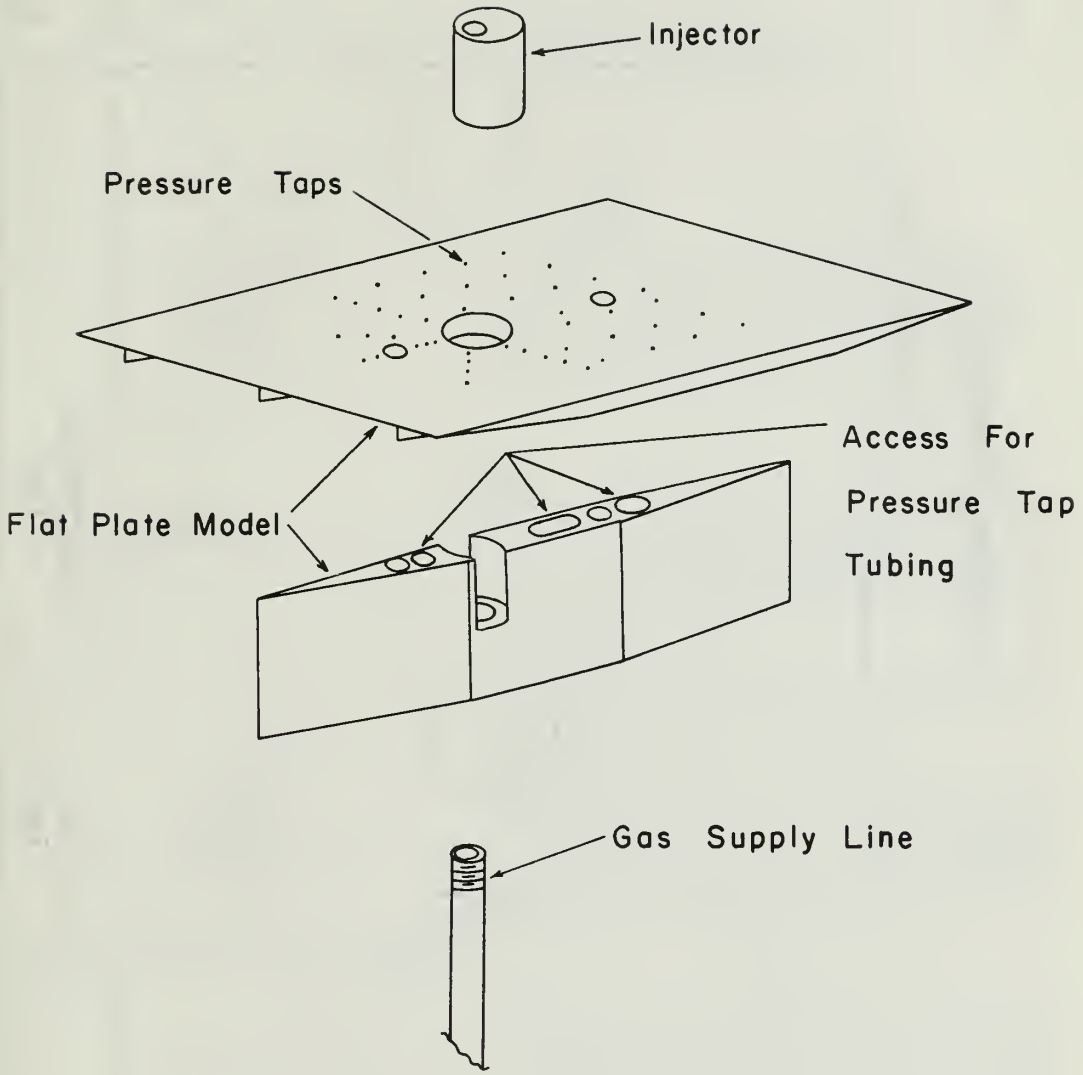

FIGURE 1

EXPLODED VIEW OF MODEL

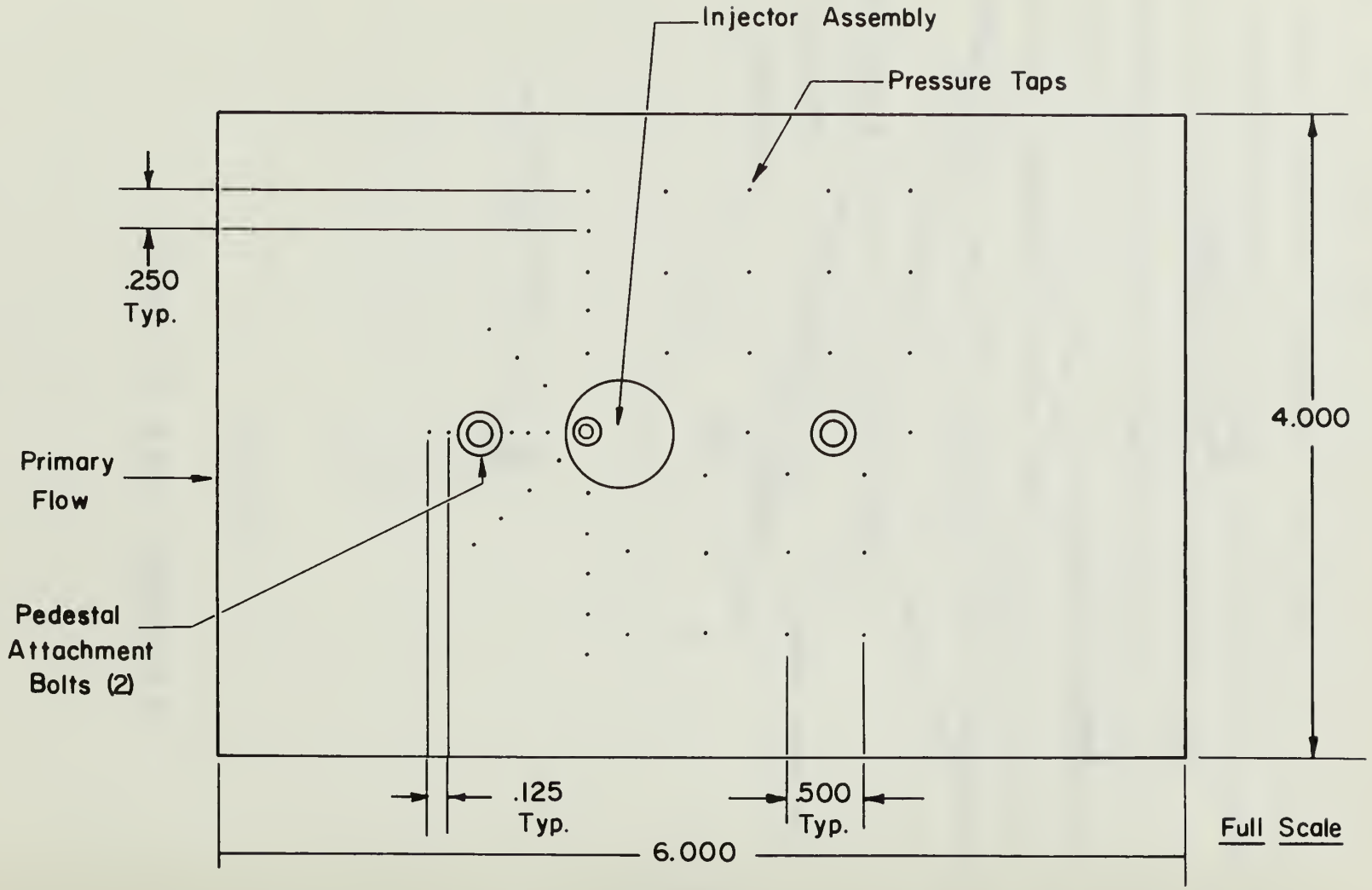

FIGURE 2

TOP VIEW OF FLAT PLATE

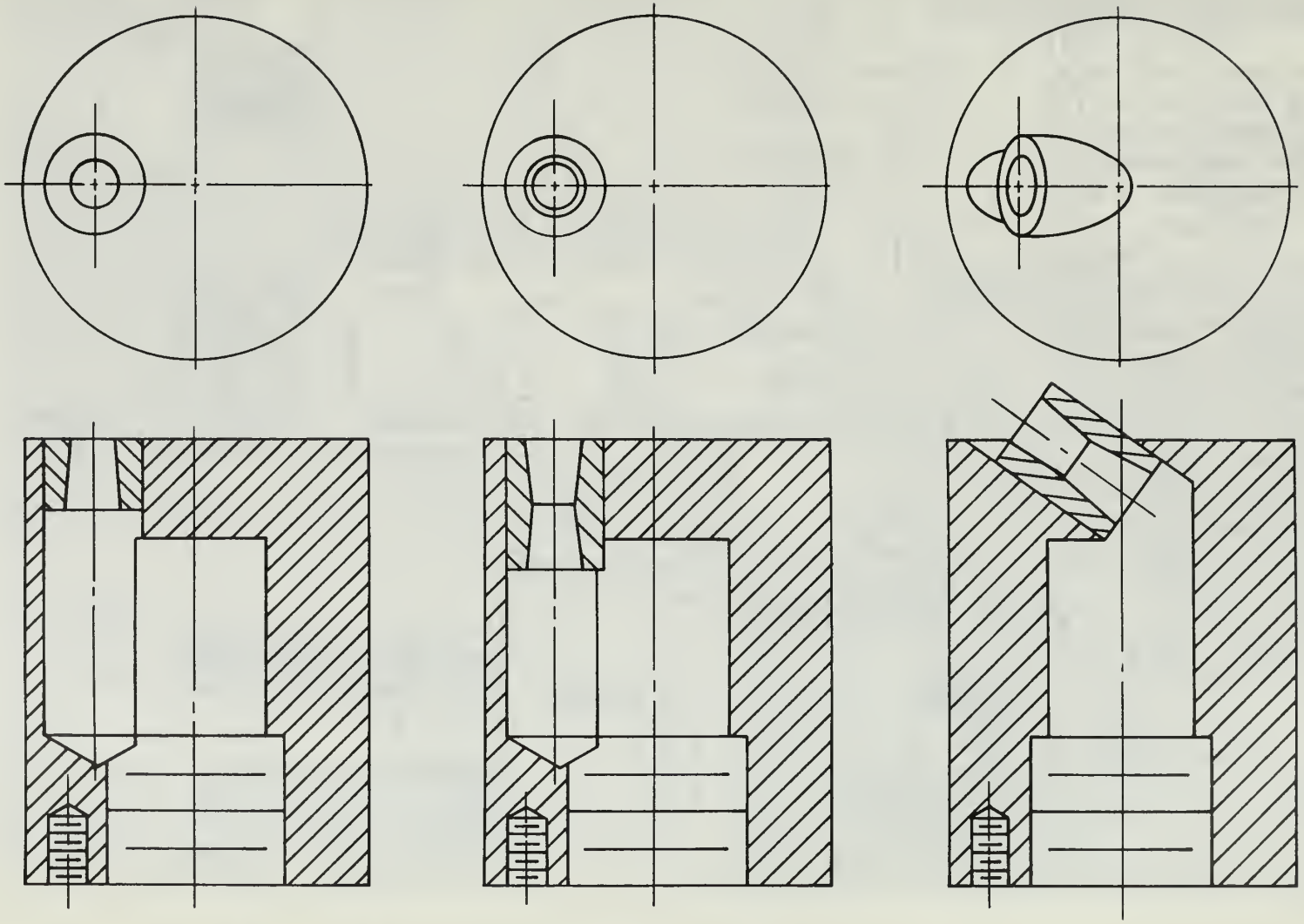

FIGURE 3. TYPICAL NOZZLE DESIGN SCALE = 3:1

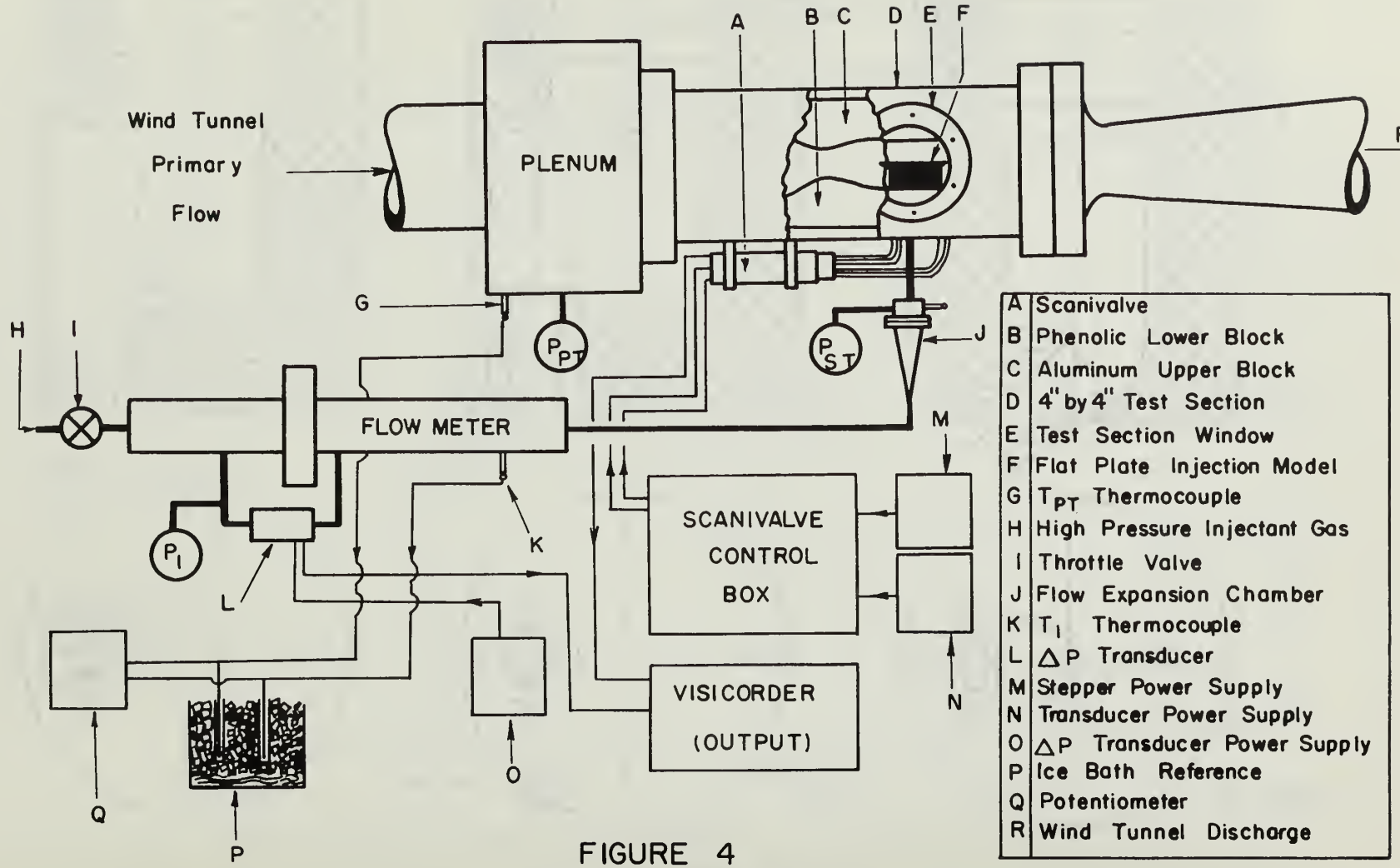

FIGURE 4
EQUIPMENT SCHEMATIC

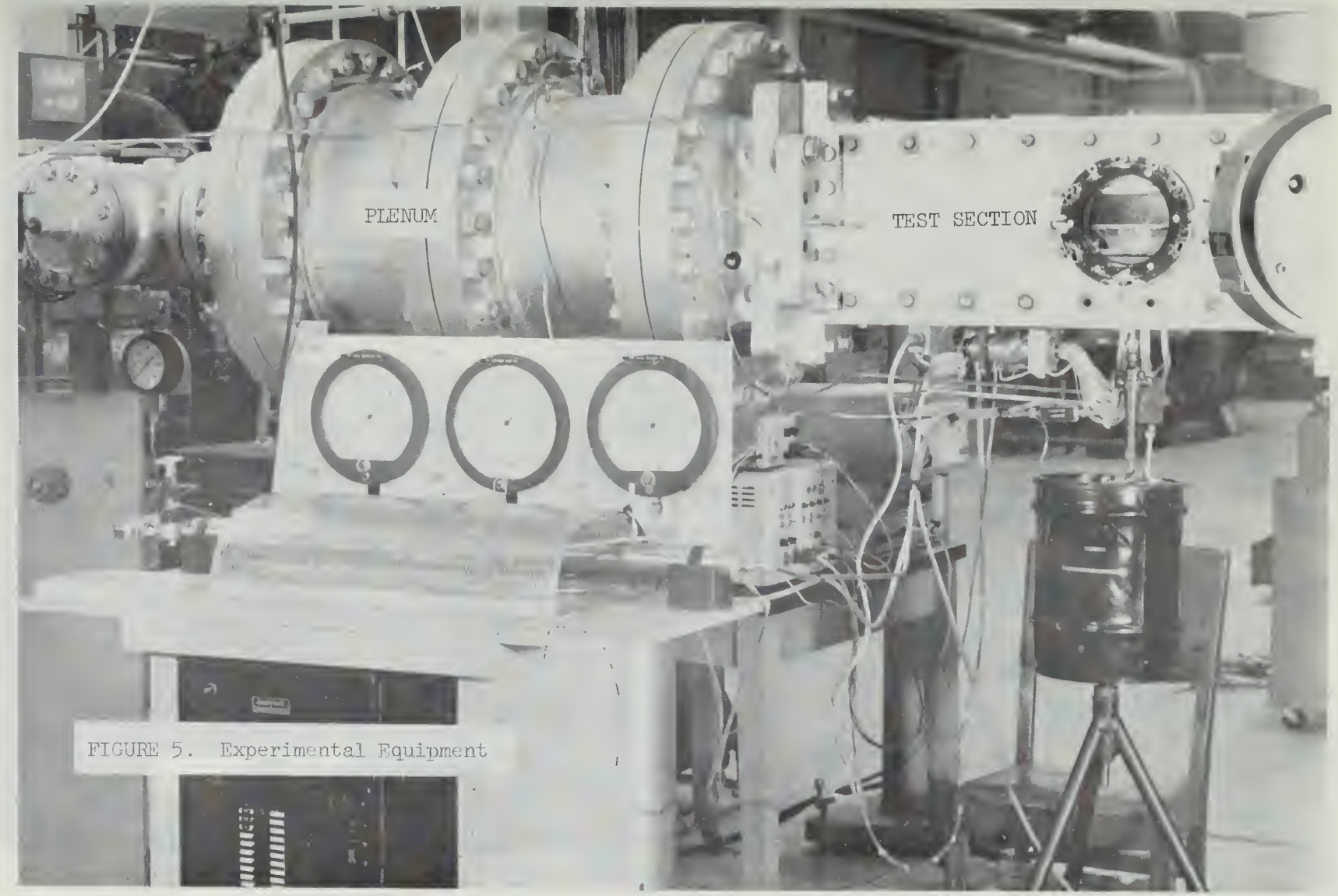

FIGURE 5. Experimental Equipment

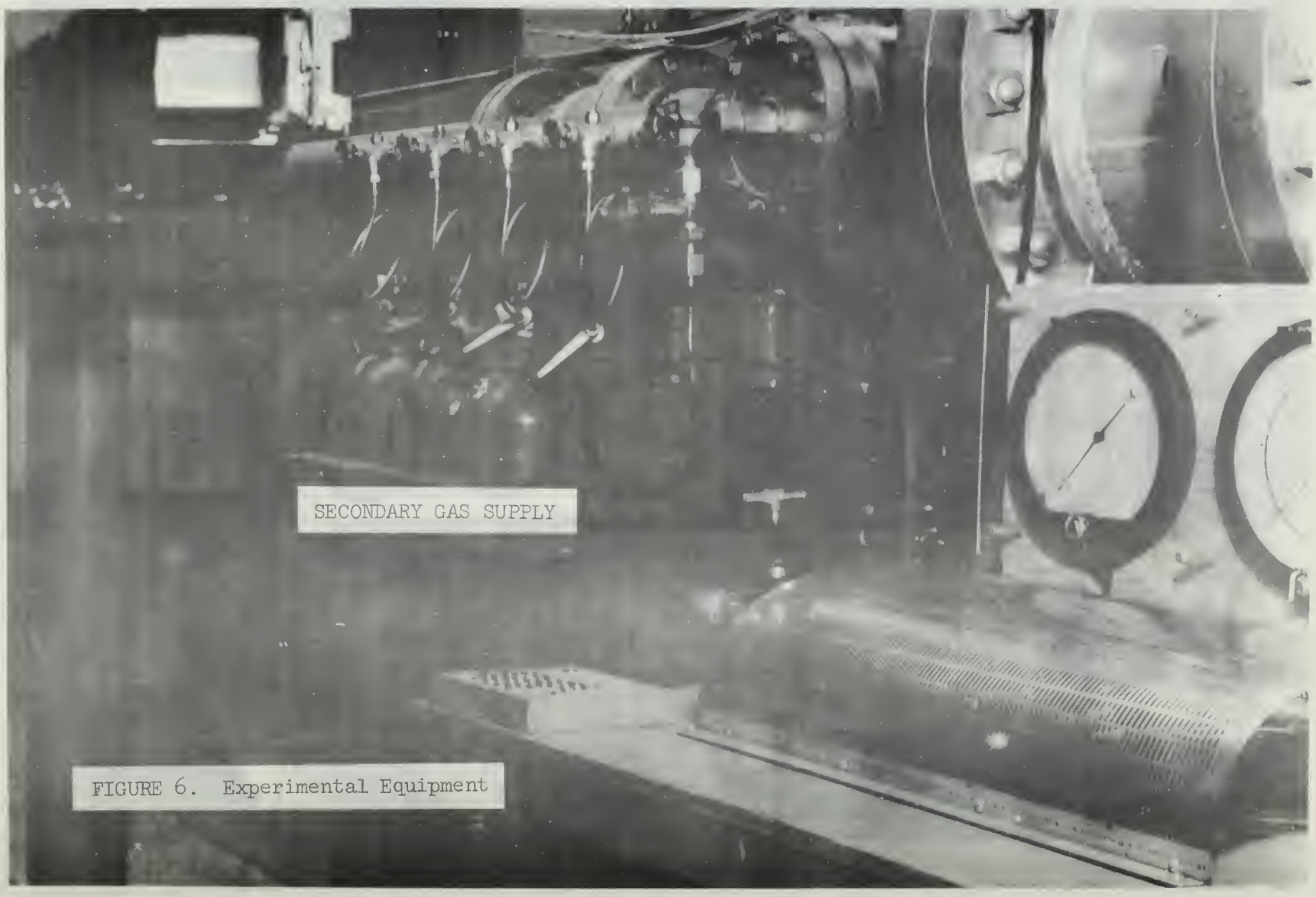

FIGURE 6. Experimental Equipment

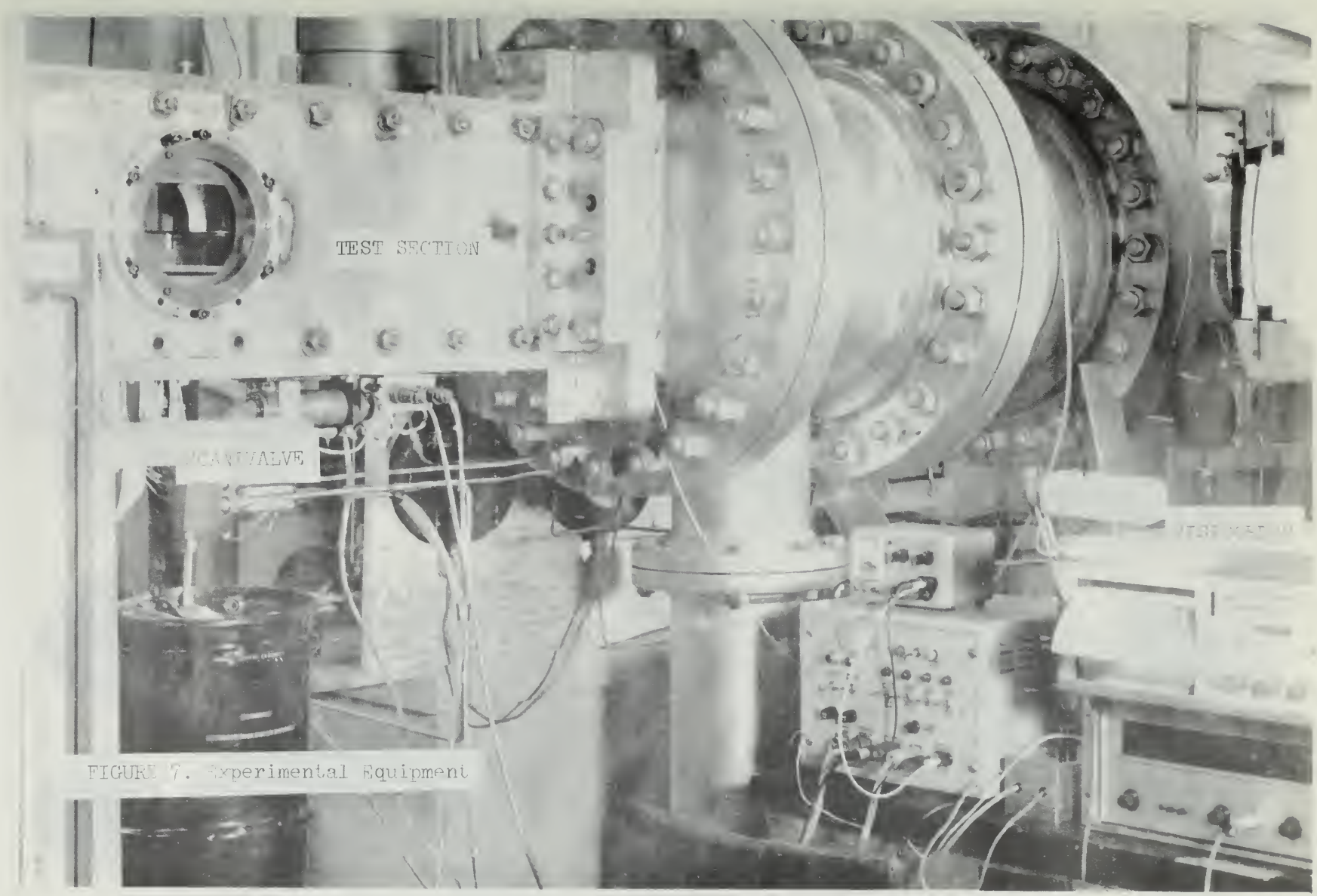

FIGURE 7. Experimental Equipment

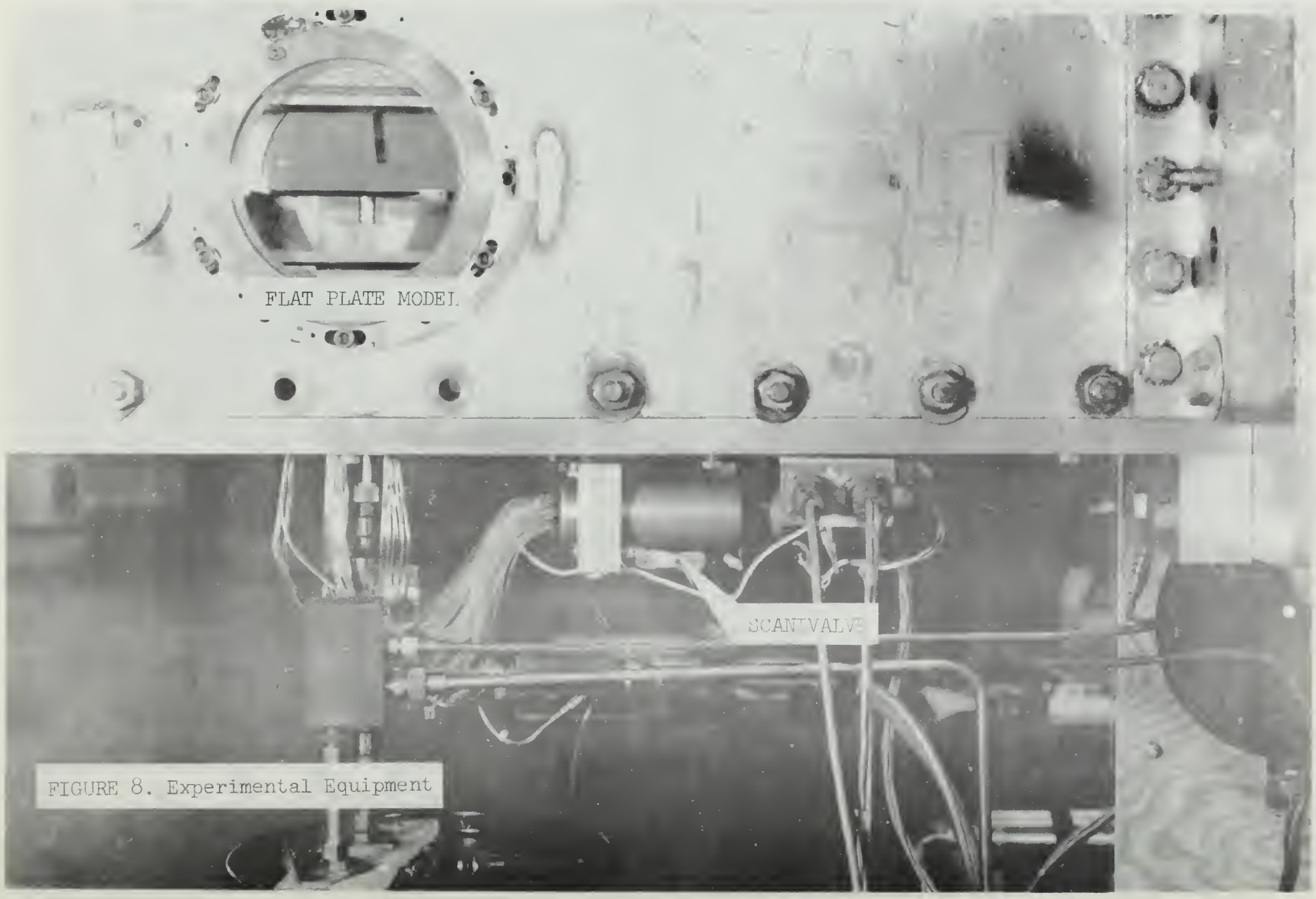

FIGURE 8. Experimental Equipment

FIGURE 9. Interchangeable Nozzle Set

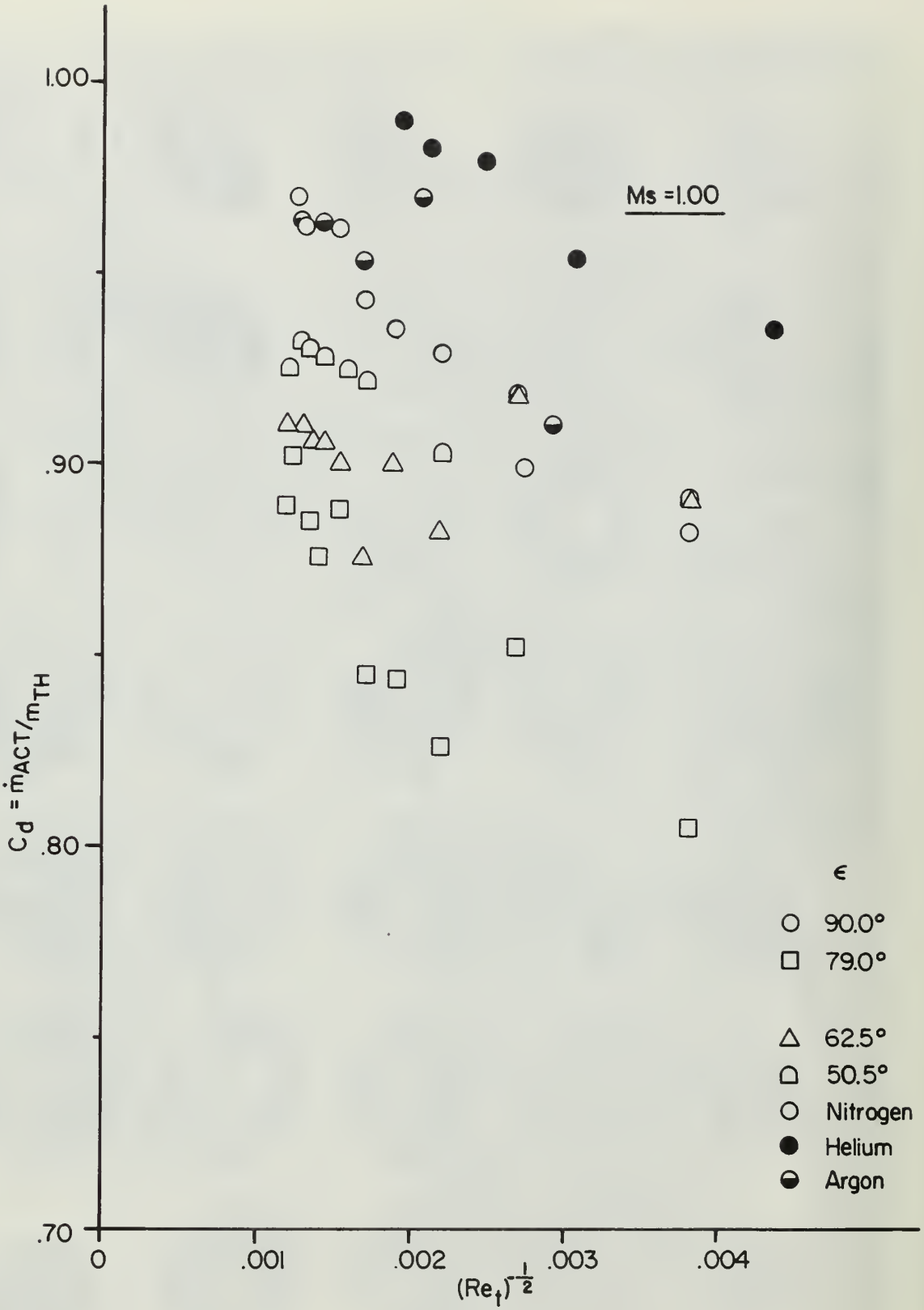

FIGURE 10

NOZZLE COEFFICIENT VS. INVERSE SQUARE ROOT OF Re_t

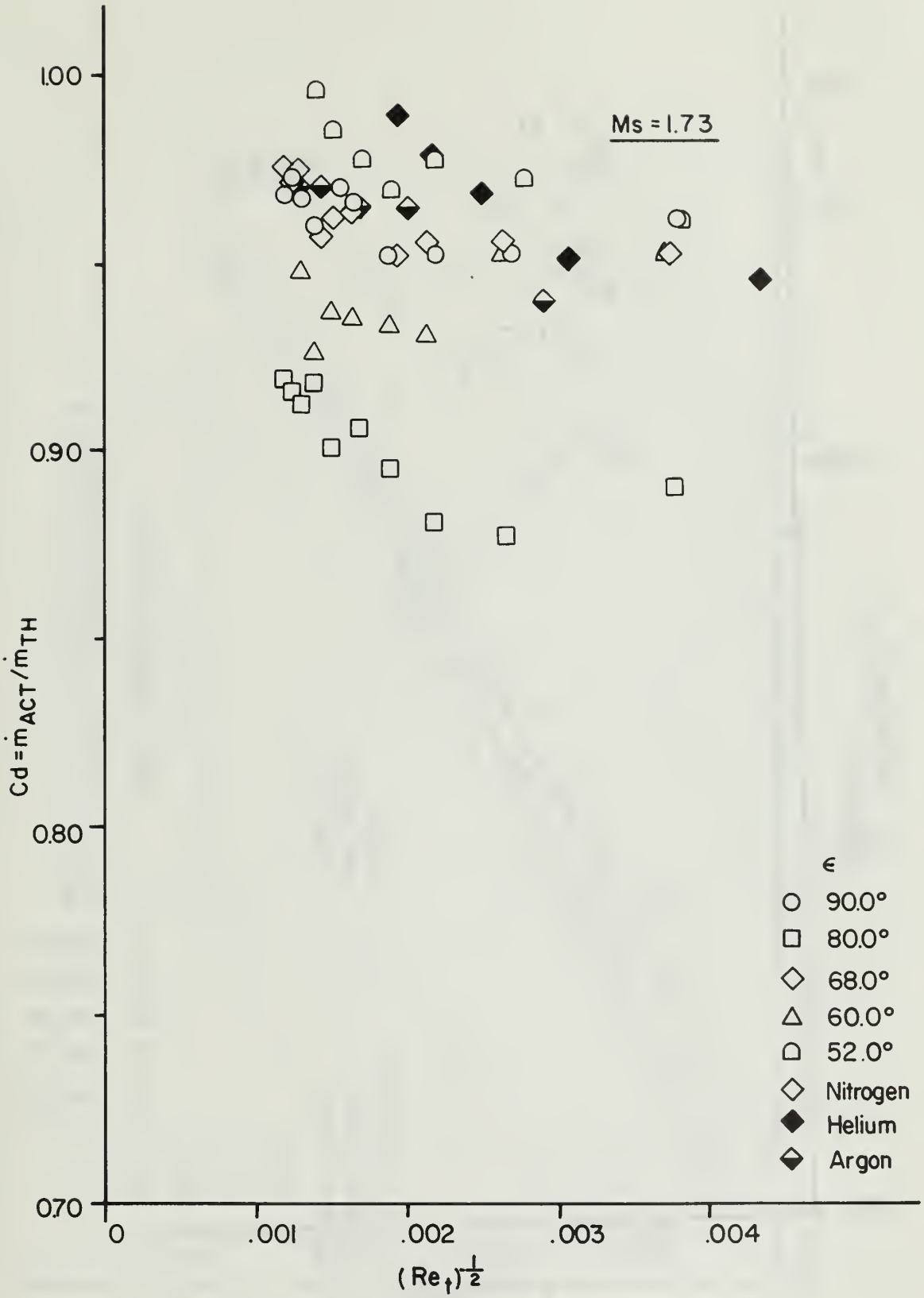

FIGURE 11

NOZZLE COEFFICIENT VS. INVERSE SQUARE ROOT OF Re_t

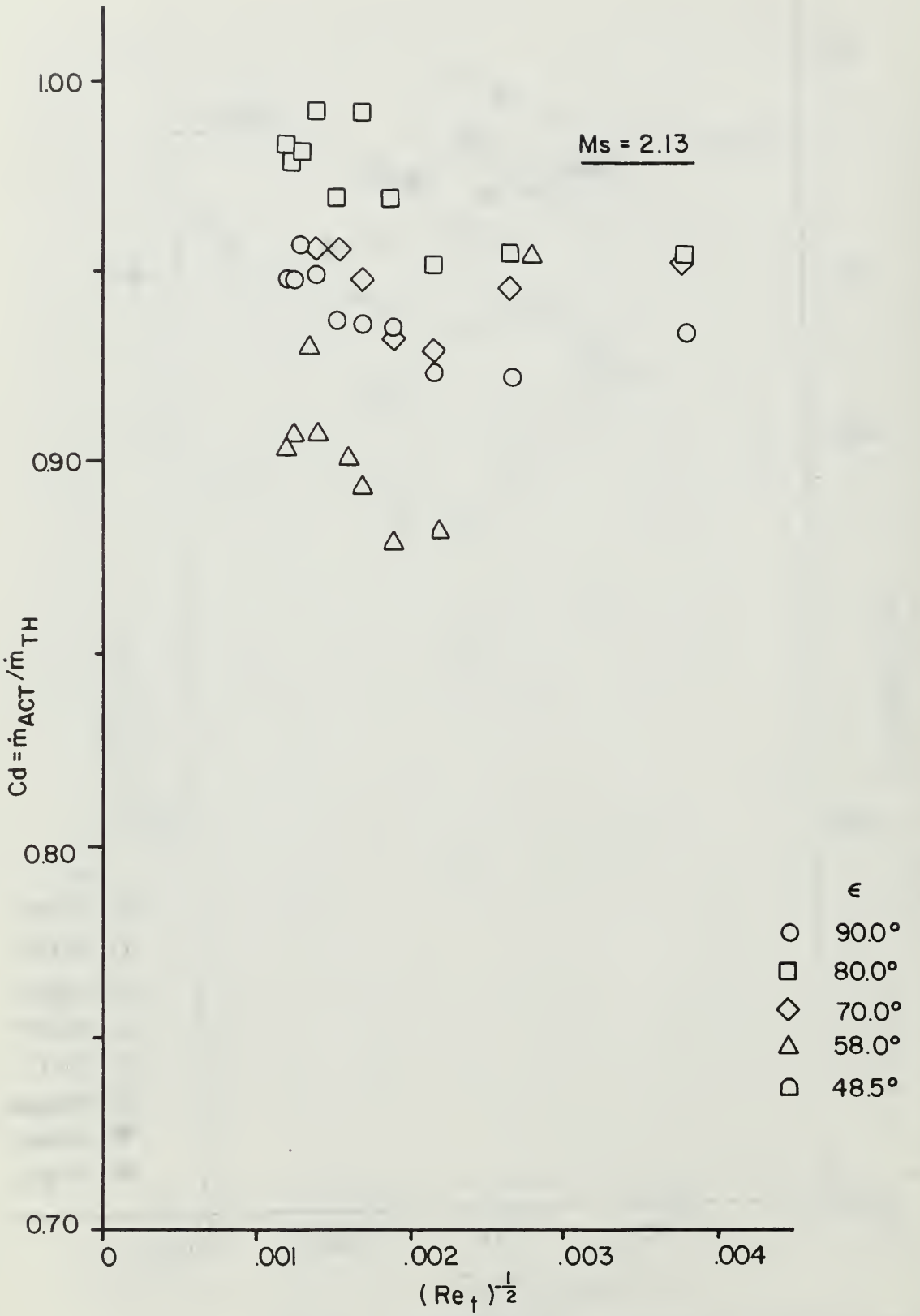

FIGURE 12

NOZZLE COEFFICIENT VS. INVERSE SQUARE ROOT OF Re_t

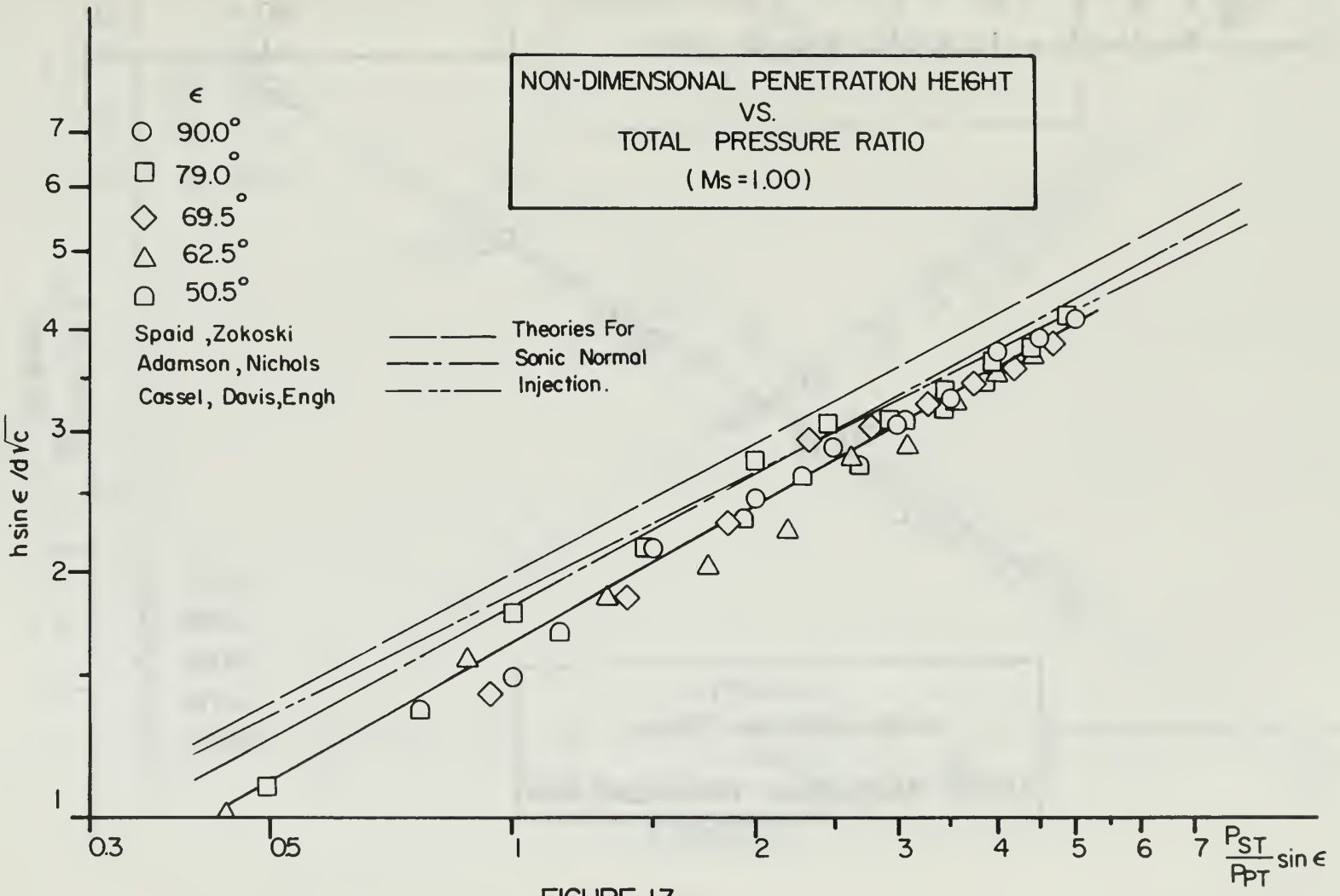
NON-DIMENSIONAL PENETRATION HEIGHT
VS.
TOTAL PRESSURE RATIO
(Ms = 1.00)
ϵ
90.0°
79.0°
69.5°
62.5°
50.5°
Spaid , Zokoski
Adamson , Nichols
Cassel, Davis, Engh
Theories For
Sonic Normal
Injection.
h sin ϵ /d√c
0.3
0.5
1
2
3
4
5
6
7
PST/PPT sin ϵ

FIGURE 13

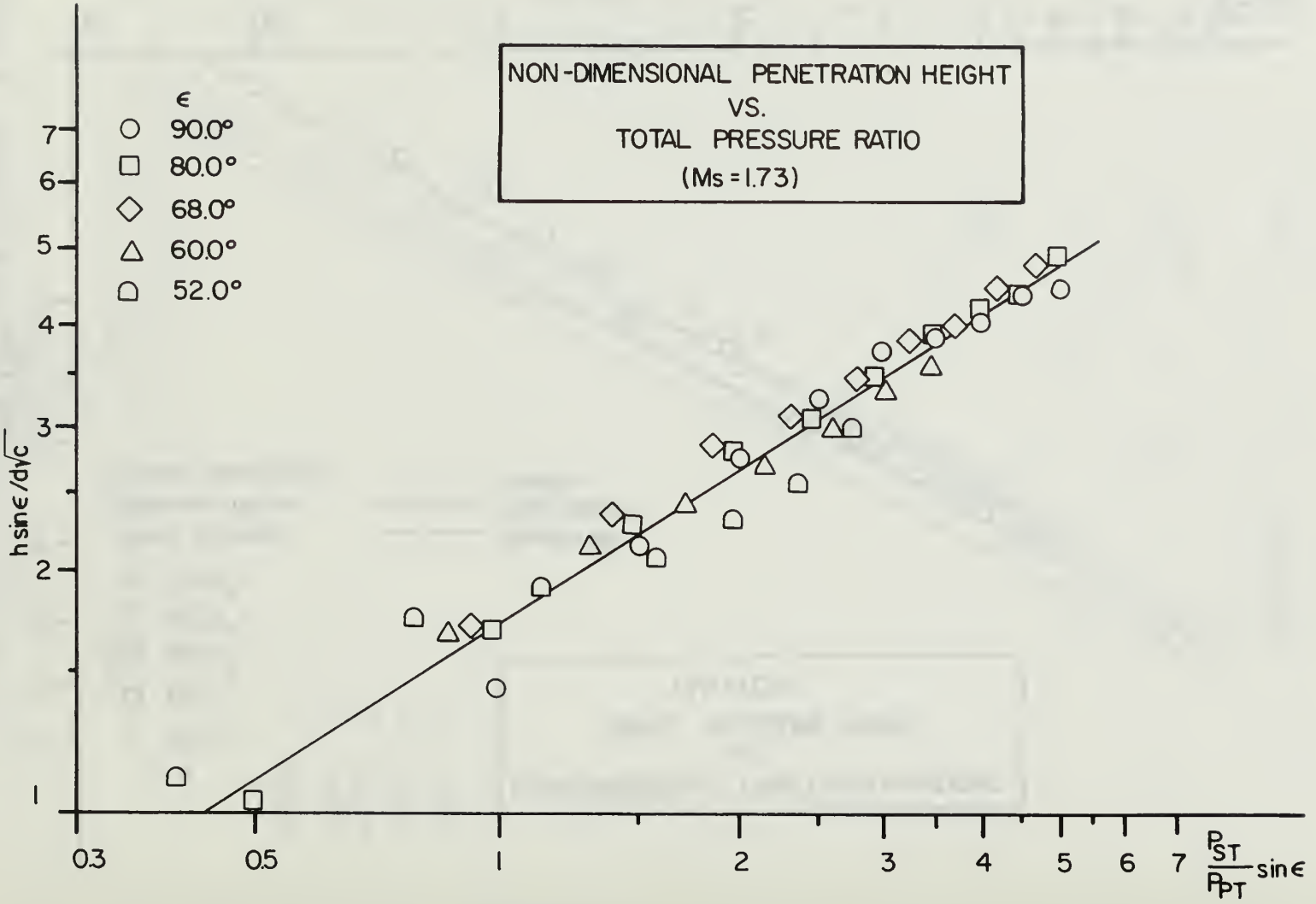
NON-DIMENSIONAL PENETRATION HEIGHT
VS.
TOTAL PRESSURE RATIO
(Ms = 1.73)
ϵ
90.0°
80.0°
68.0°
60.0°
52.0°
h sinϵ/d√c
1
2
3
4
5
6
7
0.3
0.5
1
2
3
4
5
6
7
$\frac{P_{ST}}{P_{PT}}$ sinϵ

FIGURE 14

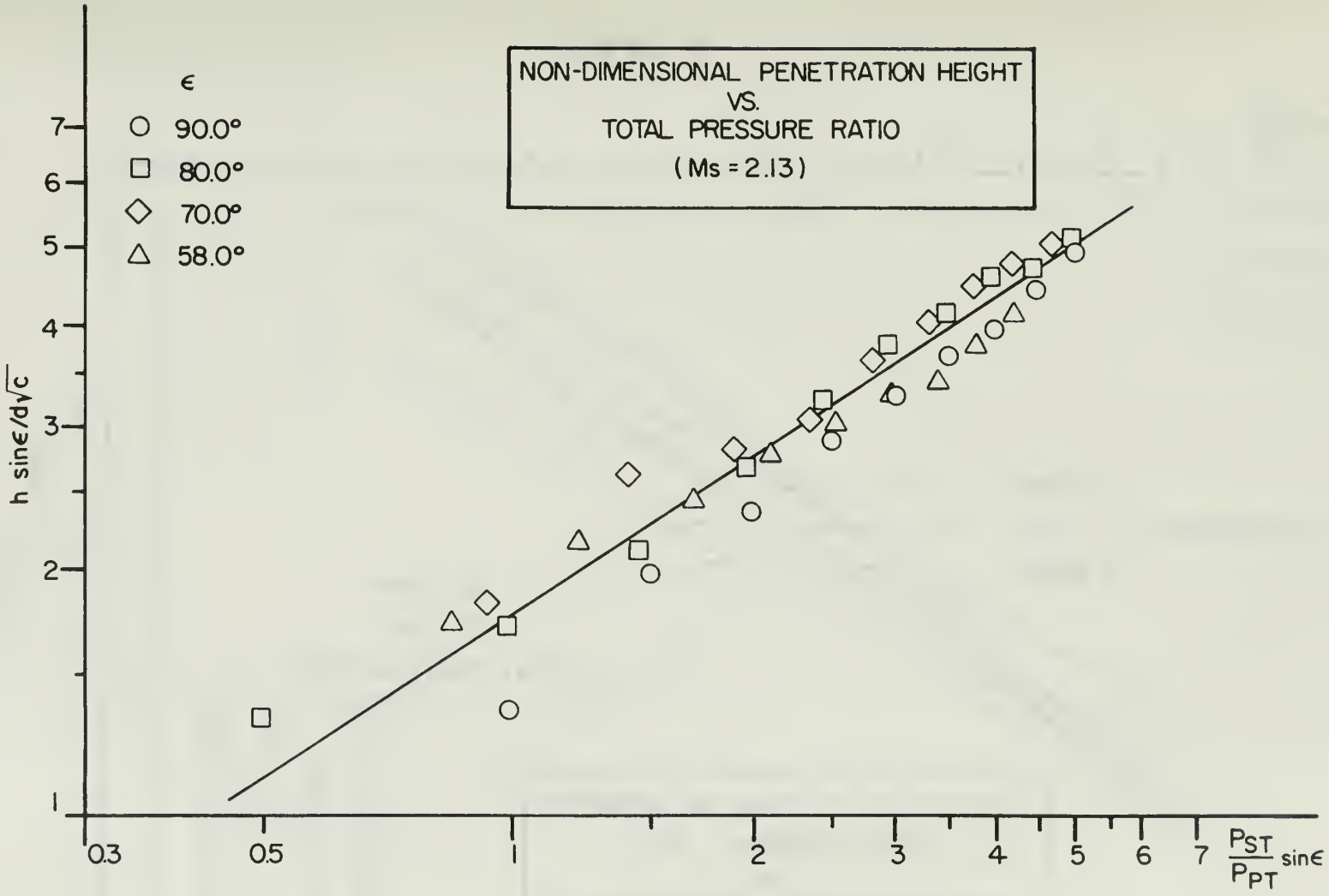
NON-DIMENSIONAL PENETRATION HEIGHT
VS.
TOTAL PRESSURE RATIO
(Ms = 2.13)
ϵ
90.0°
80.0°
70.0°
58.0°
h sinϵ/d√c
1
2
3
4
5
6
7
0.3
0.5
1
2
3
4
5
6
7
PST/PPT sinϵ

FIGURE 15

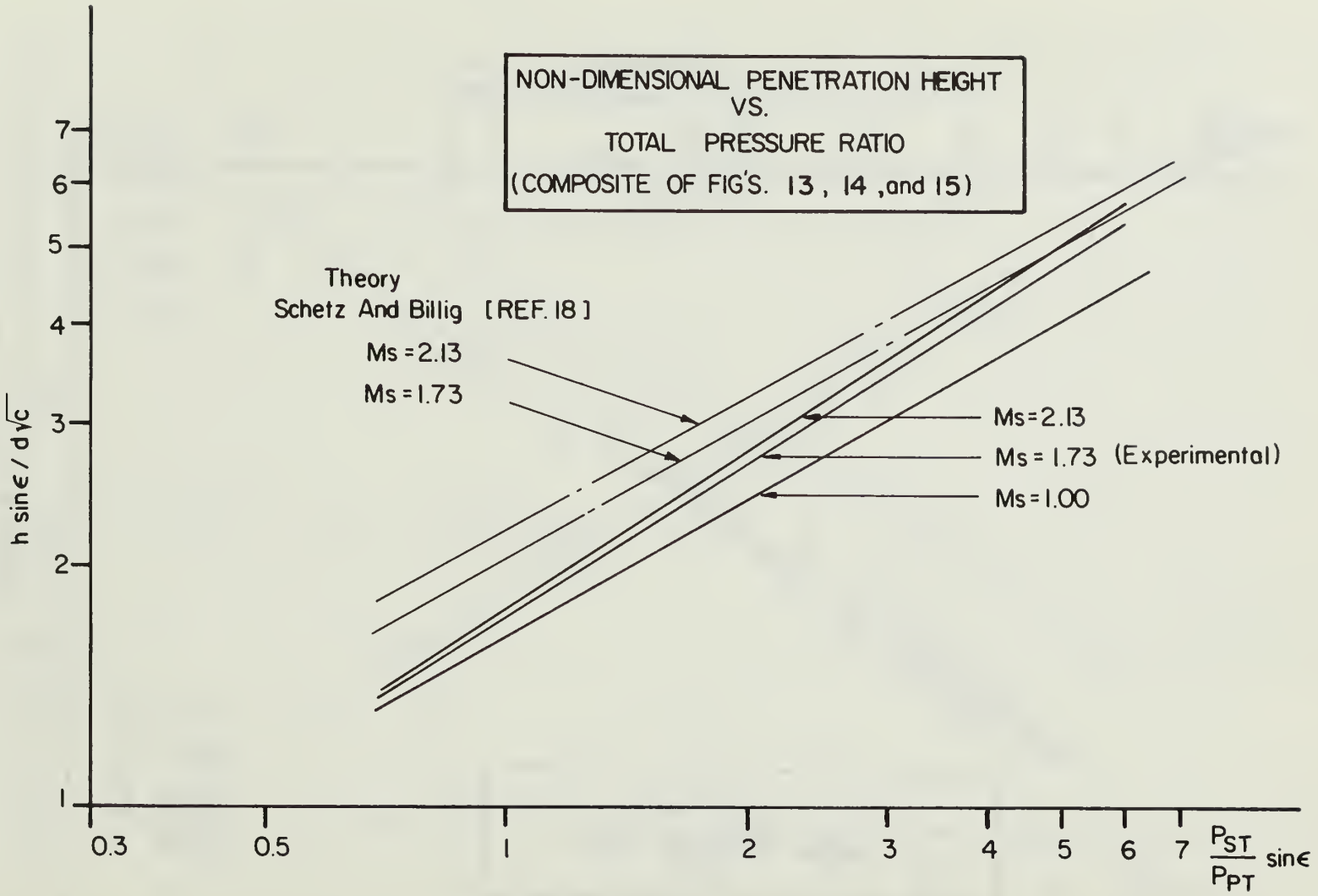
NON-DIMENSIONAL PENETRATION HEIGHT
VS.
TOTAL PRESSURE RATIO
(COMPOSITE OF FIG'S. 13, 14, and 15)
Theory
Schetz And Billig [REF. 18]
Ms = 2.13
Ms = 1.73
Ms = 2.13
Ms = 1.73 (Experimental)
Ms = 1.00
h sinϵ / d√c
1
2
3
4
5
6
7
0.3
0.5
1
2
3
4
5
6
7
$\frac{P_{ST}}{P_{PT}}$ sinϵ

FIGURE 16

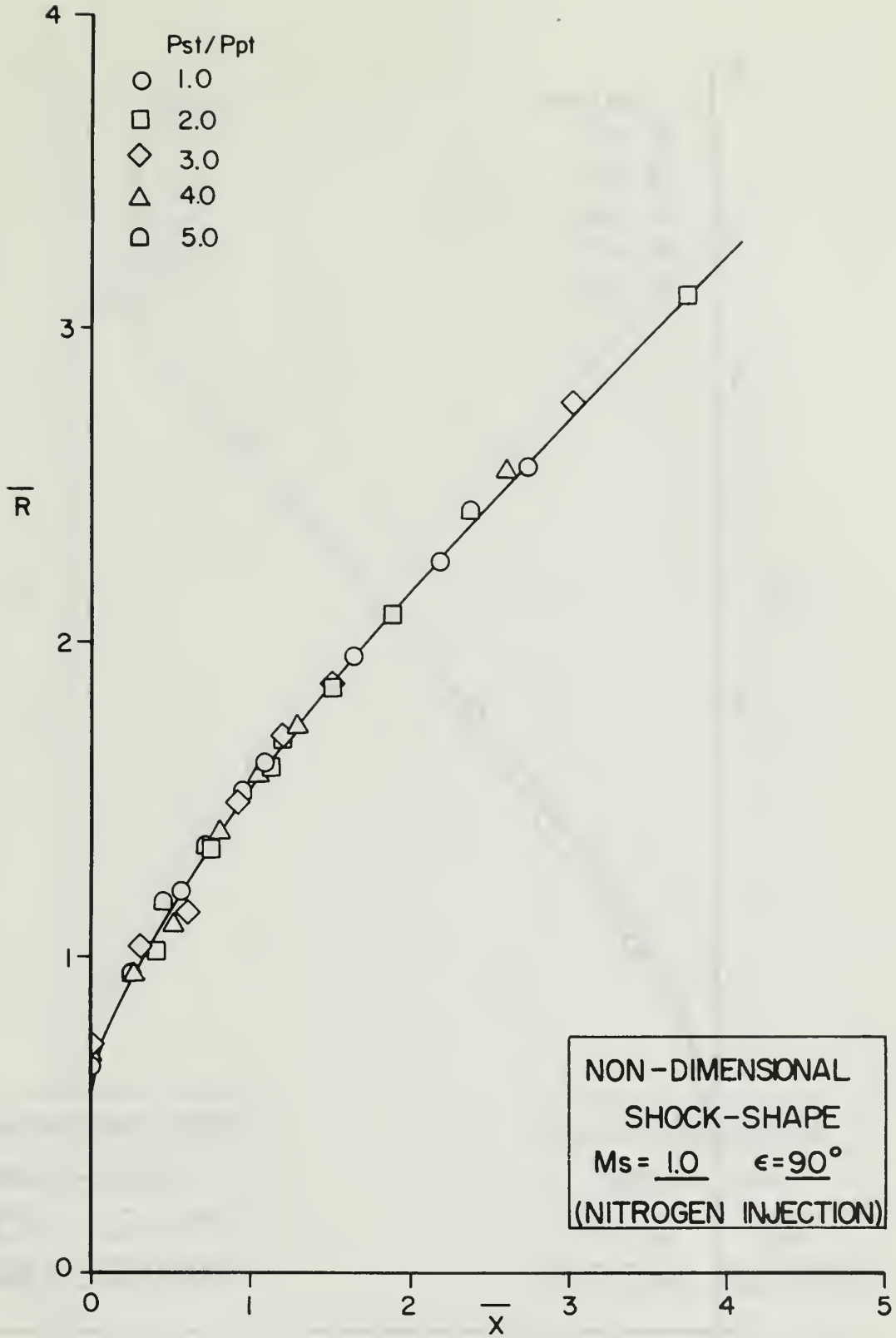
Pst/Ppt
1.0
2.0
3.0
4.0
5.0
$\overline{R}$
$\overline{X}$
0
1
2
3
4
5
NON-DIMENSIONAL
SHOCK-SHAPE
Ms = 1.0 ε = 90°
(NITROGEN INJECTION)

FIGURE 17

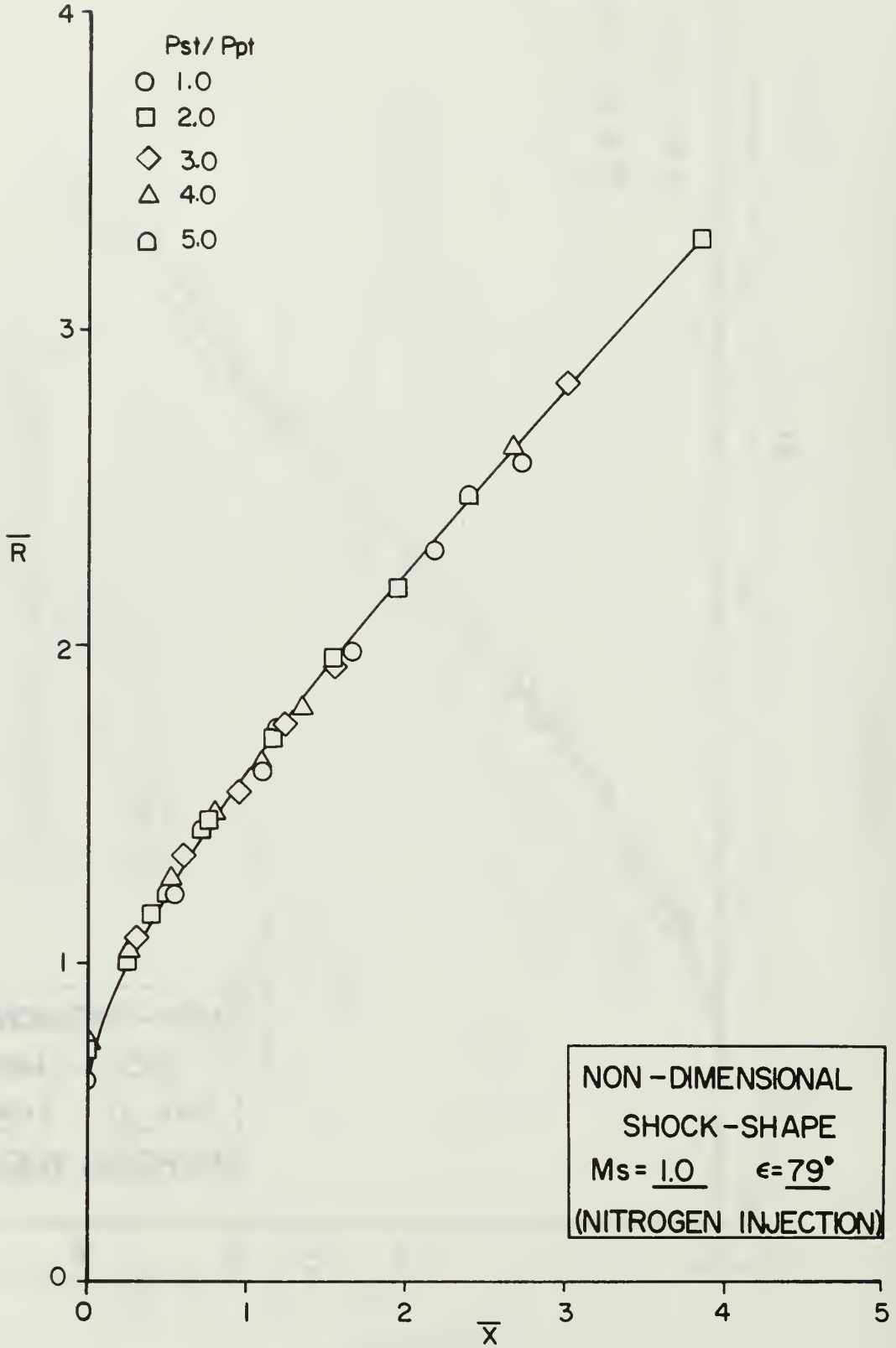
Pst/ Ppt
1.0
2.0
3.0
4.0
5.0
$\overline{R}$
$\overline{X}$
0
1
2
3
4
5
NON-DIMENSIONAL
SHOCK-SHAPE
Ms = 1.0 ε = 79°
(NITROGEN INJECTION)

FIGURE 18

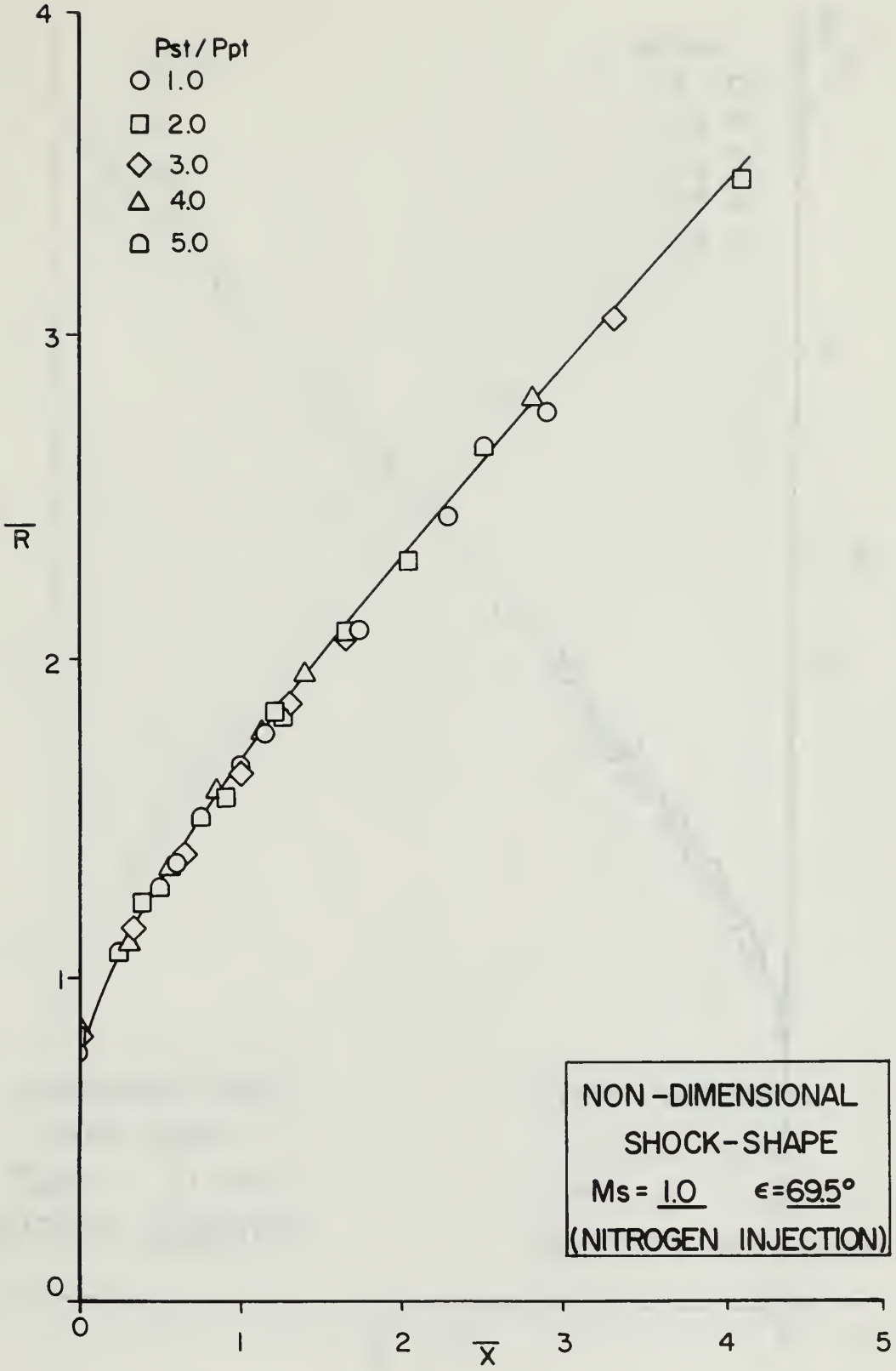
Pst / Ppt
1.0
2.0
3.0
4.0
5.0
$\overline{R}$
$\overline{X}$
0
1
2
3
4
5
NON-DIMENSIONAL
SHOCK-SHAPE
Ms = 1.0 ϵ=69.5°
(NITROGEN INJECTION)

FIGURE 19

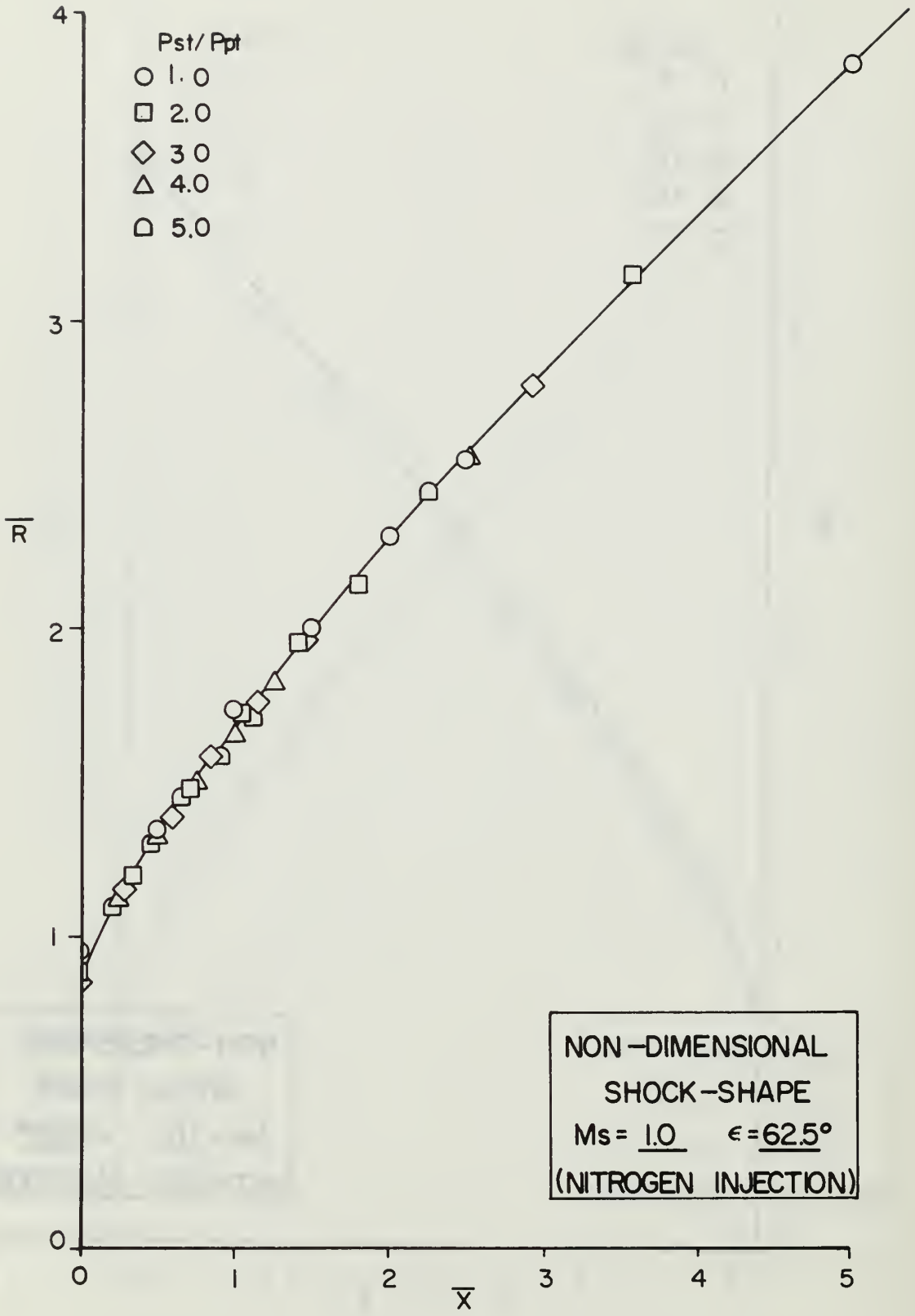
Pst/ Ppt
1.0
2.0
3.0
4.0
5.0
$\overline{R}$
$\overline{X}$
0
1
2
3
4
5
NON-DIMENSIONAL
SHOCK-SHAPE
Ms = 1.0 ∈ = 62.5°
(NITROGEN INJECTION)

FIGURE 20

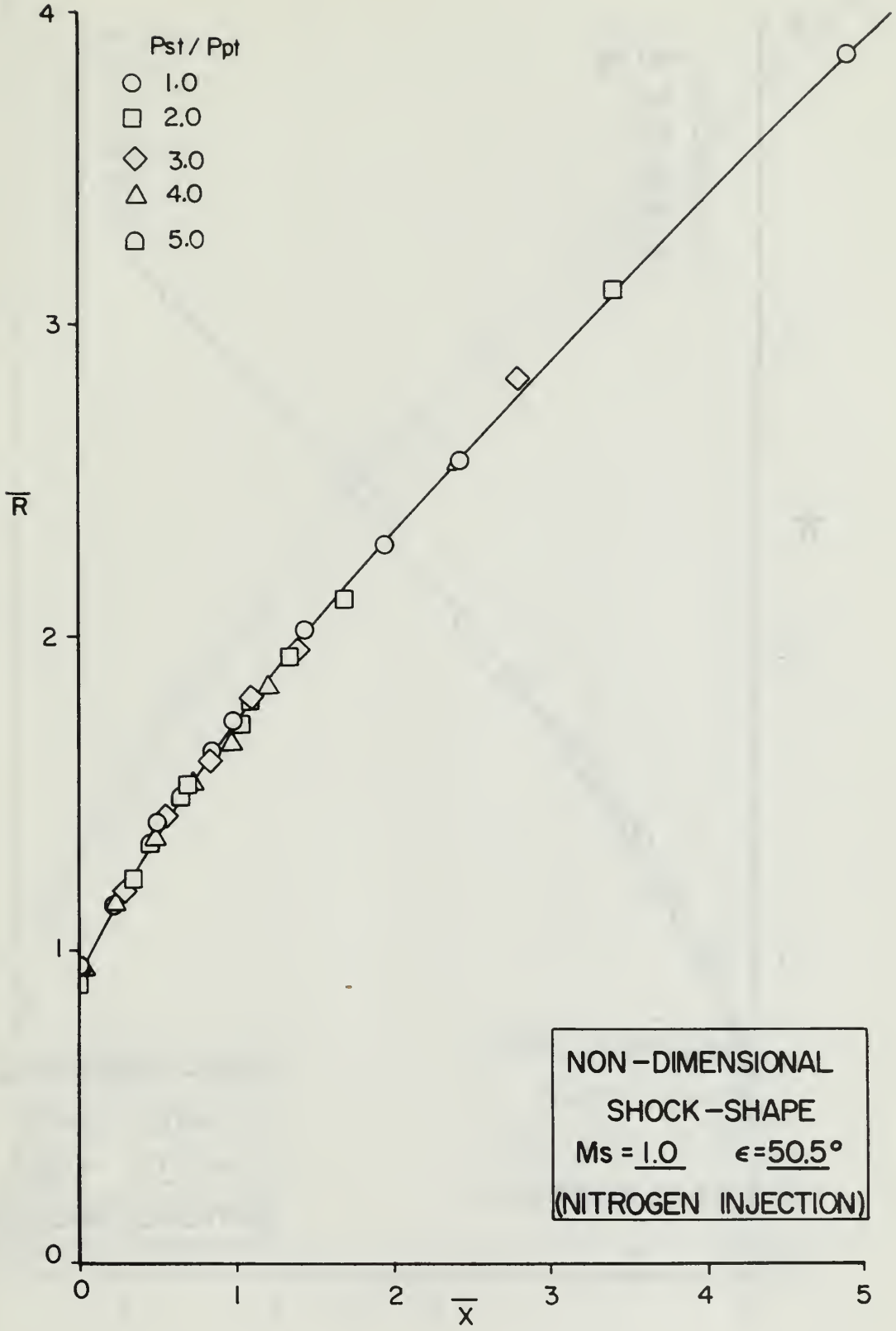
Pst / Ppt
1.0
2.0
3.0
4.0
5.0
NON-DIMENSIONAL
SHOCK-SHAPE
Ms = 1.0 ϵ=50.5°
(NITROGEN INJECTION)
R̄
X̄
0
1
2
3
4
5

FIGURE 21

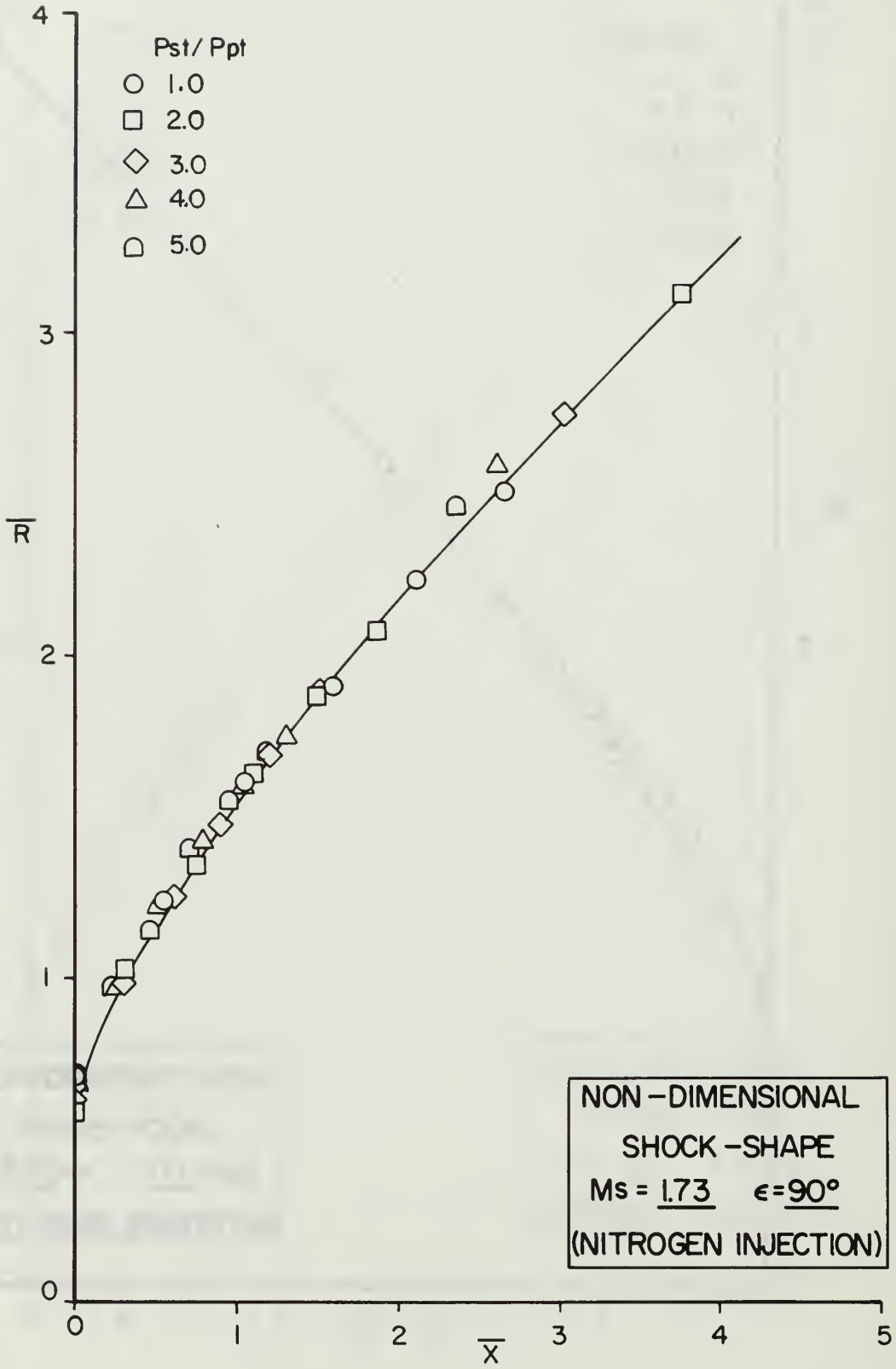
Pst/ Ppt
1.0
2.0
3.0
4.0
5.0
$\overline{R}$
$\overline{X}$
0
1
2
3
4
5
NON-DIMENSIONAL
SHOCK-SHAPE
Ms = 1.73 ε=90°
(NITROGEN INJECTION)

FIGURE 22

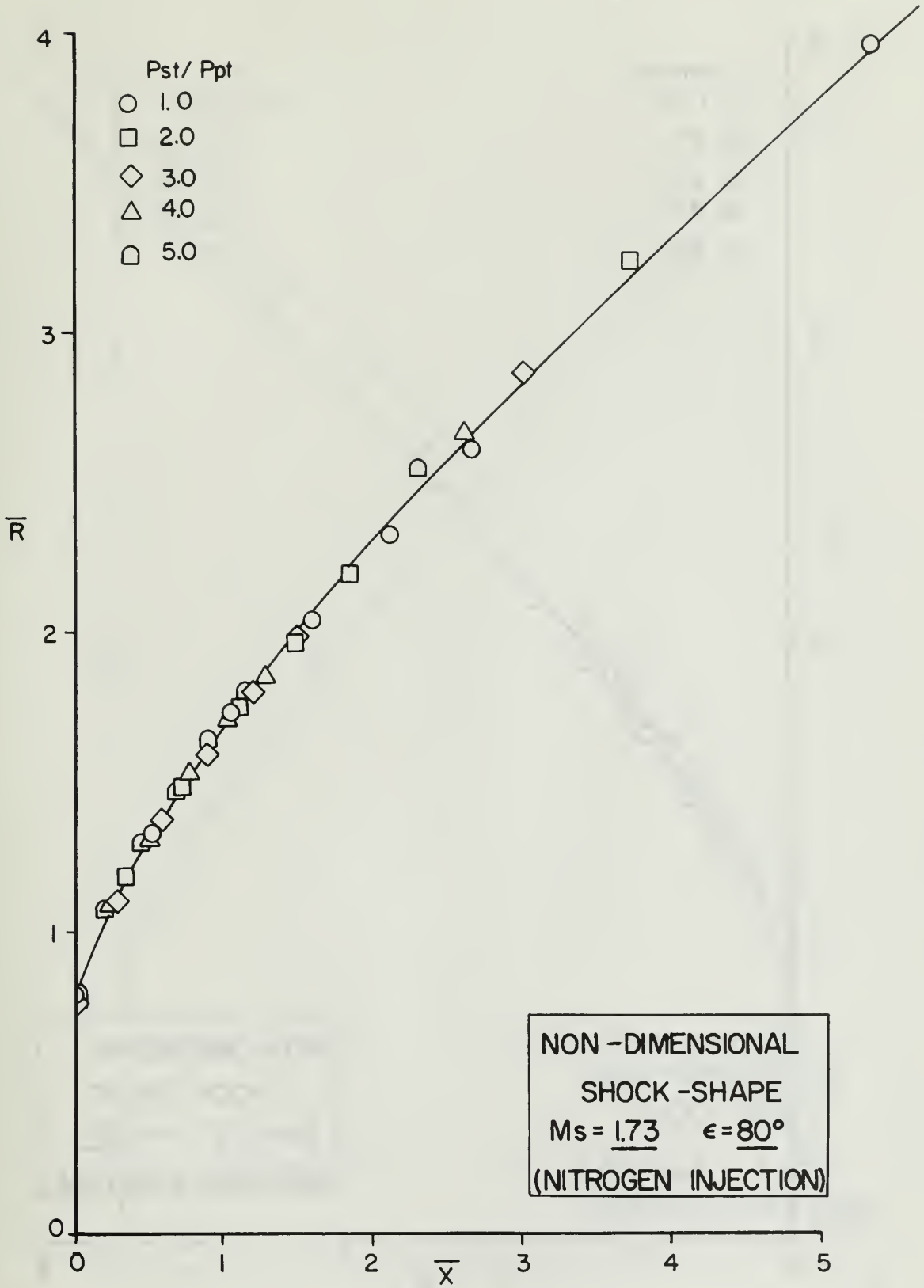
Pst/ Ppt
1.0
2.0
3.0
4.0
5.0
$\overline{R}$
$\overline{X}$
0
1
2
3
4
5
NON-DIMENSIONAL
SHOCK-SHAPE
Ms = 1.73 ε = 80°
(NITROGEN INJECTION)

FIGURE 23

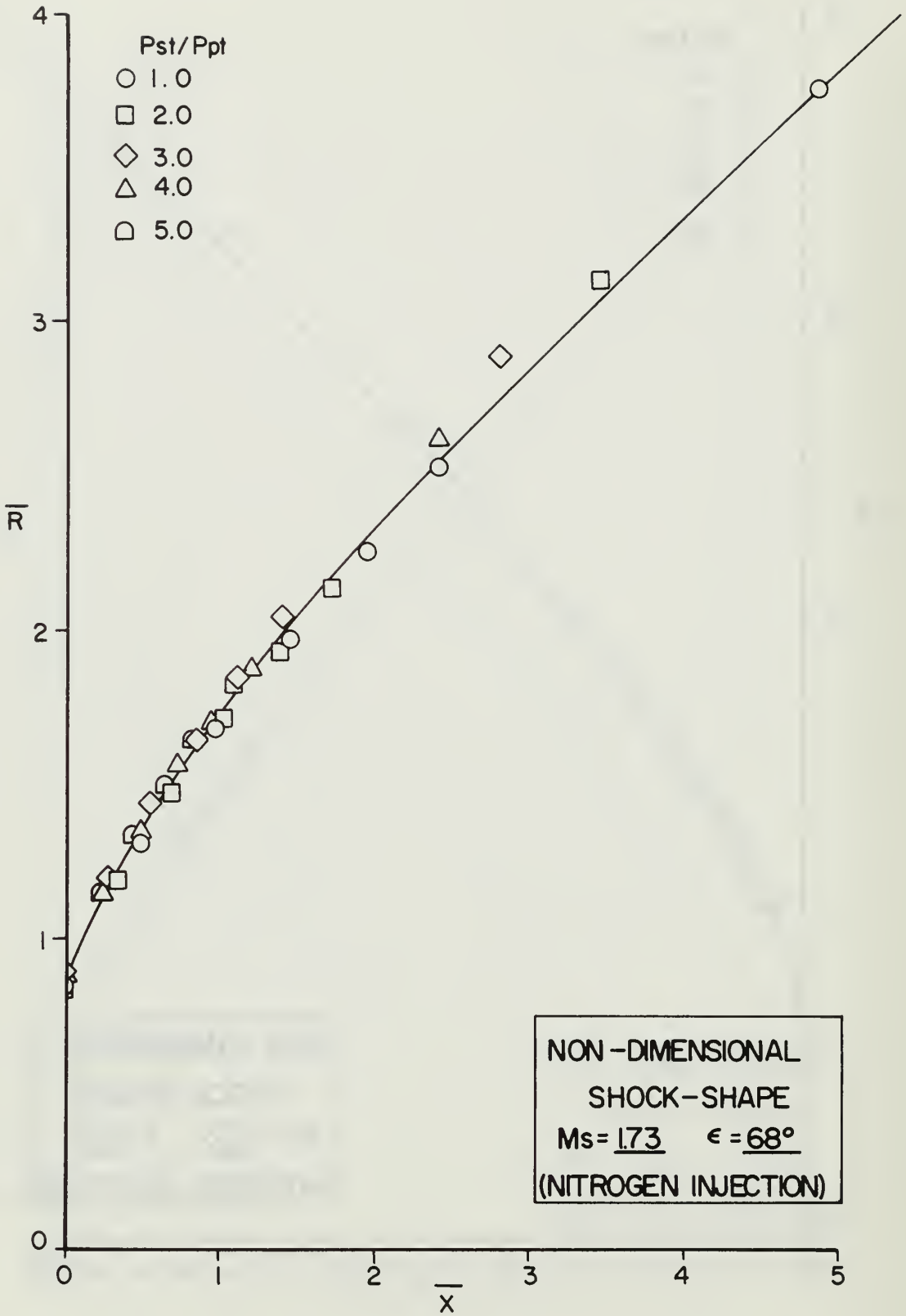
Pst/Ppt
1.0
2.0
3.0
4.0
5.0
$\overline{R}$
$\overline{X}$
0
1
2
3
4
5
NON-DIMENSIONAL
SHOCK-SHAPE
Ms= 1.73 ε = 68°
(NITROGEN INJECTION)

FIGURE 24

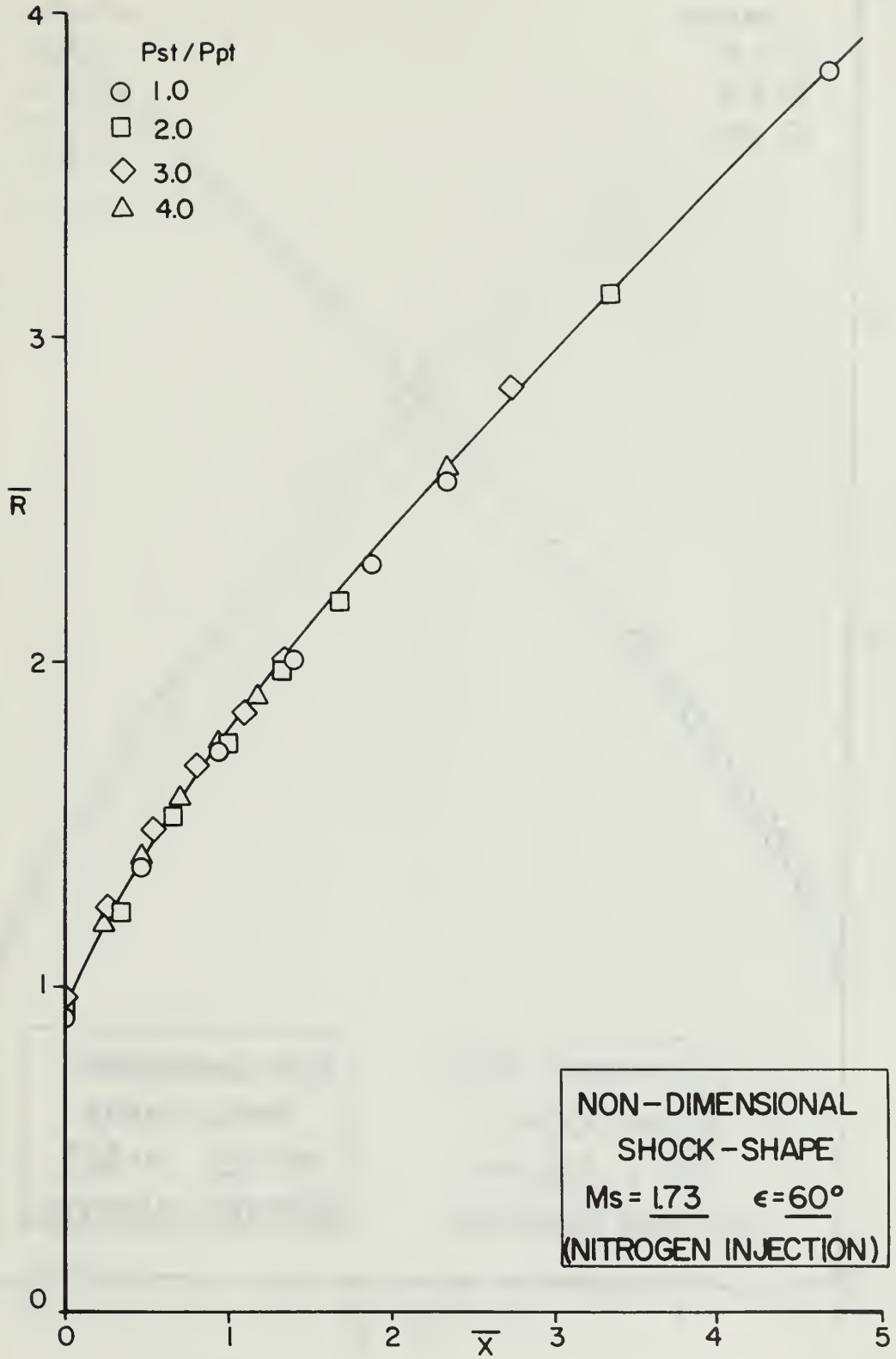
Pst / Ppt
1.0
2.0
3.0
4.0
$\overline{R}$
$\overline{X}$
0
1
2
3
4
5
NON-DIMENSIONAL
SHOCK-SHAPE
Ms = 1.73 ε = 60°
(NITROGEN INJECTION)

FIGURE 25

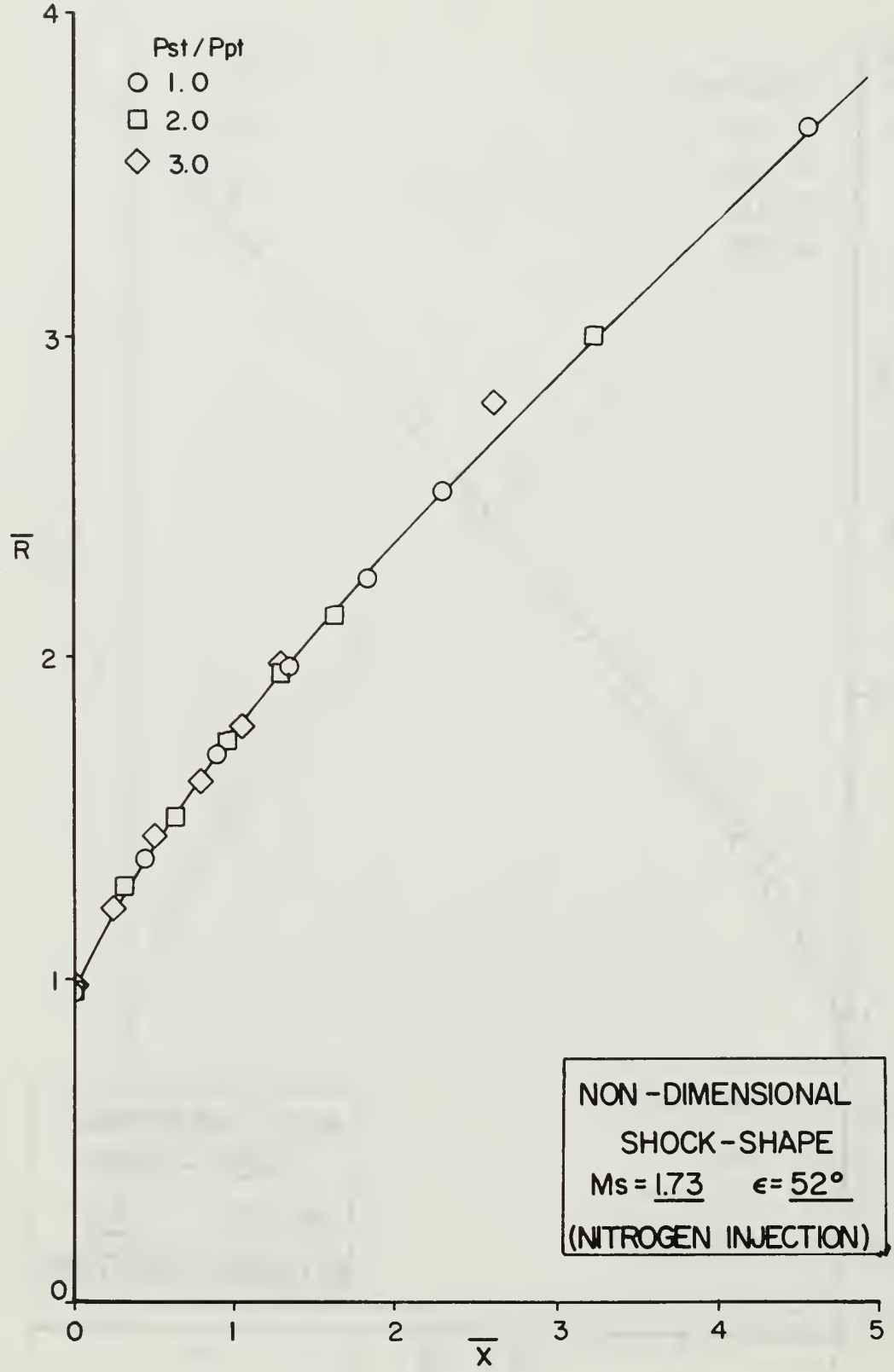
Pst / Ppt
1.0
2.0
3.0
$\overline{R}$
$\overline{X}$
0
1
2
3
4
5
NON-DIMENSIONAL
SHOCK-SHAPE
Ms = 1.73 ε = 52°
(NITROGEN INJECTION)

FIGURE 26

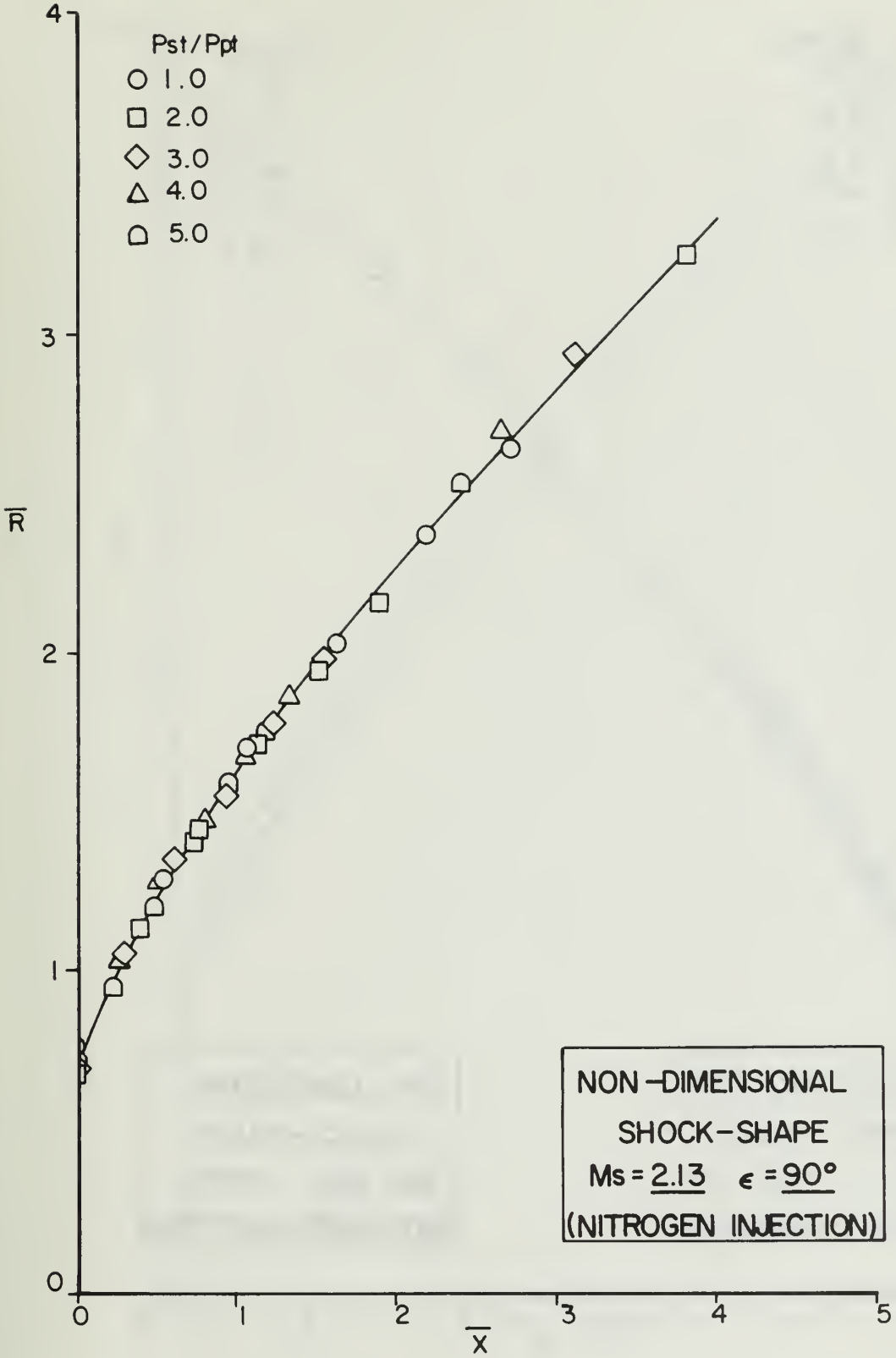
Pst/Ppt
1.0
2.0
3.0
4.0
5.0
R̄
X̄
0
1
2
3
4
5
NON-DIMENSIONAL
SHOCK-SHAPE
Ms = 2.13 ε = 90°
(NITROGEN INJECTION)

FIGURE 27

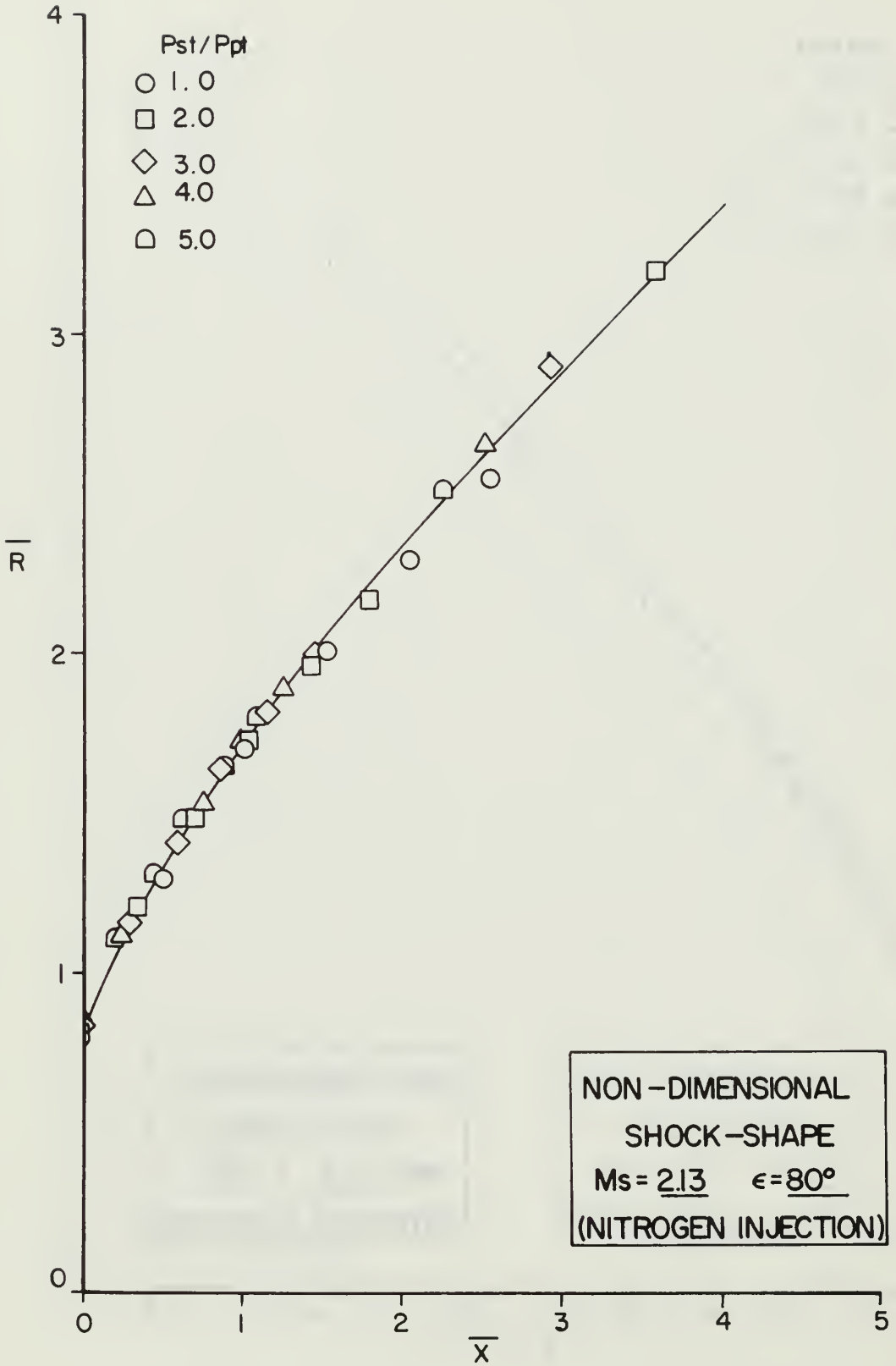
Pst/Ppt
1.0
2.0
3.0
4.0
5.0
$\overline{R}$
$\overline{X}$
0
1
2
3
4
5
NON-DIMENSIONAL
SHOCK-SHAPE
Ms = 2.13 ε = 80°
(NITROGEN INJECTION)

FIGURE 28

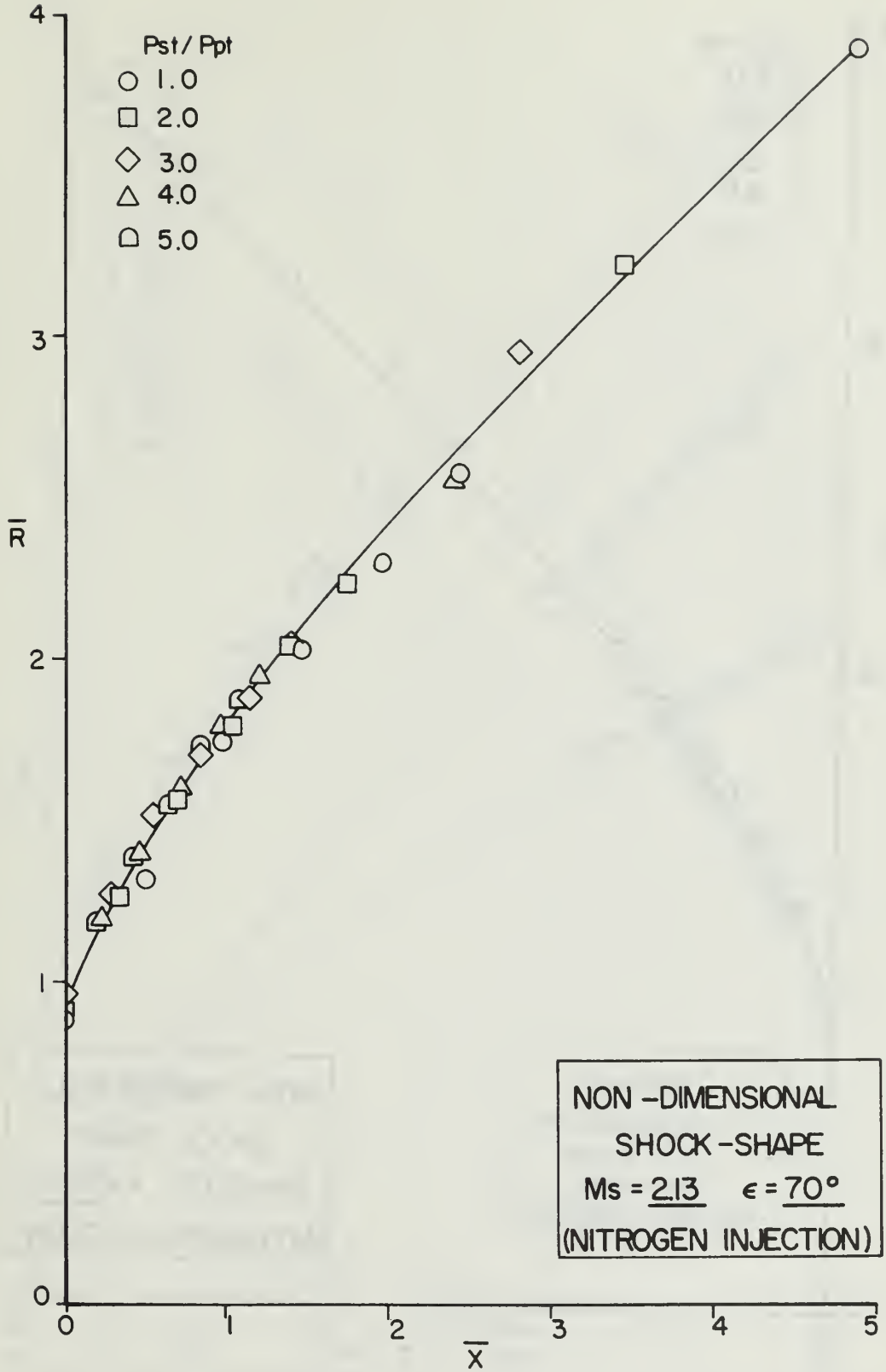
Pst / Ppt
1.0
2.0
3.0
4.0
5.0
$\bar{R}$
$\bar{X}$
0
1
2
3
4
5
NON-DIMENSIONAL
SHOCK-SHAPE
Ms = 2.13 ε = 70°
(NITROGEN INJECTION)

FIGURE 29

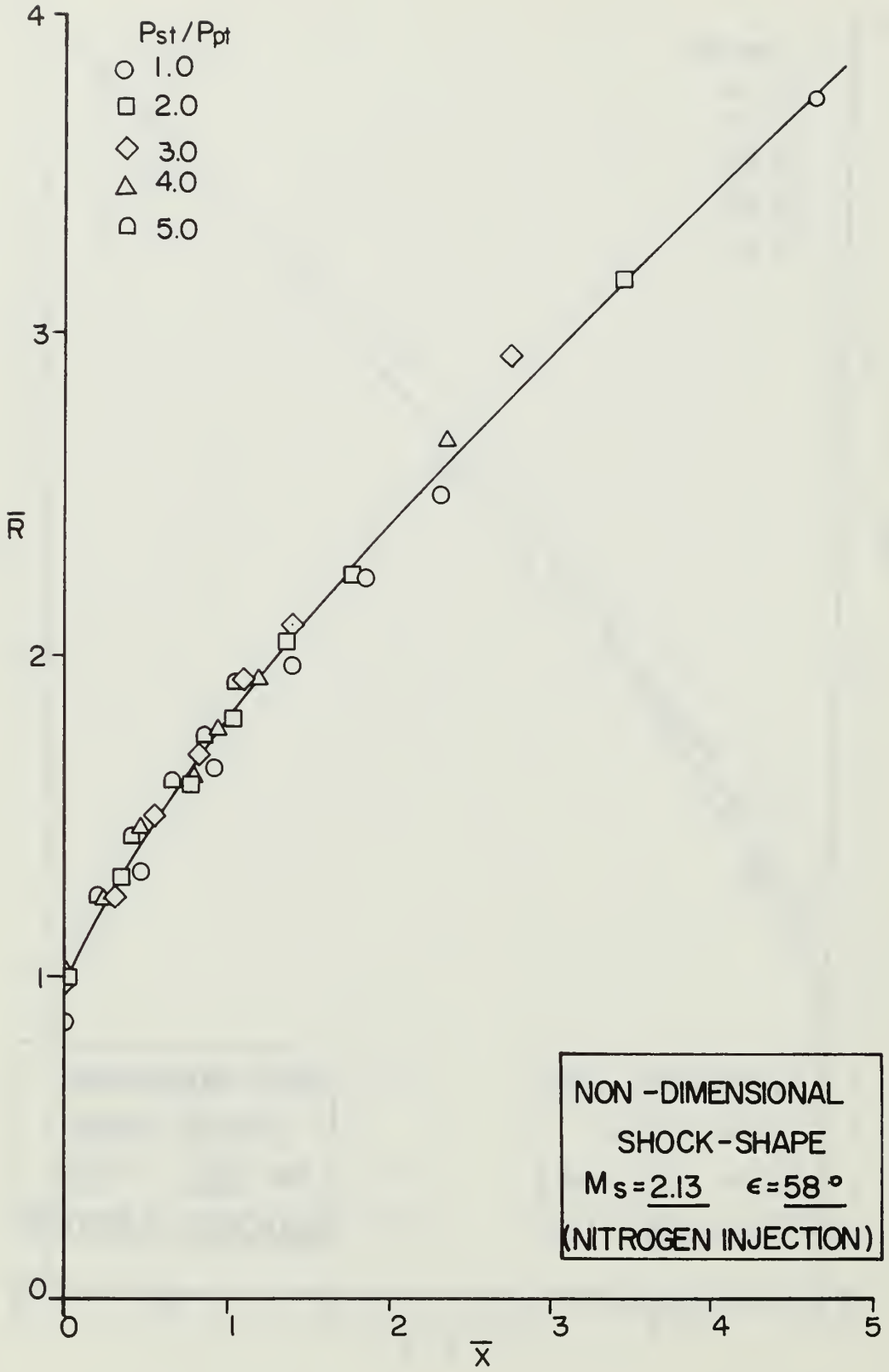
Pst / Ppt
1.0
2.0
3.0
4.0
5.0
R̄
X̄
0
1
2
3
4
5
NON-DIMENSIONAL
SHOCK-SHAPE
Ms = 2.13 ϵ = 58°
(NITROGEN INJECTION)

FIGURE 30

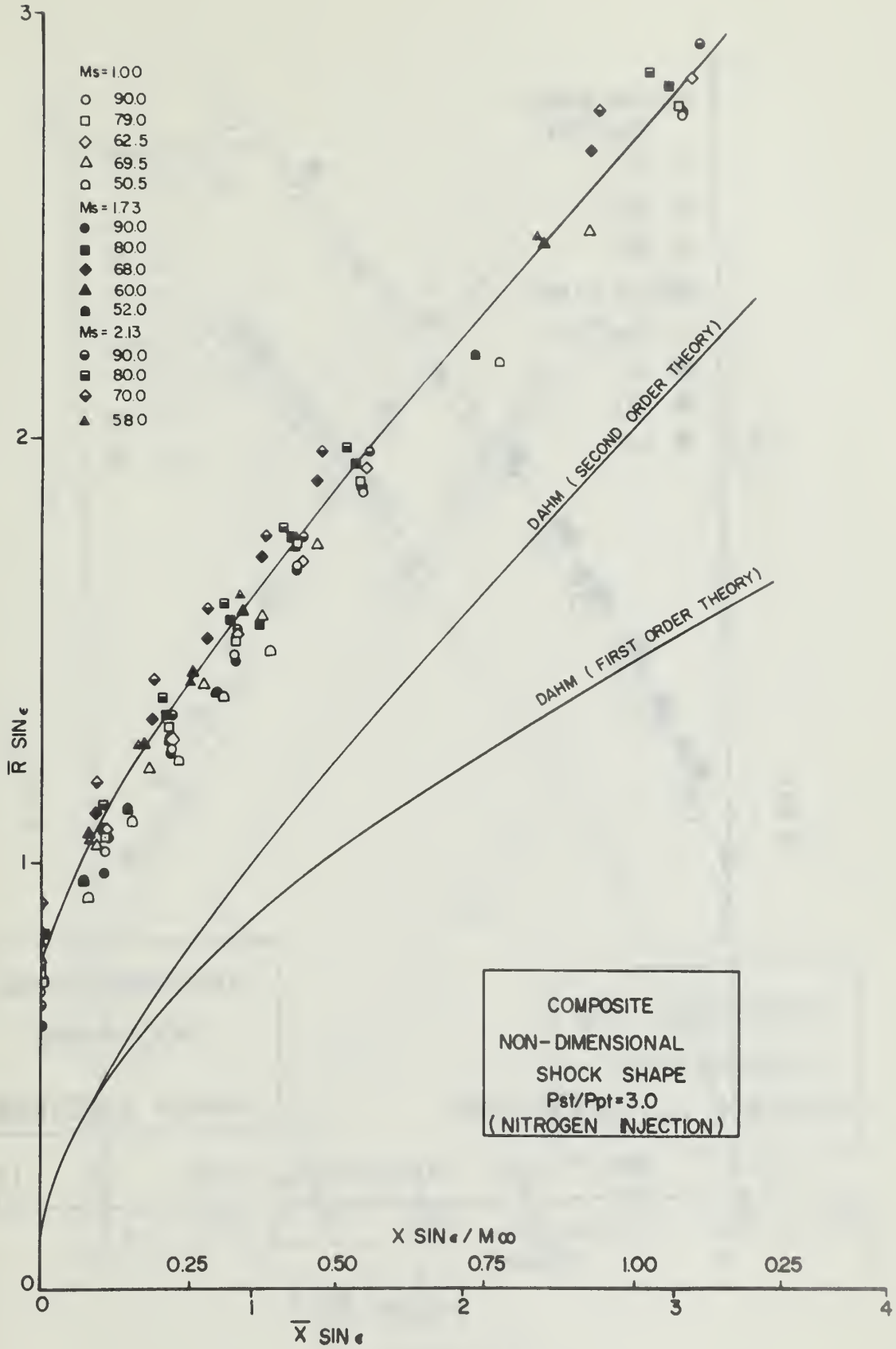
Ms = 1.00
90.0
79.0
62.5
69.5
50.5
Ms = 1.73
90.0
80.0
68.0
60.0
52.0
Ms = 2.13
90.0
80.0
70.0
58.0
DAHM (SECOND ORDER THEORY)
DAHM (FIRST ORDER THEORY)
COMPOSITE
NON-DIMENSIONAL
SHOCK SHAPE
Pst/Ppt = 3.0
(NITROGEN INJECTION)
R̄ SIN ε
X̄ SIN ε
X SIN ε / M∞
0.25
0.50
0.75
1.00
0.25
0
1
2
3
4

FIGURE 31

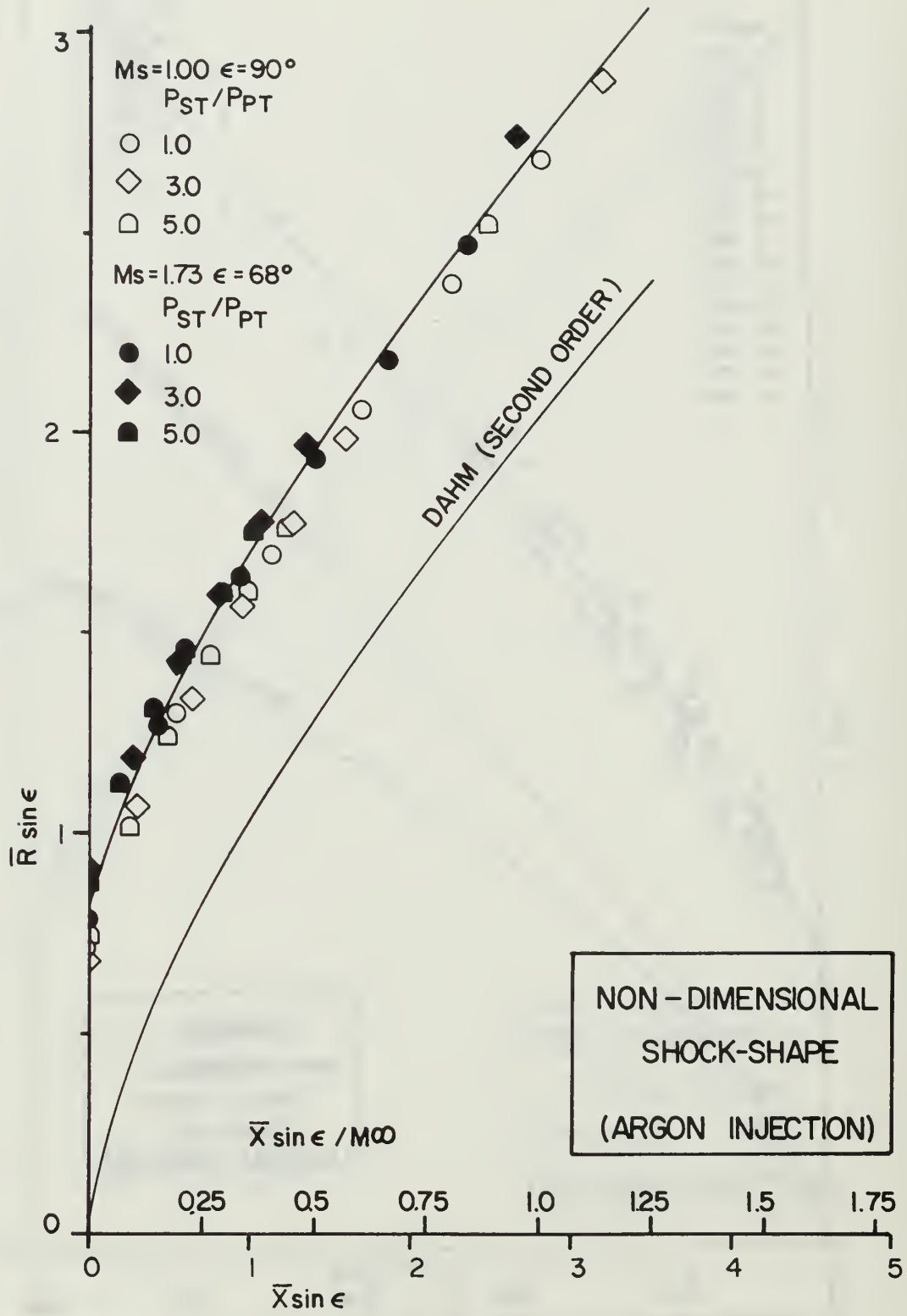
Ms=1.00 ϵ=90°
PST/PPT
1.0
3.0
5.0
Ms=1.73 ϵ=68°
PST/PPT
1.0
3.0
5.0
DAHM (SECOND ORDER)
NON – DIMENSIONAL
SHOCK-SHAPE
(ARGON INJECTION)
R̄ sin ϵ
X̄ sin ϵ / M∞
X̄ sin ϵ
0
1
2
3
0.25
0.5
0.75
1.0
1.25
1.5
1.75
4
5

FIGURE 32

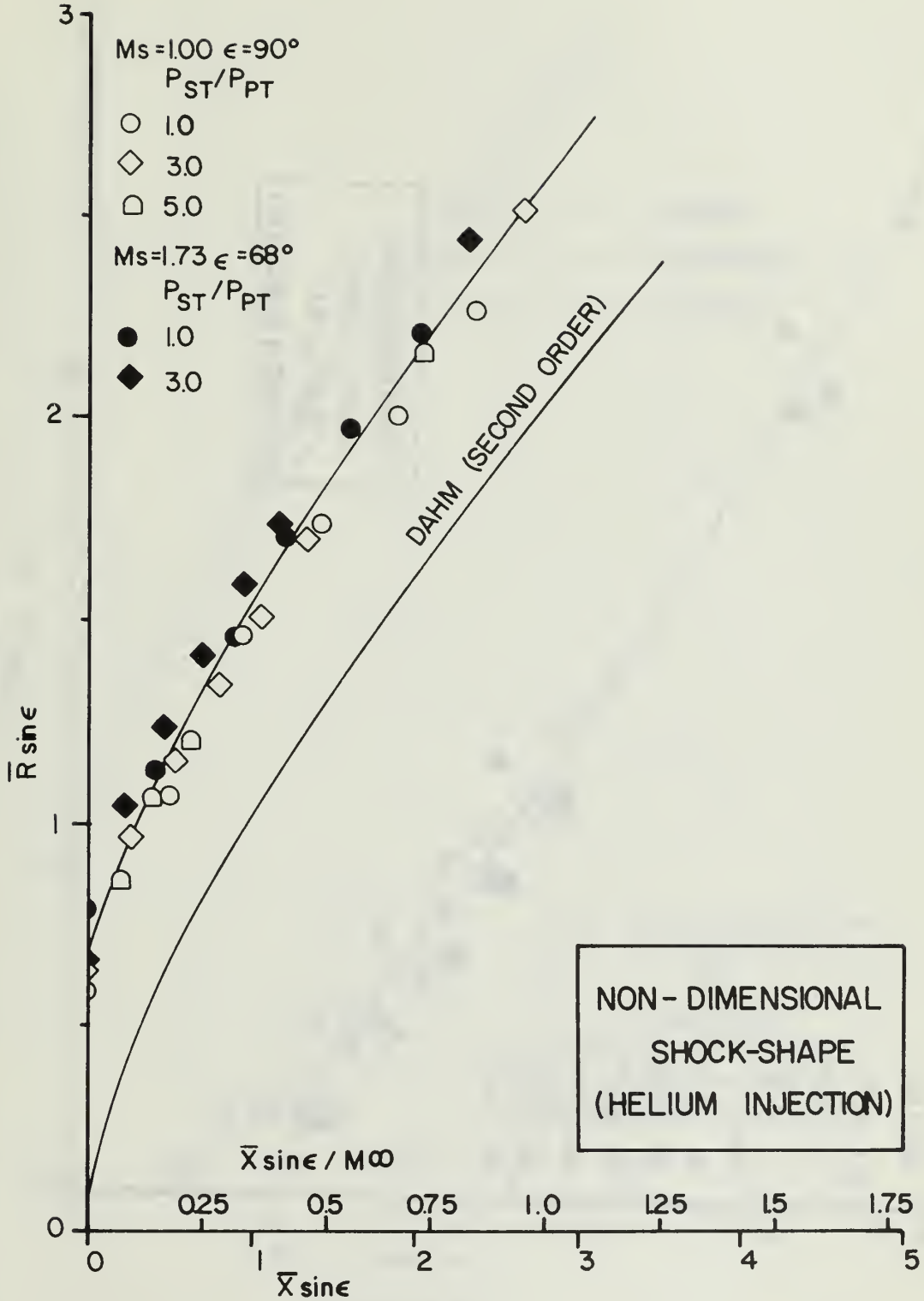
Ms = 1.00 ϵ = 90°
P_{ST}/P_{PT}
1.0
3.0
5.0
Ms = 1.73 ϵ = 68°
P_{ST}/P_{PT}
1.0
3.0
DAHM (SECOND ORDER)
NON - DIMENSIONAL
SHOCK-SHAPE
(HELIUM INJECTION)
$\bar{R}\sin\epsilon$
$\bar{X}\sin\epsilon / M\infty$
$\bar{X}\sin\epsilon$
0
0.25
0.5
0.75
1.0
1.25
1.5
1.75
1
2
3
4
5

FIGURE 33

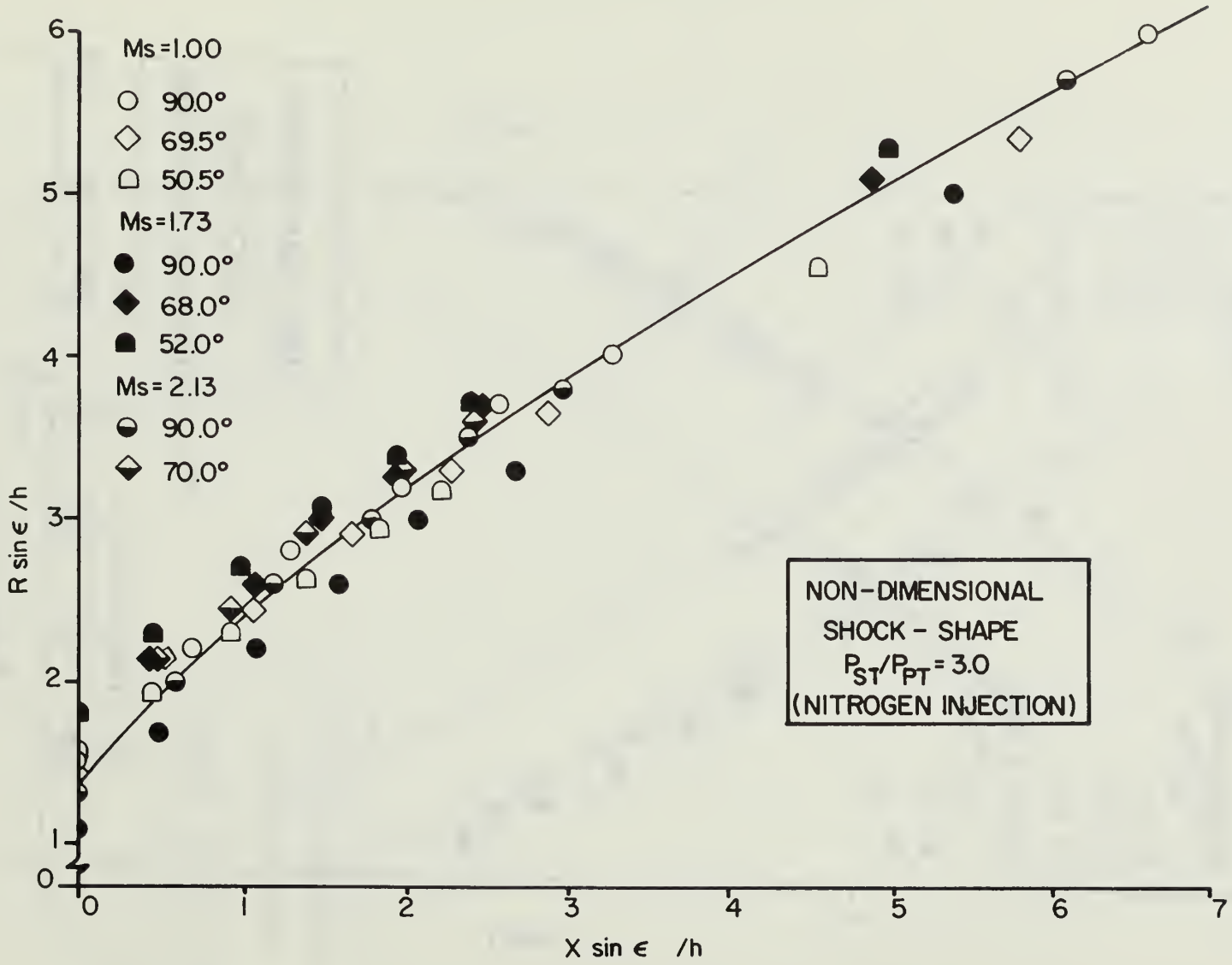
Ms = 1.00
90.0°
69.5°
50.5°
Ms = 1.73
90.0°
68.0°
52.0°
Ms = 2.13
90.0°
70.0°
NON-DIMENSIONAL
SHOCK - SHAPE
P_{ST}/P_{PT} = 3.0
(NITROGEN INJECTION)
R sin ϵ /h
X sin ϵ /h
0
1
2
3
4
5
6
7

FIGURE 34

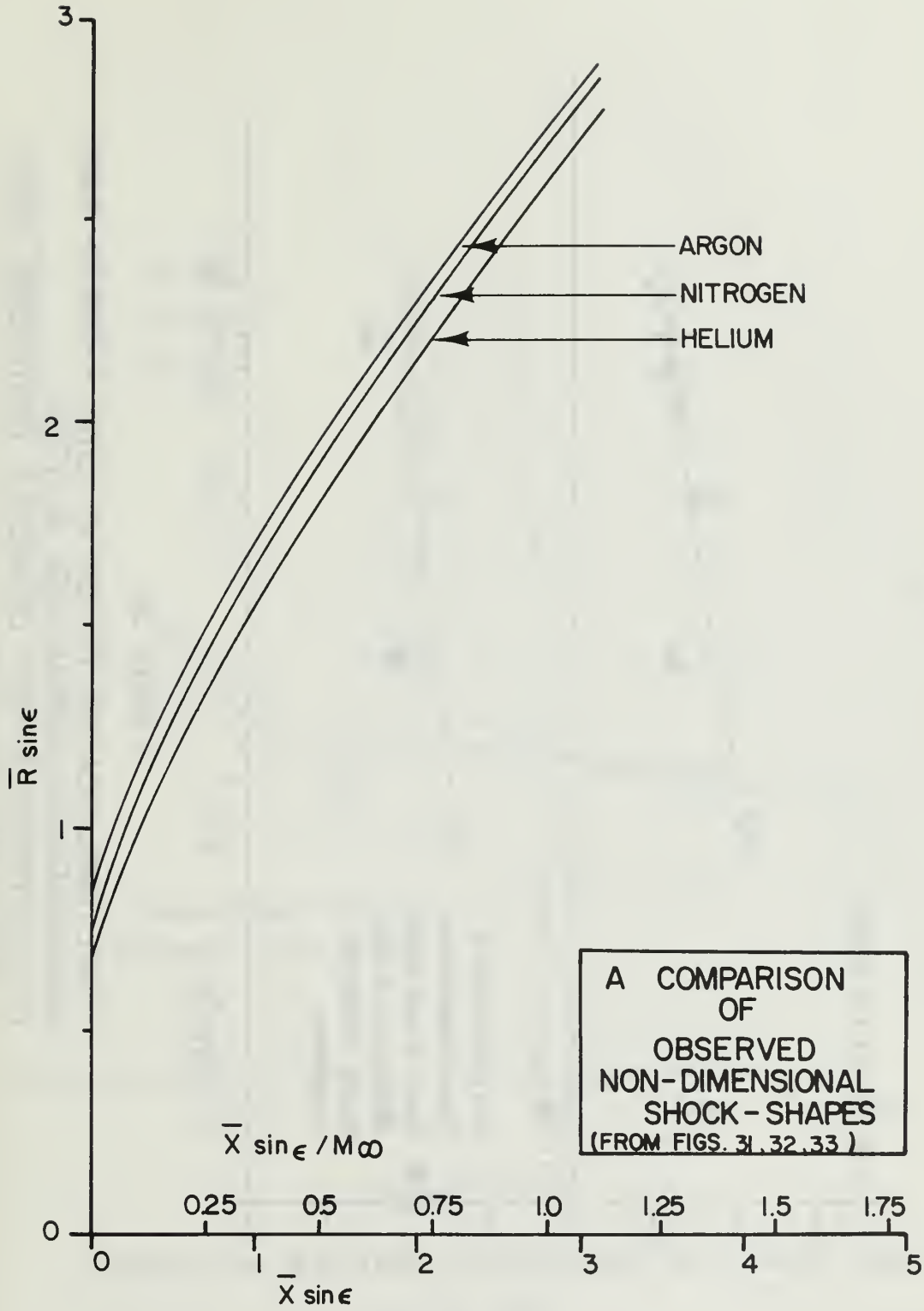
3
2
1
0
$\bar{R}\sin\epsilon$
ARGON
NITROGEN
HELIUM
A COMPARISON OF OBSERVED NON-DIMENSIONAL SHOCK-SHAPES (FROM FIGS. 31, 32, 33)
$\bar{X}\sin\epsilon / M\infty$
0.25
0.5
0.75
1.0
1.25
1.5
1.75
0
1
2
3
4
5
$\bar{X}\sin\epsilon$

FIGURE 35

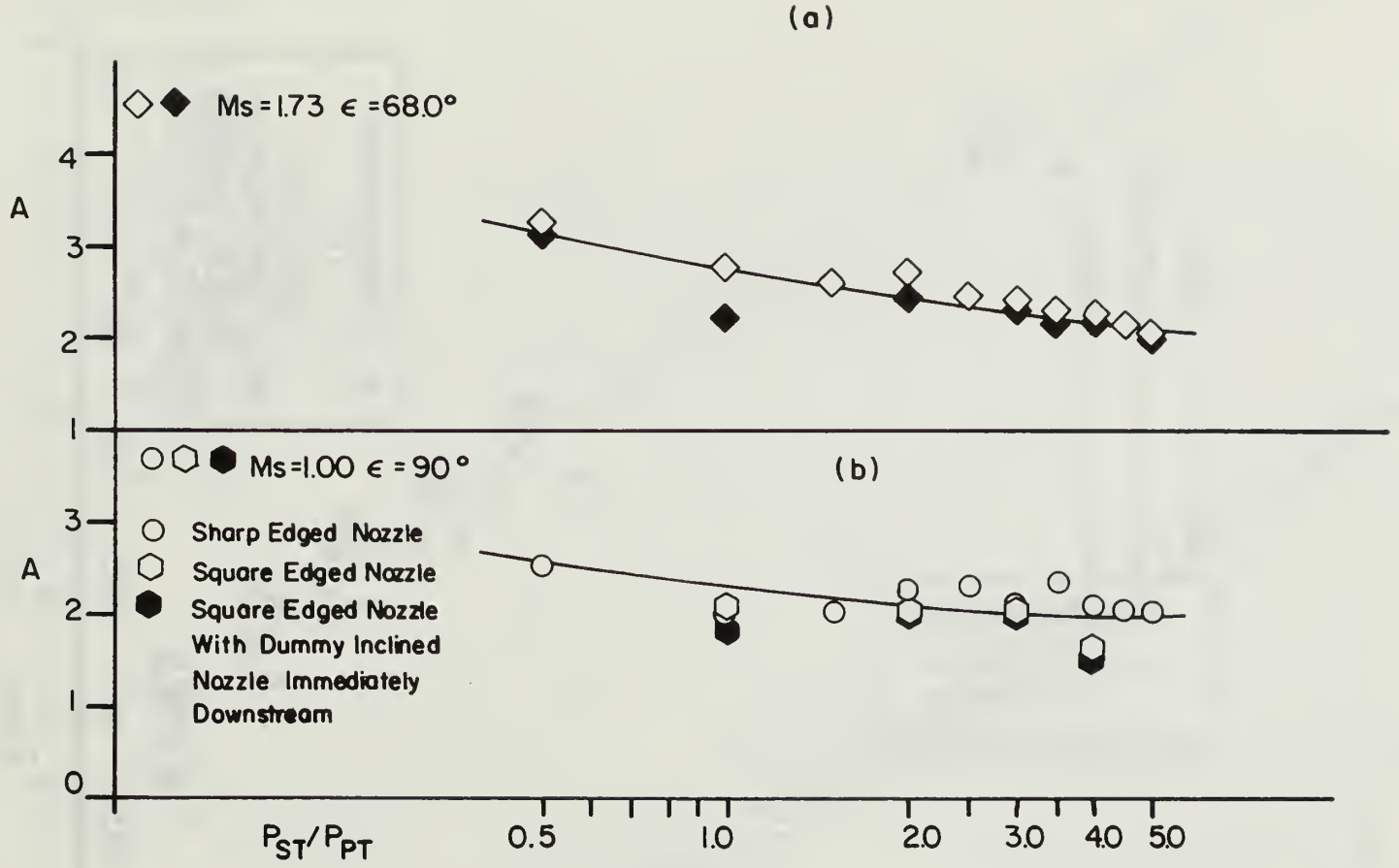

FIGURE 36

FORCE AMPLIFICATION FACTOR VS. TOTAL PRESSURE RATIO
(a) ILLUSTRATES TYPICAL DATA SCATTER
(b) ILLUSTRATES EFFECT OF NOZZLE PROTRUSION ABOVE THE PLATE AT $\epsilon < 90°$

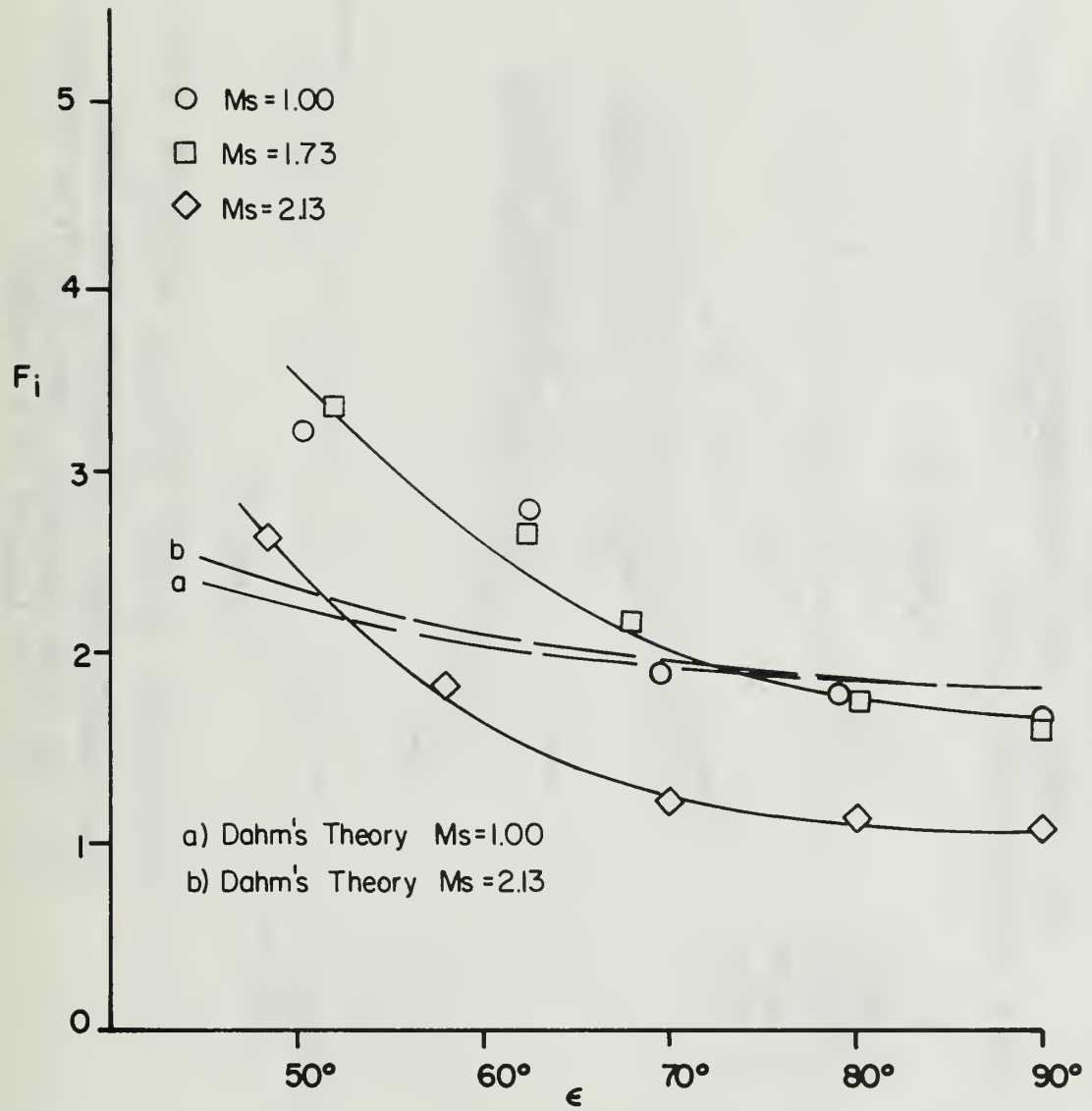

FIGURE 37

INTERACTION SIDE FORCE VS. SECONDARY INCLINATION ANGLE

(P_{ST}/P_{PT} = 3.0)

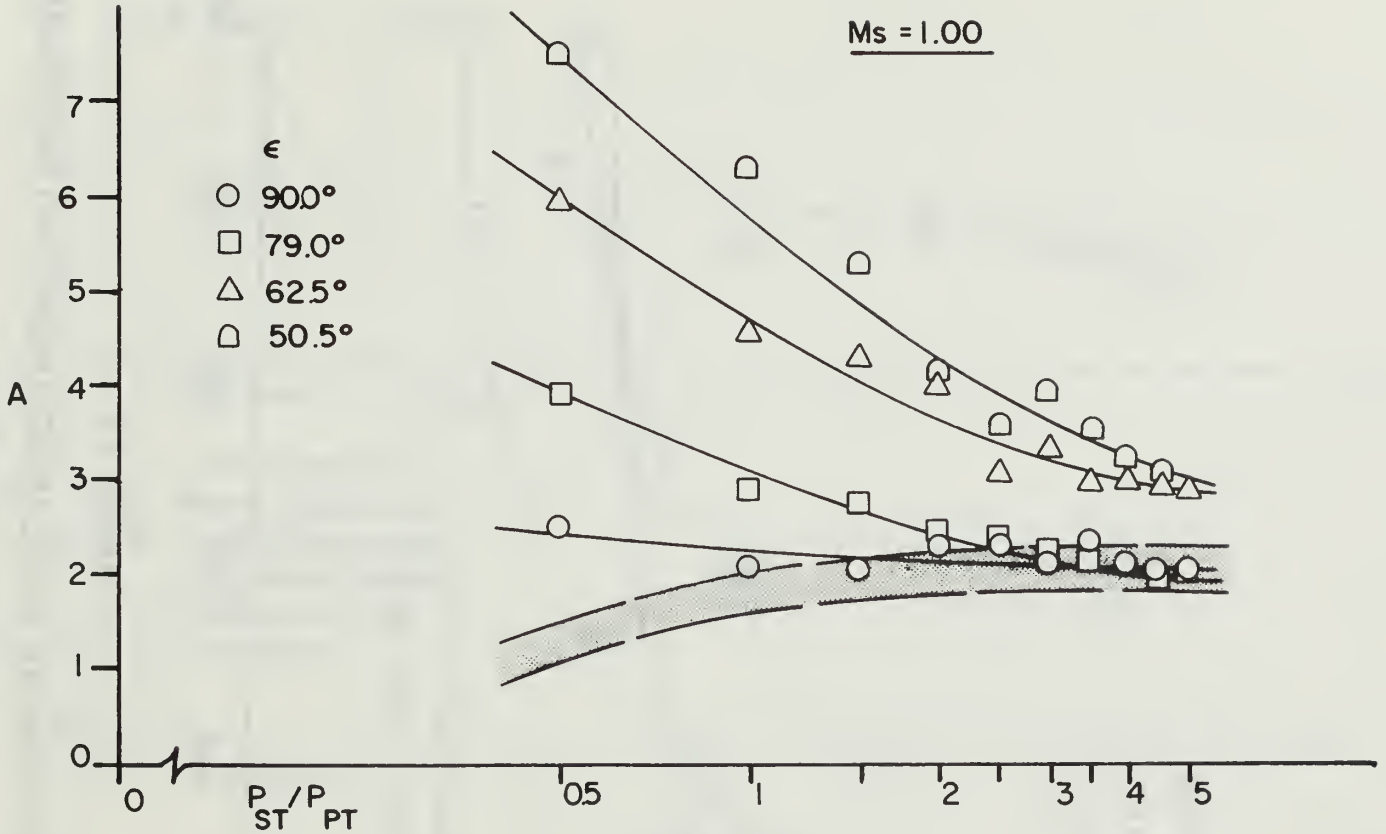

FIGURE 38

FORCE AMPLIFICATION FACTOR VS. TOTAL PRESSURE RATIO

THE SHADED AREA REPRESENTS THE RANGE OF THE SEMI-EMPIRICAL AMPLIFICATION FACTOR A' FOR THE VALUES OF ϵ SHOWN

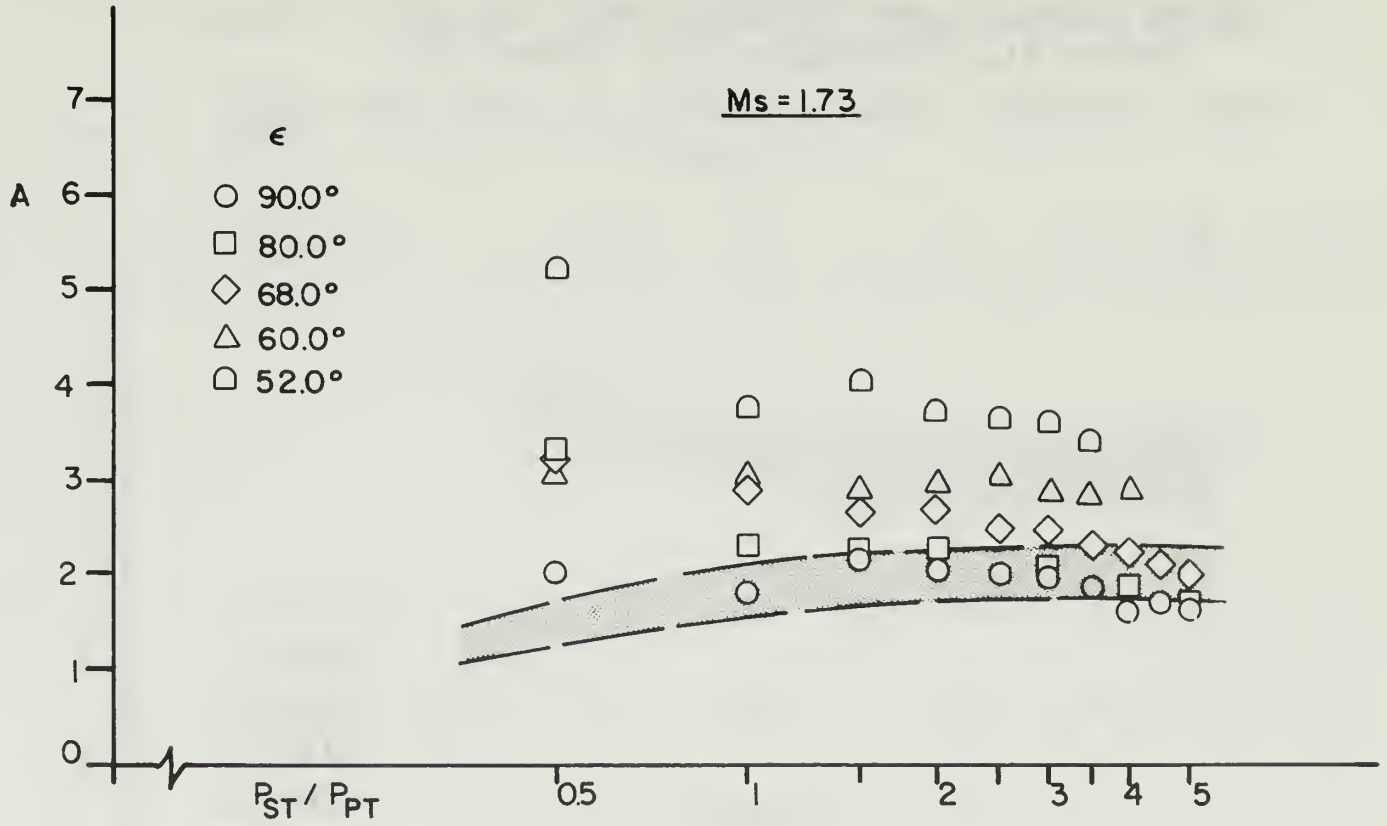

FIGURE 39

FORCE AMPLIFICATION FACTOR VS. TOTAL PRESSURE RATIO
THE SHADED AREA REPRESENTS THE RANGE
OF THE SEMI-EMPIRICAL AMPLIFICATION FACTOR
A' FOR THE VALUES OF ϵ SHOWN

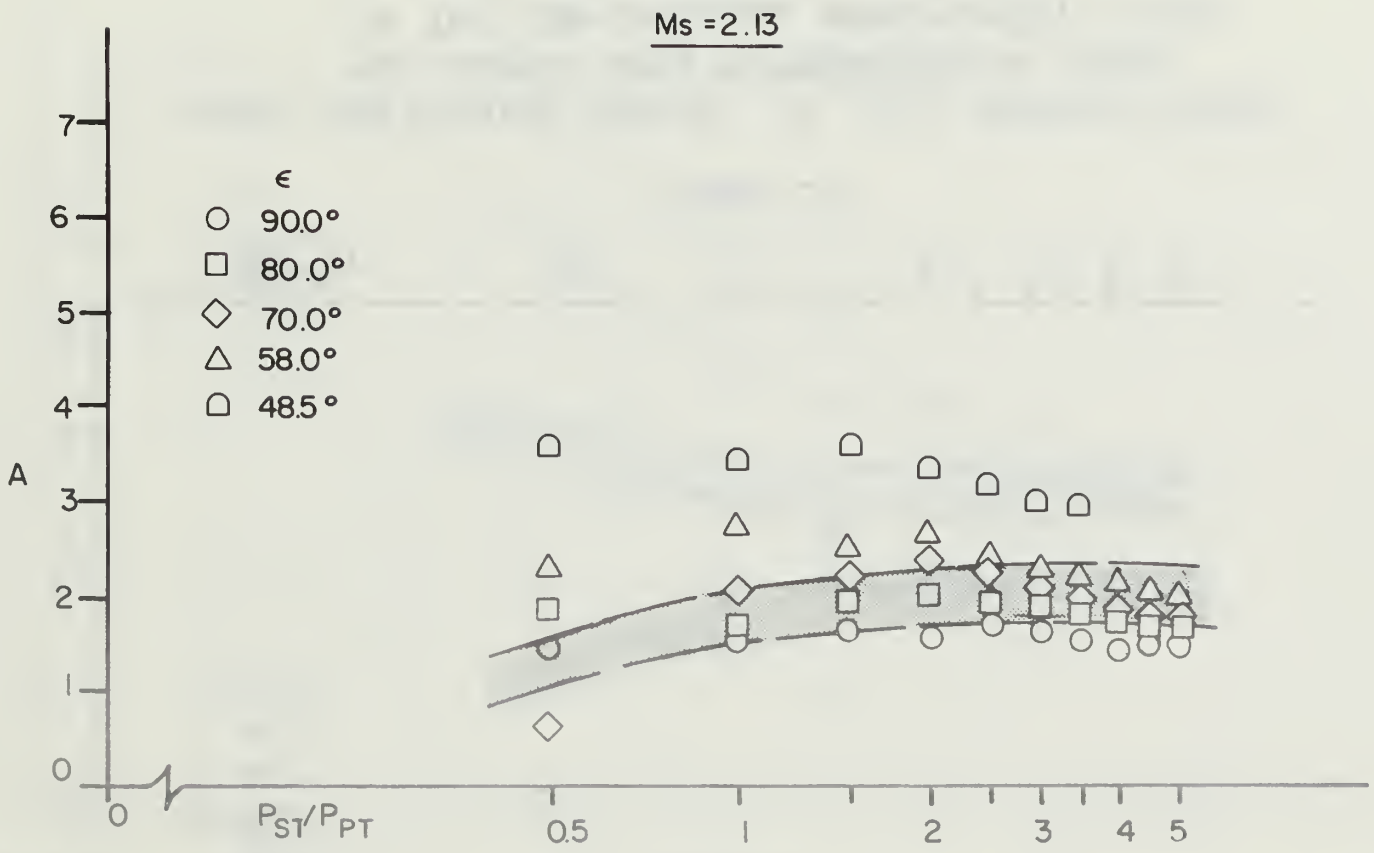

FIGURE 40

FORCE AMPLIFICATION FACTOR VS. TOTAL PRESSURE RATIO

THE SHADED AREA REPRESENTS THE RANGE OF THE SEMI-EMPIRICAL AMPLIFICATION FACTOR A' FOR THE VALUES OF ϵ SHOWN

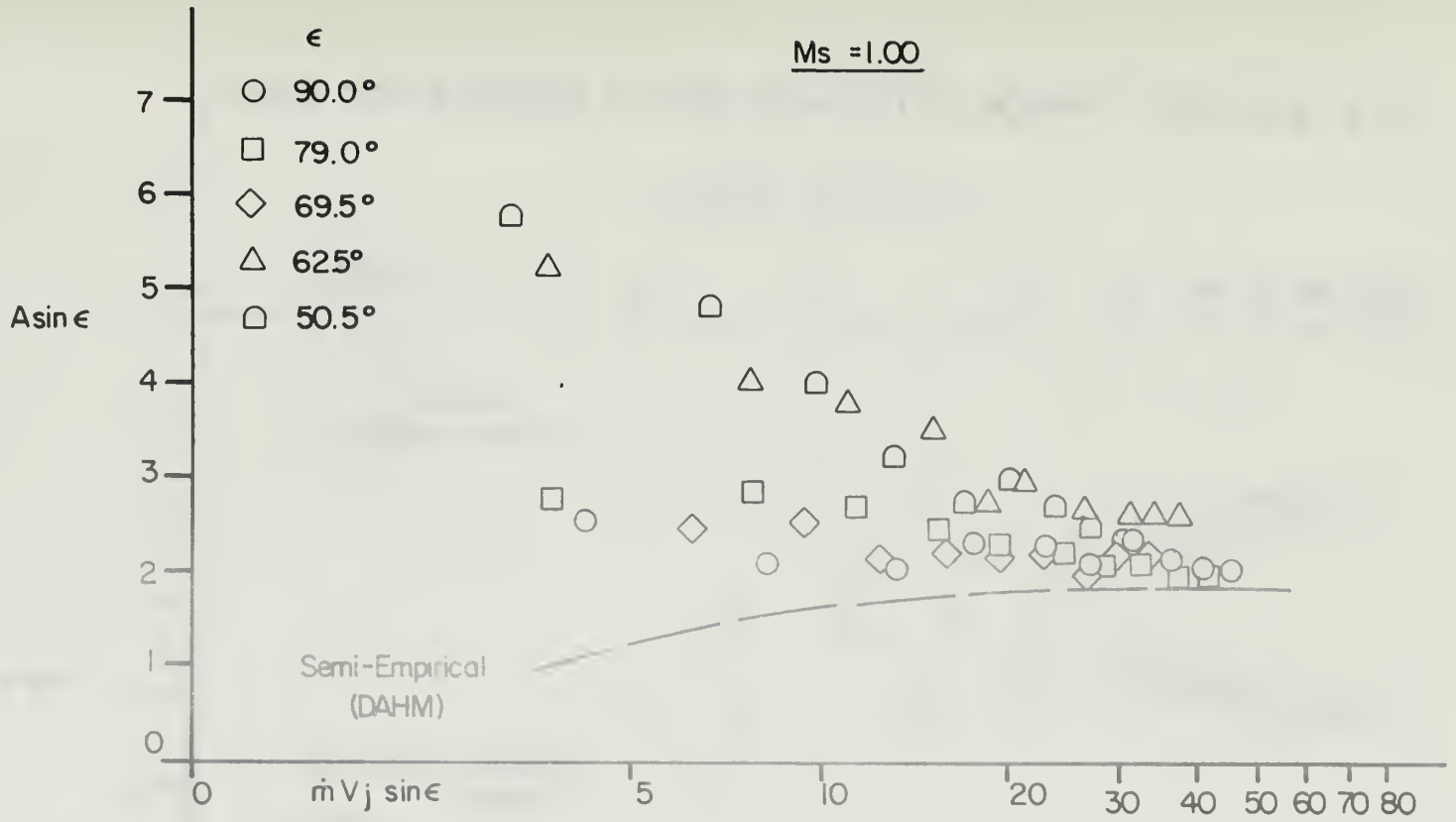

FIGURE 41

FORCE AMPLIFICATION FACTOR (Ms=1.00) VS. NORMAL MOMENTUM FLUX

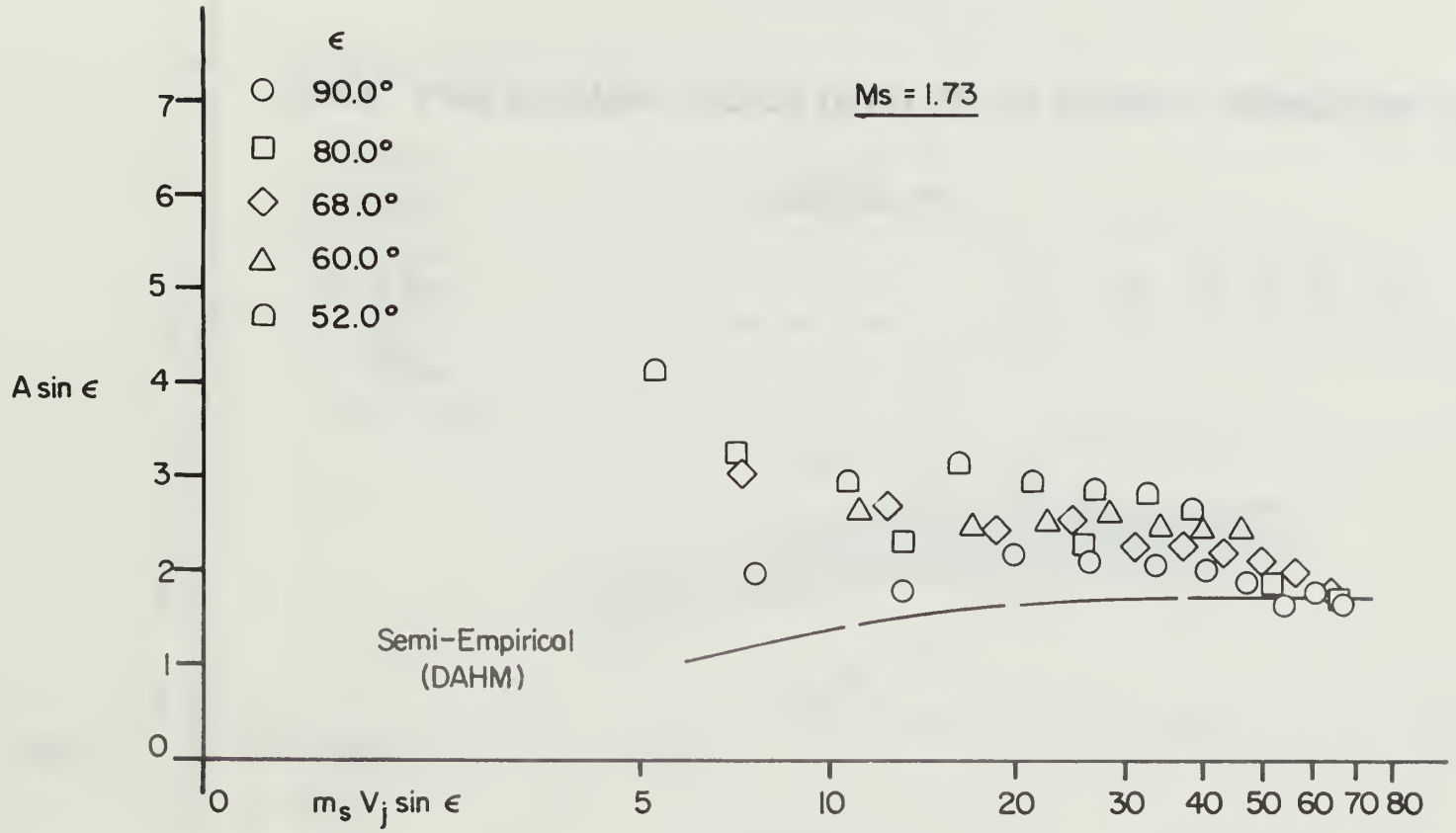

FIGURE 42

FORCE AMPLIFICATION FACTOR (Ms=1.73) VS. NORMAL MOMENTUM FLUX

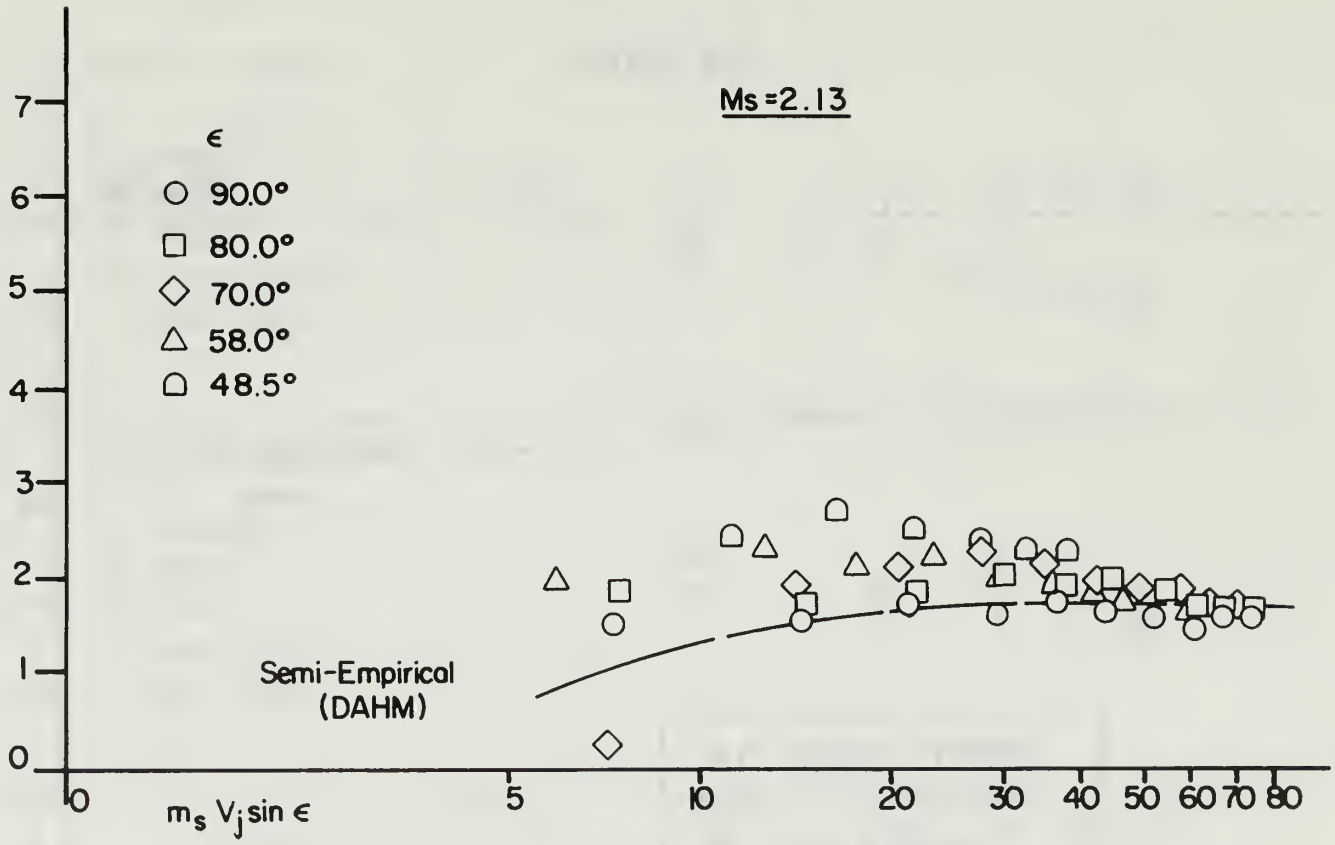

FIGURE 43

FORCE AMPLIFICATION FACTOR (Ms=2.13) VS. NORMAL MOMENTUM FLUX

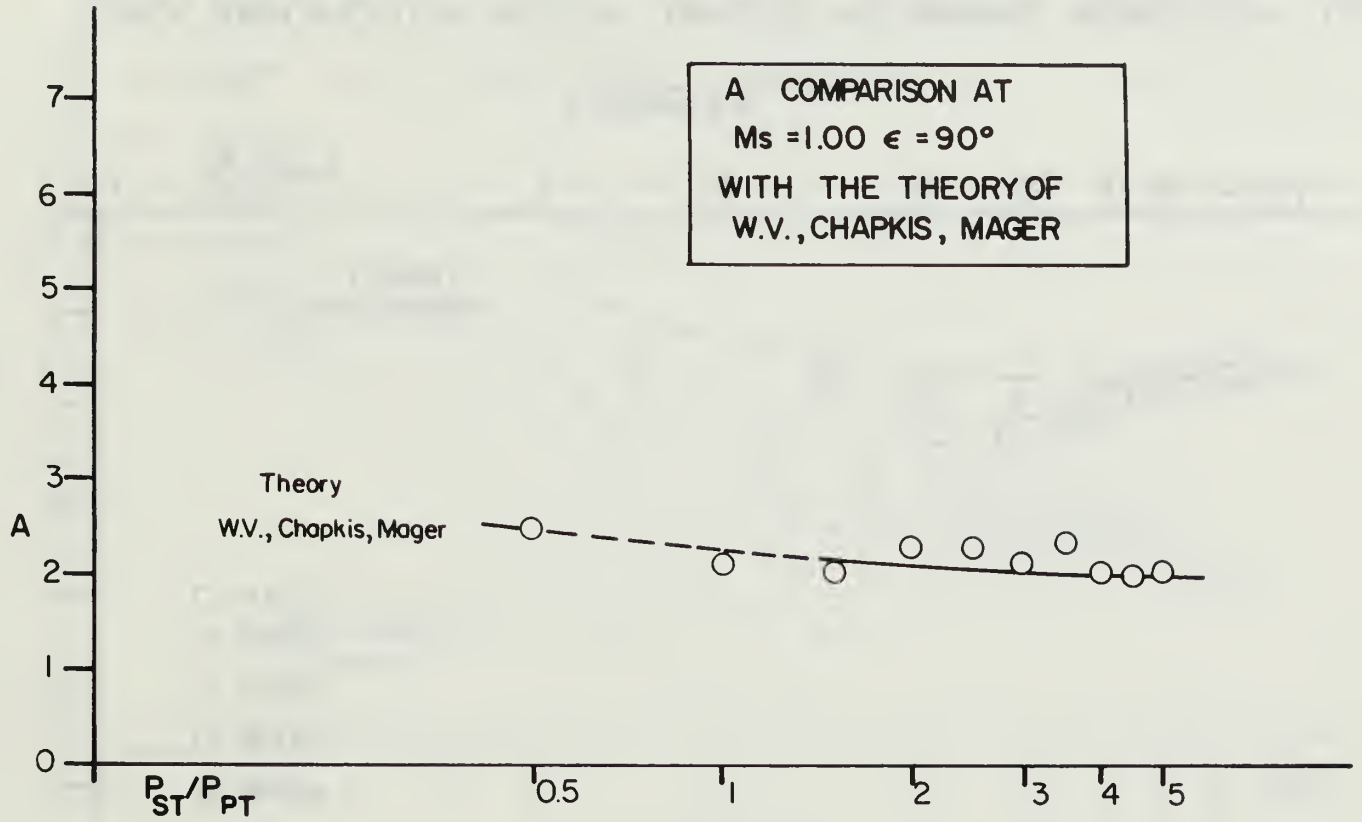
A COMPARISON AT
Ms =1.00 ϵ =90°
WITH THE THEORY OF
W.V., CHAPKIS, MAGER
Theory
W.V., Chapkis, Mager
A
0
1
2
3
4
5
6
7
P_{ST}/P_{PT}
0.5
1
2
3
4
5

FIGURE 44

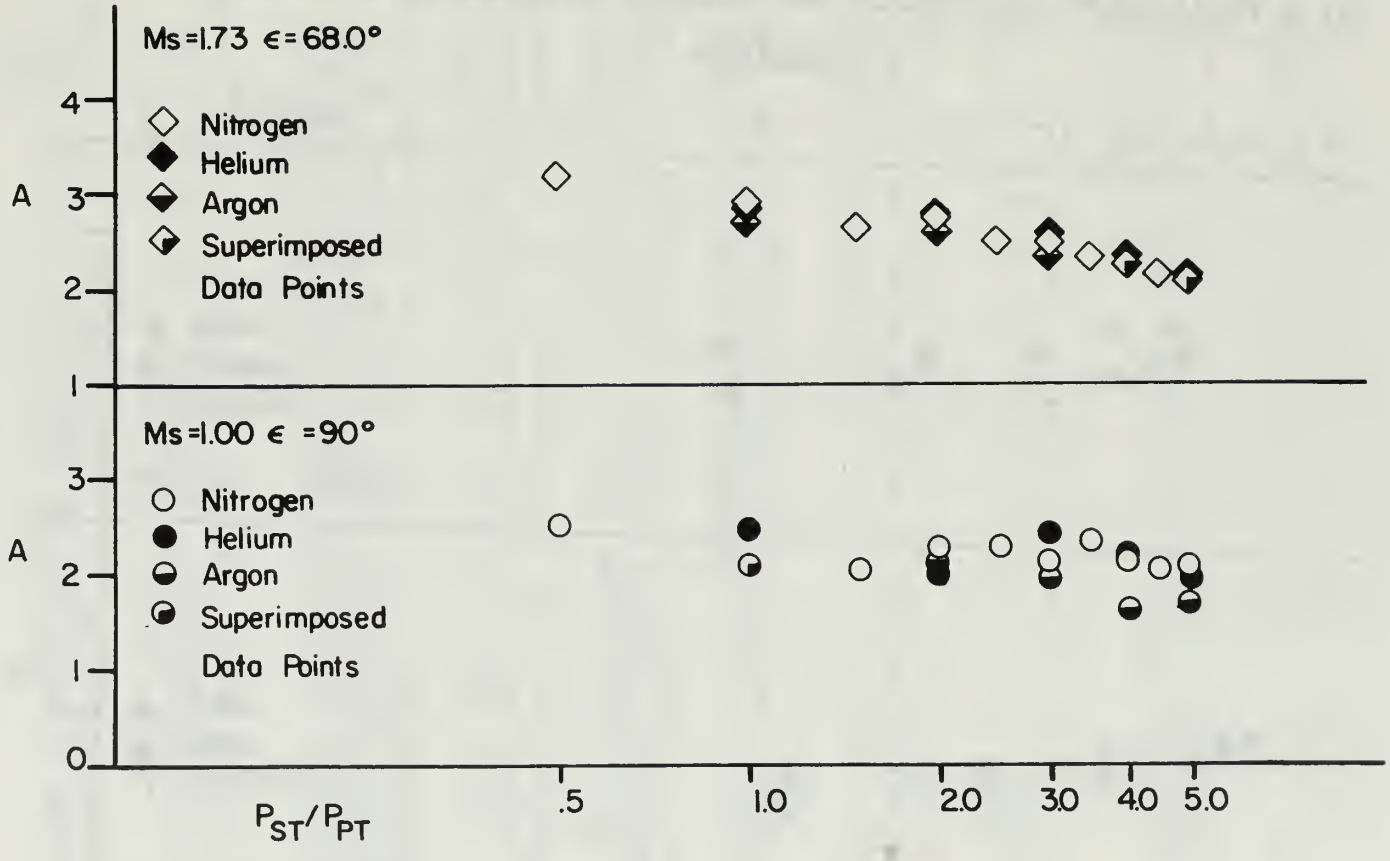

FIGURE 45

FORCE AMPLIFICATION FACTOR VS. TOTAL PRESSURE RATIO
A COMPARISON FOR GASES OF VARIOUS MOLECULAR WEIGHT

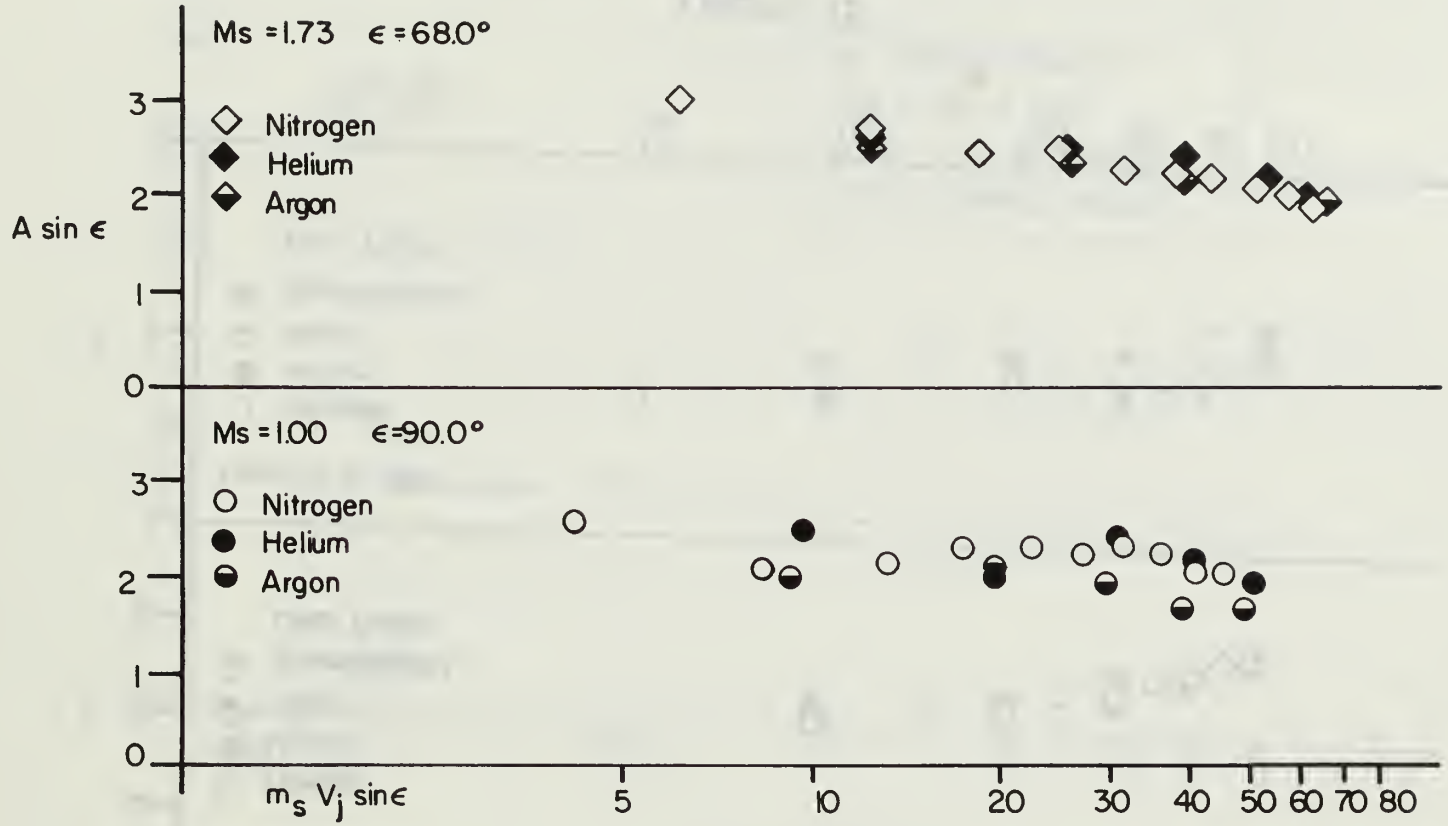

FIGURE 46

FORCE AMPLIFICATION FACTOR VS. SECONDARY MOMENTUM FLUX
A COMPARISON FOR GASES OF VARIOUS MOLECULAR WEIGHT

LIST OF REFERENCES

1. Zukoski, E. E., Spaid, F. W., "Secondary Injection of Gases into a Supersonic Flow," AIAA Journal, v.2., p. 1689-1696, October 1964.

2. U. S. Army Missile Command Report No. RD-TR-68-5, Lateral Jet Control Effectiveness Prediction for Axisymmetric Missile Configurations, by L. A. Cassel, J. G. Davis and D. P. Engh, June, 1968.

3. AFFDL-TR-67-90, Vol. I, Control Effectiveness of Transverse Jets Interacting with a High Speed Free Stream, by J. W. Barns, J. G. Davis and H. H. Tang, July 1967.

4. Crist, S., Sherman, P. M., and Glass, D. R., "Study of the Highly Underexpanded Sonic Jet," AIAA Journal, May 1967.

5. Schetz, J. A., and Billig, F. S., "Penetration of Gaseous Jets Injected into a Supersonic Stream," Journal of Spacecraft, v.3, p. 1568-1665, November 1966.

6. Hayes, W. D., "On Hypersonic Similitude," Quarterly Journal of Applied Mathematics, v.5, p. 107, 1947.

7. Lees, L., Kubota, T., "Inviscid Hypersonic Flow over Blunt Nosed Slender Bodies," Journal of Aerospace Science, v. 24, p. 195-202, March 1957.

8. Broadwell, J. E., "Analysis of the Fluid Mechanics of Secondary Injection for Thrust Vector Control," AIAA Journal, v. 1, p. 1067-1075, May 1963.

9. Vidya Technical Note No. 9166-TN-3, The Development of an Analogy to Blast Wave Theory for the Prediction of Interaction Forces Associated with Gaseous Secondary Injection into a Supersonic Stream, by T. J. Dahm, May 1964.

10. Sakuri, A., "On the Propagation and Structure of a Blast Wave, I," Journal of the Physical Society of Japan, v. 8, p. 662-669, October 1953.

11. Sakuri, A., "On the Propagation and Structure of a Blast Wave, II," Journal of the Physical Society of Japan, v. 9, p. 256-266, April 1954.

12. NASA Memorandum 12-5-58W, Interaction Effects Produced by a Jet Exhausting Laterally near the Base of an Ogive Cylinder, by P. W. Vinson, J. L. Amick and Liepman, 1959.

13. Wu, J. M., Chapkis, R. L. Mager, A., "Approximate Analysis of Thrust Vector Control by Fluid Injection," American Rocket Society Journal, p. 1677-1685, December 1961.

14. John Hopkins University / APL CM 1010, Secondary Gas Injection in a Conical Nozzle, by R. E. Walker, A. R. Stone and M. Shander, February 1962.

15. AIAA Paper No. 69-1, The Effect of Stagnation Temperature and Molecular Weight Variation of Gaseous Injection into a Supersonic Stream, by L. J. Chrans and D. J. Collins, January 1969.

16. WADD Technical Report 60-329, Interaction Effects of Side Jets Issuing from Flat Plates and Cylinders Alined with a Supersonic Stream, by J. L. Amick and P. B. Hays, June 1960.

17. Power Test Codes Supplement, Chapter 4, "Flow Measurement - Instruments and Apparatus," PTC 19.5, v. 4, part 5, American Society of Mechanical Engineers, 1959.

18. Adamson, T. C., and Nichols, J. A., "On the Structure of Jets from Highly Underexpanded Nozzles into Still Air," Journal of the Aero/Space Sciences, v. 26, p. p. 16-24, January 1959.

19. R. P. E. Technical Report #67/7, Thrust Vector Control of Rocket Engines by Gaseous Injection (A Critical Appraisal of Theoretical Models), by T. R. Horton and A. J. Meade, July 1967.

20. NACA Report 1135, Equations, Tables and Charts for Compressible Flow, by Ames Research Staff, 1953.

INITIAL DISTRIBUTION LIST

		No. Copies
1.	Defense Documentation Center Cameron Station Alexandria, Virginia 22314	20
2.	Library Naval Postgraduate School Monterey, California 93940	2
3.	Commander, Naval Air Systems Command Navy Department Washington, D. C. 20360 Attn: Dr. E. S. Lamar (Code 03C) (1) Attn: Dr. R. S. Burington (1)	2
4.	Professor D. J. Collins Department of Aeronautics Naval Postgraduate School Monterey, California 93940	4
5.	Chairman, Department of Aeronautics Naval Postgraduate School Monterey, California 93940	1
6.	Commander Naval Ordnance Systems Command Navy Department Washington, D. C. 20360	1
7.	Office Of Naval Research Navy Department Washington, D. C. 20360	1
8.	Naval Air Systems Command Research and Technology Washington, D. C. 20390 Attn: Warfare Branch (Code 3031)	1
9.	Mr. G. L. Desmond (Code 320) Aerodynamics and Structures Administration Research and Technology, Naval Air Systems Command Washington, D. C. 20390	1
10.	Dr. F. I. Tanczos Technical Director, Research and Technology Naval Air Systems Command Washington, D. C. 20390	1

11. Head, Department of Engineering — 1
U. S. Naval Academy
Annapolis, Maryland

12. Mr. I. Silver (Code 330) — 1
Propulsion Administrator
Research and Technology
Naval Air Systems Command
Washington, D. C. 20390

13. Office of Naval Research (Code 420) — 1
Physical Sciences Division
Navy Department
Washington, D. C. 20360

14. Office of Naval Research — 1
Material Science Division
Navy Department
Washington, D. C. 20360

Attn: R. D. Cooper (Code 438)

15. Office of Naval Research (Code 430) — 1
Mathematical Sciences Division
Navy Department
Washington, D. C. 20360

16. Office of Naval Research
Air Programs Office
Navy Department
Washington, D. C. 20360

17. Naval Air Systems Command — 1
Navy Department
Washington, D. C. 20390

Attn: J. W. Malloy, Weapons Branch (Code 3033)

18. Commander — 8
Naval Air Systems Command
Headquarters
Washington, D. C. 20360

AIR-03C (1)
AIR-310 (1)
AIR-320 (1)
AIR-330B (1)
AIR-536 (1)
AIR-5366 (1)
AIR-5367 (1)
AIR-538 (1)

19. Commander 2
Naval Ordnance Systems Command
Headquarters
Washington, D. C. 20360

ORD-03B (1)
ORD-033 (1)

20. Chief of Naval Research 1
Dr. Ralph Roberts (Code 429)
Navy Department
Washington, D. C. 20360

21. Naval Ordnance Station 1
Dr. G. Testi (Code RR)
Indian Head, Maryland 20640

22. Army Missile Command 2
Research and Development Directorate
Redstone Arsenal
Huntsville, Alabama 35809

Propulsion Laboratory, F. James (1)
Library (1)

23. Commander 4
Naval Weapons Center
China Lake, California 93555

Code 608 (1)
Code 451 (1)
Code 458 (1)
Library (1)

24. Commander 2
Naval Ordnance Laboratory
White Oak
Silver Spring, Maryland 20910

Code 310 (1)
Library (1)

25. Commanding Officer and Director 2
Naval Ships Research and Development Center
Washington, D. C. 20007

Code 600 (1)
Library (1)

26. Applied Physics Laboratory 1
8621 Georgeia Avenue
Silver Springs, Maryland 20910

27. Air Force Aero-Propulsion Laboratory 2
Wright-Patterson Air Force Base, Ohio 45433

APG (1)
APX (1)

28. Air Force Armament Laboratory 2
Eglin Air Force Base, Florida 32544
ATW (1)
ATZ (1)

29. Air Force Rocket Propulsion Laboratory 7
Edwards Air Force Base, California 93523

RPM (1)
RPMC (1)
RPPP (1)
RPR (1)
RPRE (1)
RPRP (1)
RPX (1)

30. Air Force Flight Dynamics Laboratory 1
Wright-Patterson Air Force Base, Ohio 45433

31. CO, Navy Space Systems Activity 1
Hq. Air Force Space Systems Division
Air Force Unit Post Office
Los Angeles, California 90045

32. LT. Larry N. Koch 1
USS HORNET (CVS 12)
Fleet Post Office
San Francisco, California 96601

UNCLASSIFIED
Security Classification

DOCUMENT CONTROL DATA - R & D

(Security classification of title, body of abstract and indexing annotation must be entered when the overall report is classified)

1. ORIGINATING ACTIVITY *(Corporate author)*

Naval Postgraduate School
Monterey, California 93940

2a. REPORT SECURITY CLASSIFICATION

Unclassified

2b. GROUP

3 REPORT TITLE

THE EFFECT OF VARYING SECONDARY MACH NUMBER AND INJECTION ANGLE ON SECONDARY GASEOUS INJECTION INTO A SUPERSONIC FLOW

4. DESCRIPTIVE NOTES *(Type of report and inclusive dates)*

Engineer's Thesis; June 1969

5. AUTHOR(S) *(First name, middle initial, last name)*

Larry Neil Koch, Lieutenant, United States Navy

6. REPORT DATE	7a. TOTAL NO. OF PAGES	7b. NO. OF REFS
June 1969	103	20

8a. CONTRACT OR GRANT NO.	9a. ORIGINATOR'S REPORT NUMBER(S)
b. PROJECT NO.	
c.	9b. OTHER REPORT NO(S) *(Any other numbers that may be assigned this report)*
d.	

10. DISTRIBUTION STATEMENT

Distribution of this document is unlimited.

11. SUPPLEMENTARY NOTES	12. SPONSORING MILITARY ACTIVITY
	Naval Postgraduate School Monterey, California 93940

13. ABSTRACT

This study was undertaken to investigate the effects of varying both the secondary Mach number and angle of inclination relative to the primary stream on the flow field generated by the interaction of a secondary jet with a supersonic mainstream. The experimental portions of this investigation were conducted at a primary Mach number of 2.80 in the Naval Postgraduate School Supersonic Wind Tunnel. Data are presented and compared with various theories. This presentation includes correlation of the penetration height of the secondary flow, bow-shock shape by non-dimensionalization with respect to various parameters and correlation of interaction side force amplification factor.

14 KEY WORDS	LINK A		LINK B		LINK C	
	ROLE	WT	ROLE	WT	ROLE	WT
SECONDARY GASEOUS INJECTION						